7

Stabilization Techniques and Silicon-Germanium Saturable Absorbers for High Repetition Rate Mode-Locked Lasers

by

Felix Jan Grawert

M.S., Electrical Engineering,
Georgia Institute of Technology, 2000

Dipl.-Ing., Electrical Engineering,
University of Karlsruhe, Germany, 2001

Submitted to the Department of Electrical Engineering and Computer Science
in partial fulfillment of the requirements for the degree of

Doctor of Philosophy in Electrical Engineering and Computer Science

at the

MASSACHUSETTS INSTITUTE OF TECHNOLOGY

September 2005

Author .....
Department of Electrical Engineering and Computer Science
August 5, 2005

Certified by .....
Franz X. Kärtner
Professor of Electrical Engineering and Computer Science
Thesis Supervisor

Accepted by .....
Arthur C. Smith
Chairman, Department Committee on Graduate Students

This thesis is dedicated to my mother Hilleken.
Thank you for supporting me, believing in me and encouraging me to pursue my dreams over all the many years.

Stabilization Techniques and Silicon-Germanium Saturable Absorbers for High Repetition Rate Mode-Locked Lasers

by

Felix Jan Grawert

Submitted to the Department of Electrical Engineering and Computer Science
on August 5, 2005, in partial fulfillment of the
requirements for the degree of
Doctor of Philosophy in Electrical Engineering and Computer Science

Abstract

The monolithic integration of passively mode-locked solid-state lasers at highest repetition rates has been prevented by Q-switching instabilities and the lack of integrable saturable absorbers to date. In this thesis we demonstrate in theory and experiment that active feedback electronics controlling the intracavity loss of the laser is capable of suppressing the Q-switching instability. We introduce a control system's perspective to the stability of saturable absorber mode-locked lasers. This approach unifies the existing methods of laser stabilization and identifies feedback control with an intracavity loss modulator as a universal stabilization scheme, applicable without restrictions to lasers at the highest repetition rates. This finding is validated in laboratory experiments by showing that a laser which is unstable without feedback control can reach a noise performance equivalent to that of a passively stabilized laser, once the feedback controller is engaged. The addition of feedback stabilization does not negatively affect the pulse shaping dynamics, since controller and mode-locking dynamics occur on vastly different timescales. Furthermore, we address the materials challenge of manufacturing a CMOS-compatible saturable Bragg reflector in the Si-SiO_2-Ge materials system, enabling the monolithic integration of the absorber with the laser gain medium of future compact mode-locked lasers. A wafer-scale Si-SiO_2 high reflector with 99.8% peak reflectance and an unprecedented bandwidth of 700 nm in the near-infrared serves as the substrate of a saturable Bragg reflector, while a germanium layer grown on top provides saturable loss. Ultrafast recovery of the saturation is observed in pump-probe measurements, indicating the operation of the saturable Bragg reflector as a fast semiconductor saturable absorber in the laser. In contrast, strong inverse saturable loss occurs in the regime of high fluence, contributing to stabilization against Q-switching instabilities. An erbium-ytterbium:glass laser mode-locked with the silicon-germanium saturable Bragg reflector generates the shortest pulse and broadest optical spectrum obtained from a bulk Er-Yb:glass laser to date. Spanning the C-band of optical communications on a ± 10 dB level, it demonstrates that mode-locked Er-Yb:glass lasers can serve as multi-wavelength laser sources in next-generation optical communications

systems, providing all channels across the communications spectrum with a stable train of pulses.

Thesis Supervisor: Franz X. Kärtner
Title: Professor of Electrical Engineering and Computer Science

Acknowledgments

First and foremost I would like to thank my advisor Professor Franz X. Kärtner for his inspiring support, patient mentorship and seemingly endless energy in pursuing new concepts. In every respect of our work his creativity proved to be a sheer infinite source of ideas and his optimism paired with the willingness to take risks taught me to think free of constraints. Not only did I have the freedom to pursue my own research agenda, but his deep trust in my abilities left me with an incredible amount of responsibility, giving me the room for growth I desired. I am very thankful for the opportunity to work with him over the last four years. I also would like to thank is wife Petra for the many invitations to their home and her patience when I was keeping her husband busy with research.

I would like to express deep thanks to Professor Erich P. Ippen and Professor Rajeev J. Ram for numerous scientific discussions, research ideas and for serving on my thesis committee. Professor Terry P. Orlando was my academic advisor in the last four years and his advice and support with respect to all facets of academic life were invaluable.

My research couldn't have happened outside of the creative and supportive atmosphere of M.I.T. and without numerous friends and colleagues on and off the campus. First, I would like to thank the members of my research group for numerous discussions, suggestions and equipment loans. F. Ömer Ilday, friend and mentor, taught me more than can be expressed in words, David "buddy" Kielpinski helped me out and challenged me whenever he could, Axel Winter built up my knowledge of RF electronics and Oliver Mückes brilliant questions and intuition always pointed me to the most relevant aspects of a concept. My officemates Richard Ell, Lingze Duan, Onur Kuzucu and Christian Koos always had an open ear for everything from science to world politics. Fuwan Gan, Jan-Malte Fischer, Milos Popovic and Mike Watts invited me to an excursion into integrated optics and high speed optical modulators, while it was a pleasure to share the burden of late nights in lab and office with Jungwon Kim, Jonathan Birge, Blaise Gassend, Jonathan Birge, Ariel Gordon, Lia Matos, Jeff Chen, Hyunil Byun, Jonathan Cox, Stefan Rausch and Alex Killi. Christian Jirauschek gave me invaluable advice and guidance throughout our overlapping time, and it is great to see him again in Germany soon. With Philipp

Wagenblast and Aleem Siddiqui I explored the art of single-frequency lasers, as opposed to the mode-locked work I spent most of my time on. Thomas Schibli got me started in the lab and laid the foundation of my electronics knowledge. In numerous projects I could rely on the superb knowledge and equipment of the greater optics group, whose members would always be willing to leave their work, give advice or even look after a setup being stuck. My particular thanks goes to Juliet Gopinath who helped me not only with numerous pump probe measurements, an introduction to saturable absorbers, advice on post-processing of semiconductor samples and an endless number of equipment loans out of the Ippen lab, especially in the first year, during the buildup phase of our own laboratory. Ali Motamedi, kept the support going and allowed me to get my own hands-on pump probe experience in the VCSEL and silicon-germanium project, so did Hanfei Shen. Jason Sickler introduced my to fiber splicing, Dan Ripin to Cr^{4+}:YAG lasers and Peter Rakich, Matthew Grein, Marcus Dahlem and Hideyuki Sotobayashi would always be willing to help with ideas and equipment. The same holds for Professor Fujimoto and his research group, where Aaron Aguirre, Robert Huber, Andrew Kowalevicz, Aurea Tucay Zare, Maciej Wojtkowski, Vikas Sharma, Pei-Lin Hsiung and Tony Ko would always be up for a chat or a research discussion.

My projects included a large number of collaborations across campus and around the world, and I owe special thanks to all those who supported me with concepts and components. My particular thanks with regard to the silicon-germanium project goes to my friend Shoji Akiyama, who was the ideal research partner over the two years of our project. Endless hours in the lab converted our dreams to reality and none of my ideas was too wild to be rejected without sincere thought. Thank you, Shoji! Of course, the project would have never succeeded without the support of Jifeng Liu, Professor Kazumi Wada and Professor Lionel C. Kimerling. With our initial results it is now in the best hands of Muyiwa Olubuyide, Professor Judy Hoyt, Jung Yoon at Lincoln Lab as well as Yasha Yi and Ching-yin Hong in the Kimerling group. Special thanks also go to Dr. George Celler and Dr. Takeshi Akatsu of Soitec Inc. for providing silicon-on-insulator and germanium-on-insulator wafers for our work. With respect to sample analysis we are grateful for the support of Libby Shaw and Tim McClure in the CMSE analysis lab.

The other major collaboration, extending over my entire stay at MIT was centered on group III-V semiconductor saturable absorbers and optical modulators. Professor Leslie Kolodziejski and Gale Petrich have grown a plethora of structures for us with work still in progress. Several aspects of this project would have been impossible without the dielectric-metallic coatings deposited by Peter O'Brien at Lincoln Lab, who also fabricated all the custom optics for the erbium-ytterbium:glass laser and all resonant coatings for our saturable absorbers. An intense collaboration with Markus Maute of Professor M.-C. Amann's research group in Munich, Germany lead to several optical modulator devices. He also provided us with the VCSELs that we employed as optical modulators, while Ben Williams of Professor Quing Hu's group provided the knowledge that allowed successful mounting of these devices. An Erbium-doped waveguide amplifier borrowed from Professor Frank Wise at Cornell University was the basis for most of our work on active laser stabilization, many thanks for the long-term loan!

None of my work would have been so efficient without the support infrastructure of the Research Lab of Electronics and M.I.T. in general. Al McGurl and Bill Gibbs would fix any conceivable problem around the lab infrastructure and help out even with the acquisition of temporary lab space. Dave Foss computer skills kept my laptop running for four years without major problems and Maxine Samuels managed to get every urgent order shipped overnight regardless how late I brought it in. Thank you all so much for the great help and real effort ! Our administrative assistants Dorothy Fleischer and Donna Gale kept the everyday operations smooth and running while none of the machining needs I had was too challenging for Fred Cote of the Edgerton student machine shop.

Finally, I would like to thank my girlfriend Andria M. Gong for her loving support and understanding for the many nights and weekends spent in the lab.

Contents

List of Figures

List of Tables

Chapter 1

Motivation

The development of mode-locked lasers at high repetition rates paired with the emergence of photonic integrated circuits (PICs) paves the way to commercial high-volume applications of ultrafast laser technology. In this thesis we provide the essential components for enabling the construction of bulk mode-locked lasers at highest repetition rates: We demonstrate that active laser stabilization with an intracavity loss modulator is a universal approach for suppression of Q-switching instabilities, we present a silicon-germanium saturable Bragg reflector that allows for monolithic integration of saturable absorber and gain medium in the silicon materials platform, and we report the first C-band spanning mode-locked bulk Erbium-Ytterbium:glass laser to date. These results allow one to extend the advantages of bulk mode-locked solid-state lasers to future fundamentally mode-locked, high repetition rate laser systems: The broad optical spectra, the highly stable and almost jitter-free pulse trains as well as the chirp-free, Fourier-limited pulses that can be generated in these lasers are highly attractive for a number of applications.

Our research was motivated by the vision of a platform combining monolithic integrated mode-locked lasers with PICs comprising active and passive optical components as well as electronic control circuitry. The mode-locked laser produces an optical pulse train at GHz-repetition rate while the PIC allows for high-speed optical processing of the generated pulse train. This integrated platform both gives access to the unique temporal and spectral qualities of mode-locked lasers and leverages the high integration density of photonic integrated circuits, allowing for cost-effective unification of a multitude of optical

functions within a single semiconductor chip.

In the following sections we outline three major applications of compact optical systems composed of an integrated mode-locked laser and a PIC (sections 1.1-1.3). We discuss the unique performance offered by these systems, their requirements on the mode-locked laser source and possible system architectures. We then present the setup and the characteristics of the integrated mode-locked lasers anticipated for future applications and the challenges inherent in their construction that have been addressed in this thesis (section 1.4). We conclude this introduction with an outline of the topics covered in this thesis.

1.1 Application of high repetition rate mode-locked lasers in WDM networks

1.1.1 Flexible and cost-effective optical networks

Carriers in the optical communications marketplace are currently exposed to two major forces that lead to a fundamental re-evaluation of optical networking technology: The market requests order-of-magnitude reductions in component cost and operating expenses while simultaneously asking for more flexible, highly reconfigurable networks that can accommodate the imminent convergence of voice and data traffic. The pressure on prices is dictated by an erosion of margins experienced by network operators. The overall traffic in the optical network steadily increases by 80% per annum, causing a need for parallel investments in network infrastructure, and thus a parallel increase in cost [4, 5]. In contrast, revenue growth is limited to 4% per annum [4], since the carriers have been unable to capture a larger share of consumers expenses. Consequently, the rapidly growing costs at almost constant revenue lead to a steep decline in profit margin triggering the carriers to fully exploit the potential of cost reductions. It is estimated [4, 5, 6, 7] that current optical networking technology will be unable to meet the target of 40% annual cost reduction for newly deployed components as well as the need for a highly automated network that reduces the operating and maintenance expenses, which now constitute

up to 50% of transport cost, by an order of magnitude. Conventional optical networks are made of hundreds of discrete components, each in an individual package, as shown in Fig. 1-1 for a long-haul wavelength division multiplexing (WDM) system employing return-to-zero (RZ) modulation. Light for each channel of the system is generated in a continuous-wave (cw) distributed feedback (DFB) laser, then chopped into pulses by a pulse carver consisting of a fast modulator and subsequently modulated with the data to be transmitted in a second modulator. Finally, the individual channels are combined in a multiplexer, *e.g.* based on arrayed-waveguide gratings (AWGs) or on micro-ring resonator filters, and transmitted to their destination. In this system, entirely composed of discrete components, mere packaging accounts for up to 80% of total cost. Hybrid or monolithic integration of system components promises reductions in cost, physical size, power consumption and fiber routing [8].

Besides the targeted reduction of component count, optical systems integration is driven by the need for an increase in network functionality, arising from a fundamental change in the data transmitted over the network. Initially, traffic consisted almost

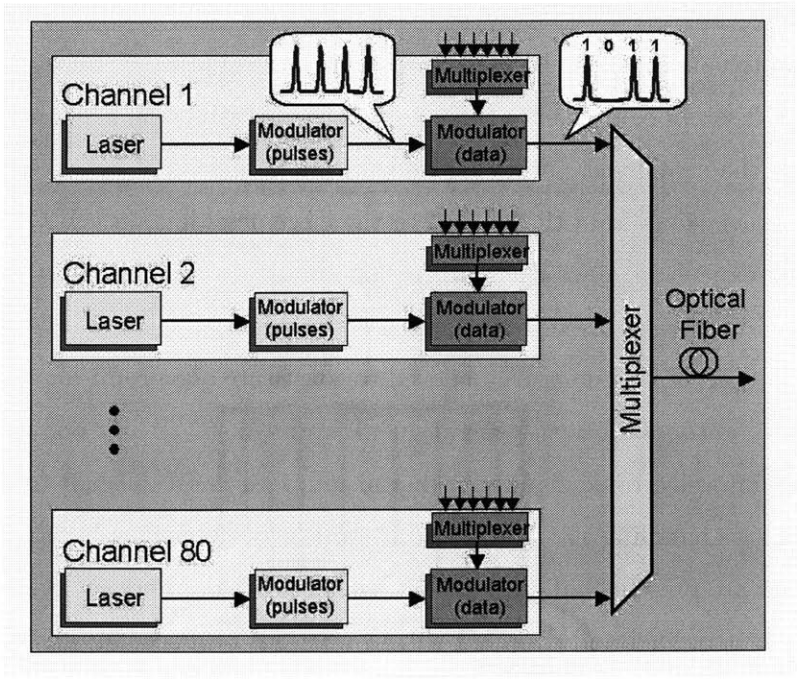

Figure 1-1: Conventional WDM transmission system composed of discrete components.

exclusively of voice data, transmitted from point-to-point. Traffic volume was highly predictable and the static network infrastructure combined with the prevalent SONET standard were well suited for transmission. However, the volume of data traffic is now about to surpass that of voice traffic and even the latter is increasingly shifted towards packed-based protocols such as voice-over-internet-protocol (VoIP) [4]. As a result, overall optical traffic adopts the characteristics of data traffic, resulting in rapid fluctuations of traffic volume and of geographic distribution and in the need for quality-of-service (QoS) differentiation between different data streams. To accommodate these new traffic patterns, a highly flexible network is required, that allows for optical package routing and for IP-style "plug and play" addition of new equipment [6]. Furthermore, rapid variations in traffic volume demand for a network that automatically adapts to traffic fluctuations and operating conditions rather than relying on manual load balancing and dispersion compensation [9, 10].

1.1.2 Potential of electronic-photonic integration

None of these challenges, neither the need for significant cost reductions, nor the need for a flexible, adaptive network can be addressed with the current static network infrastructure, composed of discrete components (Fig. 1-1a). The overall cost of this architecture is too high, due to the significant packaging and installation costs of discrete components. In particular, conversions from the optical to the electronic domain (OEO-conversions) are prohibitively expensive, since each conversion entails several functions, that each would have to be realized with discrete, expensive components.

However, OEO-conversions are believed to constitute one promising way to realize the vision of fully automated next generation networks [5, 6, 7]. By converting an optical data stream into electronic signals, a digital interface is established to the optical network that allows handling the traffic and network management in highly flexible manner: Since all data are present in digital format, the network becomes software-reconfigurable. Channels can be added and dropped within fractions of a second, additional nodes can be inserted into the network with low effort, individual packets rather than entire channels can be routed, and different transmission protocols, for voice and data, could coexist

next to each other. To realize this vision, the cost for OEO-conversions has to be drastically reduced, allowing each node of the network to be equipped with an inexpensive OEO-converter and intelligent switching logic. The required cost-effectiveness can be realized by means of co-integration of a large number of electronic and photonic functions in an electronic-photonic integrated circuit (EPIC). Similar to all-electronic integrated circuits (ICs), EPICs unify a large number of functions on a single chip. Their wafer-scale economies and the elimination of discrete packages yield the desired cost reductions for next generation networks. Section 1.1.3 discusses the advantages and architecture of a transmission system composed of EPICs fabricated in the silicon materials platform, supplied by high repetition rate mode-locked lasers with light.

An alternative approach, targeting the opposite, the complete elimination of OEO-conversions, is presented in section 1.2: In next-generation *all-optical* networks data are fully routed and switched in the optical domain in an attempt to avoid OEO-conversions made out of costly discrete components. High repetition rate mode-locked lasers are highly attractive for this system architecture as well since they provide a highly stable train of short pulses for transmission.

1.1.3 WDM system based on high repetition rate mode-locked lasers

Two competing materials platforms are considered for next-generation electronic-photonic integrated circuits: For transmission spans up to 200 km in length, fully integrated large-scale PICs based on Indium Phosphide (InP) have been developed and recently been deployed commercially. A single integrated transceiver has been shown to be capable of handling all the traffic of 10 WDM channels at an aggregate data rate of 100 Gbit/s [5, 7]. The advantage of InP is, that all passive and active optical functionality can be integrated on a single semiconductor chip, including lasers for transmitters, fast optical electro-absorption modulators and high-speed control circuitry. In the above-mentioned system deployed by the startup company Infinera, an InP chip incorporates all optical functionality, while a second chip, based on silicon-germanium (SiGe) technology, contains

all control logic, offering a fully digital electronic interface to the optical network layer [5].

In contrast, PICs based on silicon (Si), the standard materials platform of the microelectronics industry, are still in the development phase. Silicon is highly attractive for photonic applications, since it is superior to InP in terms of fabrication cost, fab infrastructure and waveguide loss. Silicon offers the potential of a seamless co-integration of both the optical and electronic functionality of a complete transceiver on a single semiconductor chip [11, 12, 13, 14, 15]. The low cost of silicon-based circuitry and the maturity of silicon fabrication technology promise the full integration of complete microprocessors handling the logic part of a switch with a PIC interfacing the optical layer on a single chip.

However, unlike InP, commercially viable lasers are currently not available in the silicon platform. Silicon is an indirect semiconductor [16] and instead of direct band transitions emission from dopants such as Erbium [17, 18] is needed to obtain stimulated emission. Alternatively, Raman effects are currently under investigation [19, 20, 21, 22] in the pursuit of a silicon laser. This lack of optical sources in silicon requires a separation of the generation of light, serving as the carrier in optical communications, from the PIC comprising all other optical and electronic components. This need coincides with the long-held desire for a compact, inexpensive and robust multi-wavelength source capable of supplying all channels of the WDM system with light [23, 24, 25, 26, 27]. All multi-wavelength sources share the principle, that a single laser generates light at all frequency components within the desired transmission bandwidth. The individual wavelengths are then demultiplexed (sliced) in an optical filter bank and a different data stream is added to each wavelength component before the channels are eventually re-combined and transmitted. Initial research towards spectrally sliced multi-wavelength sources focussed on incoherent sources, such as amplified spontaneous emission (ASE) sources based on erbium-doped fiber amplifiers (EDFAs) [25, 28]. However, the noise limitations imposed by the spontaneous-emission beat noise [25] triggered a change in focus towards supercontinuum sources [29, 26, 30] and the use of mode-locked lasers [31, 32, 33, 24, 34, 35, 23, 27].

Mode-locked lasers are highly attractive as multi-wavelength sources because of their

broad optical spectra, their inherently low timing jitter [36, 37] and their potentially chirp-free, Fourier-limited pulse quality. First transmission experiments with mode-locked lasers employed a fiber laser at repetition rates in the 30 MHz-range and demonstrated the chirped-pulse WDM scheme (CP-WDM) [31, 32, 33, 24, 34, 35]: Pulses from a mode-locked laser source are highly stretched in time by propagation through a dispersive fiber, such that different spectral components are mapped to different time-slots. Then, a fast modulator is used to encode the data. Since data added to an individual channel within one period are carried by different spectral components, different replica of the modulated signal can be delayed with respect to each other and multiplexed to achieve a combination of WDM and optical time-domain multiplexing (OTDM), reaching a data rate of up to 2.35 Gb/s over 100 parallel channels [33, 24, 34].

Most recently, bulk mode-locked lasers at multi-GHz repetition rates have been developed [38, 39, 40, 41, 27], that operate at the clock frequency of the optical network, for example at 10 GHz or 40 GHz. This way, the CP-WDM transmission scheme can be

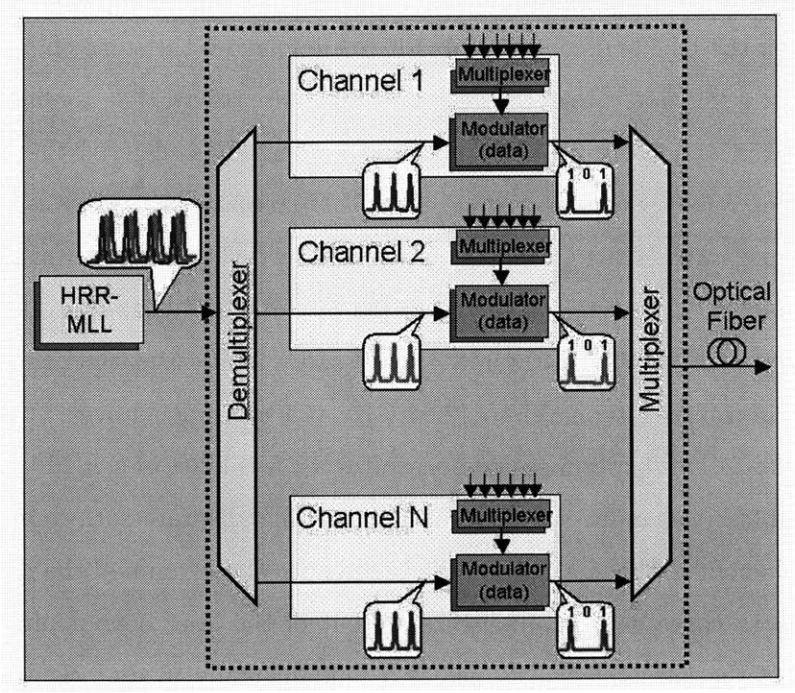

Figure 1-2: Proposed architecture of future communications system composed of a mode-locked high repetition rate laser (yellow) and a single silicon chip (all other components).

greatly simplified, and the strong dispersive broadening of the pulse train can be avoided alltogether [27]. These sources pave the way towards highly compact, robust and inexpensive transmitters that may facilitate the ubiquitous use of inexpensive OEO-conversion in the future (Fig. 1-2): A high repetition rate mode-locked laser (HRR-MLL) serves as a broadband light source spanning the entire transmission spectrum to be utilized, for example the C-band of optical communications. It emits sub-picosecond pulses at the clock frequency of the system or at an integer fraction thereof. In the PIC, located on the transceiver chip (indicated by a dashed line in Fig. 1-2), the spectral components of the pulse train from the HRR-MLL are separated into different channels by a de-multiplexer composed of arrayed waveguide gratings (AWGs) [42, 43] or micro-ring resonator filters [44, 45]. The 193.1 THz (1552.52 nm) center frequency of the filter array and the distance between adjacent channels (multiples of 12.5 Ghz) are chosen to match the ITU-grid [46]. Each channel now carries a pulse train of distinct center wavelength. Determined by the narrow filter width for each channel, the pulses can be significantly broadened, but the filter width is chosen to prevent pulse-to-pulse interference. Fast modulators [47, 48, 49], integrated on the PIC and controlled by drive circuitry on the same chip, encode streams of data at the repetition rate of the laser onto the pulse trains, that are finally re-combined in a multiplexer and transmitted to their destination. A decade after the proof-of-concept experiment of WDM with femtosecond pulses [23], recently the transmission of 1.36 Tb/s over 32 channels with 42.64 Gb/s has been demonstrated with a transmission scheme similar to the one of Fig. 1-2 [27]: The repetition rate of a 2.67 GHz mode-locked Cr^{4+}:YAG laser was increased to 10.67 GHz in a 4:1 free-space interleaver, then encoded with data, stepped up in a fiber interleaver to 42.64 GHz and transmitted over 32 channels, carved out by an AWG. This experiment demonstrates the feasibility of using high repetition rate mode-locked lasers as multi-wavelength sources in high bit-rate data communications and reveals the benefit of this approach: The broad optical spectrum of the mode-locked laser permits one to carve each channel directly out of the laser output and the high repetition rate of the laser allows the use of a fundamentally mode-locked laser. The long upper-state lifetimes in solid-state mode-locked lasers at telecommunications wavelengths lead to very low effective timing jitter of the pulse train since pump noise is filtered out

[36, 37]. A high extinction ratio of the pulses is common, since the pulses are generated in the mode-locked laser where the noise in the RF-spectrum is typically suppressed by over 70 dB. In contrast, pulse trains generated by electro-optic modulators frequently offer extinction ratios as small as 10 dB. Furthermore, passive mode-locking prepares the data from the beginning for return-to-zero (RZ) modulation, giving access to robust modulation formats, that reduce the effects of third-order nonlinearities in fiber transmission [50]. Finally, and most importantly, the pulses from the mode-locked laser can be chirp-free, allowing for minimum dispersive pulse broadening upon long-haul transmission. The high pulse quality clearly distinguishes a transmission system based on a mode-locked laser from InP-based integrated transmitters. Here, the change of refractive index in electro-absorption modulators during switching leads to large chirp of the pulses, leading to undesired intersymbol interference (ISI) upon long propagation distances. In contrast, the chirp-free pulse train emitted by the system composed of HRR-MLL and silicon-EPIC is equally well suited for short-haul and long-haul transmission [51].

In summary, HRR-MLLs are highly attractive multi-wavelength sources for optical communications, especially in combination with EPIC-based transceivers. Since both the silicon EPIC and the HRR-MLL can be manufactured cost-effectively [52], this approach promises to significantly reduce the costs for each switching node of the network, facilitating frequent use of OEO-conversions (section 1.1.2). This way, the proposed communications system contributes to the vision of a highly intelligent, fully automated optical network.

1.2 Application of high repetition rate mode-locked lasers in OTDM systems

In the previous sections the platform composed of high repetition rate mode-locked lasers and EPICs was proposed to lower the cost of optical transceivers via large scale photonic integration. This approach aims at offering an electronic interface to the physical layer of the multilayer protocol stack in order to extend existing network management techniques

directly into the optical domain. The availability of a large fraction of the required building blocks and its straightforwardness make this approach attractive for deployment in the near future to alleviate the challenges outlined in section 1.1.1. However, this platform does not fully utilize all the advantages offered by networks built in the optical domain, namely the capability of all-optical packet switching. The latter offers a different set of solutions to the issues mentioned in section 1.1.1. It allows to combine data streams of guaranteed bandwidth with on-demand services, to increase the data rate in each channel and to extend the transmission distance via all-optical signal regeneration [53]. While the use of EPICs in multi-channel WDM networks promises near-term commercial benefits, all-optical networks are currently the object of intense research without definitive plans for actual deployment in the short run.

The fast, all-optical switching capability of all-optical networks removes the limitations on modulation speed in a single channel, allowing to increase the data rates far beyond 100 Gb/s. For example, in [54, 55] transmission with 1.28 Tb/s over a single channel has been demonstrated. The larger channel bandwidth opens the way to multiplexing in the time domain, optical time division multiplexing (OTDM). Transmission at these data rates over large distances requires stable and chirp-free pulses to avoid ISI between neighboring time slots [51]. Therefore, high repetition rate mode-locked lasers are ideal sources for high-speed OTDM networks. Consequently, the work towards high repetition rate lasers presented in this thesis represents milestones both for the development of EPIC-based multi-wavelength WDM networks as well as a contribution to future all-optical OTDM networks.

1.3 Application of high repetition rate mode-locked lasers in optical AD conversion

Apart from applications in optical networks, HRR-MLLs are considered as key components in next-generation high-speed optical analog-to-digital converters (ADCs). The performance of electronic ADCs at GHz sampling rates is fundamentally limited by the

timing jitter of the electronic clock signal [56]. Timing jitter is an uncertainty in the temporal position of the trigger signal, that converts to errors in the sampled values of the analog signal. For example, at 10 GHz sampling rate the electronic timing jitter of approximately 1 ps limits the resolution of the sampled signal to less than 6 bits. In contrast, the timing jitter in mode-locked lasers can be as low as 10 fs [36, 37], permitting an increase in sampling resolution to 11 bits at 1 GHz sampling rate [56].

To exploit the superior jitter characteristics of mode-locked lasers, optical AD conversion schemes are currently investigated [57, 58, 59]. Wavelength division multiplexed time-interleaving photonic sampling is based on the idea of encoding fast analog signals to different frequency components of the optical carrier, permitting an array of slower ADCs to be employed for digitization [57, 58]. A possible implementation based on integrated

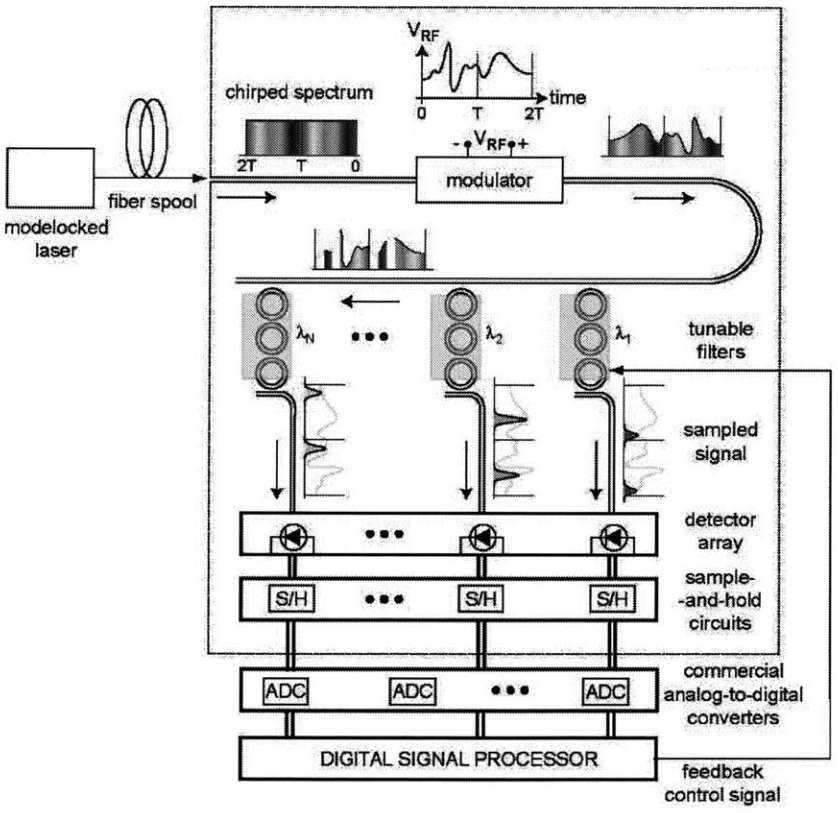

Figure 1-3: Architecture of WDM time-interleaved photonic sampling [1].

electronic-photonic circuits is shown in Fig. 1-5. A high repetition rate mode-locked laser generates a pulse train at the repetition frequency f_R. The pulses are dispersively broadened in a fiber and passed through a fast modulator that encodes the analog signal on the pulse train. Temporal variations within the sampling period T are encoded onto different wavelengths (Fig. 1-5), which are separated by an array of N micro-ring resonator filters, spectrally slicing the pulse train. The demultiplexed WDM channels carry N interleaved pulse trains at the repetition frequency, which serve as the input to a photodectecor and sample-and-hold circuit array. After AD conversion of the individual channel signals by means of ADCs, clocked at the repetition rate of the laser, the digital signals are interleaved, resulting in an aggregate real-time sampling rate of $f_s = M \cdot f_R$. Parallel AD conversion of the individual channels enables the use of slow but precise electronic sampling, while maintaining an overall data rate in the GHz range. Besides low timing jitter of the mode-locked laser, high repetition rates are required to reach high data rates with this sampling technique: The channels of the WDM filter must be separated by at least the maximum sampling rate f_s [57]. This limits the maximum number of parallel WDM channels, since the mode-locked laser provides only a limited optical bandwidth. To reach highest data rates despite this constraint, repetition rates f_R in the GHz-range can be required. Thus, the development of HRR-MLLs marks a key step towards the realization of multi-GHz optical AD-converters.

1.4 Mode-locked microchip and waveguide lasers

The development of high repetition rate mode-locked lasers in general opens the wide variety of applications outlined in sections 1.1 - 1.3 to ultrafast technology. Different approaches to the construction of high repetition rate mode-locked lasers are the focus of ongoing research: Harmonically mode-locked fiber lasers reach the high repetition rates required in the proposed applications but suffer from larger timing jitter than fundamentally mode-locked lasers [60]. The latter have proven to work up to 50 GHz repetition rate at the communications wavelength in discrete cavities with carefully optimized saturable absorbers [40]. Combined with laser gain media that have long upper state lifetimes,

the technical noise emerging from the pumping process is strongly filtered and reduced, such that very low jitter levels can be achieved, as demonstrated recently in an actively stabilized 10 GHz repetition mode-locked bulk Erbium-Ytterbium:glass laser, achieving a timing jitter of 26 fs (6Hz - 1.56 MHz) [61]. Finally, the third class of lasers competing for deployment as future high repetition rate sources are mode-locked semiconductor lasers. Pulses as short as 185 fs have been demonstrated [62] and 60 discrete channels could be carved out of the broad optical spectrum of a mode-locked semiconductor laser [63], yet the fast gain dynamics render the generation of short and energetic pulses more difficult than in mode-locked solid-state lasers.

While each class of lasers offers distinct benefits, we envision future high repetition rate systems to be based on very compact, fundamentally mode-locked, bulk solid-state lasers. These systems offer highest performance with respect to all relevant criteria: Fundamental mode-locking permits a low timing jitter, and the long upper state lifetime in erbium-ytterbium:glass, the common gain medium at the communications wavelength, results in strong suppression of pump noise. Furthermore, in Chapter 6 of this thesis we present the first Er-Yb:glass laser emitting a broad spectrum that covers the C-band of optical communications, allowing pulse trains feeding all channels to be carved out of the spectrum emitted by the laser. In addition, here we report the first semiconductor saturable absorber in the Si-SiO_2-Ge materials system that allows for monolithic integration of the saturable absorber with the gain medium, since the materials are fully compatible and permit mutual wafer bonding. For the future, we envision the mode-locked high repetition rate laser to consist of a monolithic cavity comprising gain element, saturable absorber and output coupler. The compact integration of all elements leads to the robustness mandatory for wide commercial deployment under harsh environmental condition, exposing the laser to shock, temperature variations and humidity. Thus, targeting a laser at the communications wavelength, all concepts discussed in this thesis are geared towards the fabrication of fundamentally mode-locked erbium-ytterbium:glass lasers monolithically integrated with semiconductor saturable absorbers as the mode-locking element. Compatibility with the silicon materials system furthermore permits the monolithic integration of the laser with a silicon - silicon dioxide PIC on the same substrate, a property

none of the other high repetition rate technologies offers. In the following two sections we outline two possible cavity designs of our envisioned lasers as well as the challenges posed by their fabrication.

1.4.1 Cavity setups

The cavity of the microchip laser consists of a bulk gain medium, to which the end mirrors are directly attached [64, 65] (Fig. 1-4). The round trip time and thus the repetition rate of the laser are determined by length and refractive index of the gain medium. For example, the cavity of a 40 GHz Erbium:glass (Er:glass) microchip laser would be 2.5 mm long (index $n = 1.521$). One side of the gain medium is covered with a dielectric coating that simultaneously serves as pump mirror and as output coupler. From this side the laser is pumped, *e.g.* the Er:glass laser with 980 nm pump diodes. Pump beam and output beam are multiplexed and separated outside of the cavity with dichroic mirrors. To initiate and stabilize mode-locking in the microchip laser, a saturable Bragg refelector (SBR), that provides an intensity dependent loss [66, 67], constitutes the other end mirror of the laser cavity. For laboratory experiments the SBR can be butt-coupled to the gain medium, but the requirements for stability and robustness of a commercial product would ask for attachment by wafer bonding. To date, microchip lasers have

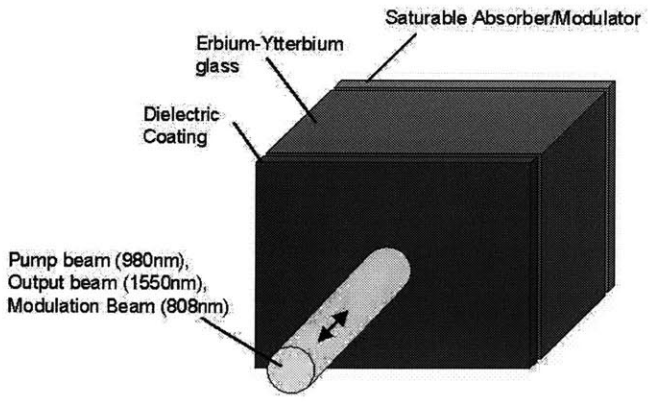

Figure 1-4: Schematics of the mode-locked microchip laser.

demonstrated superior performance as single-frequency, continuous-wave (cw) lasers [64] and in Q-switched operation [68, 69]. However, the challenge of stabilizing a mode-locked microchip laser against Q-switching instabilities [70, 71] has prevented the construction of a cw mode-locked microchip laser to date.

Like microchip lasers, waveguide lasers are composed of a cavity that monolithically integrates all functional elements of the laser. The gain element is a glass waveguide, doped with rare earth ions such as Erbium (Er) or Ytterbium (Yb) or a combination thereof. The waveguide is deposited on a substrate material of lower refractive index to ascertain mode confinement to the active region. The substrate can either be a quartz wafer, or a silicon wafer, covered with a sufficiently thick SiO_2 layer, obtained either by oxidation or deposition. In fully integrated waveguide lasers, indiffused or etched waveguide gratings form end mirrors of the cavity, or when hybrid integration is employed, one of the end mirrors may be attached as a separate component to the chip. The same holds for the incorporation of saturable Bragg reflectors, which may be fabricated monolithically on the base substrate of the waveguide laser, or hybridly attached. Similar to the microchip laser, pump and laser light are multiplexed outside the laser cavity, *e.g.* in a waveguide coupler integrated on the same substrate. The possibility of using silicon wafers as substrates for waveguide lasers renders them highly attractive as laser sources for EPICs: On a

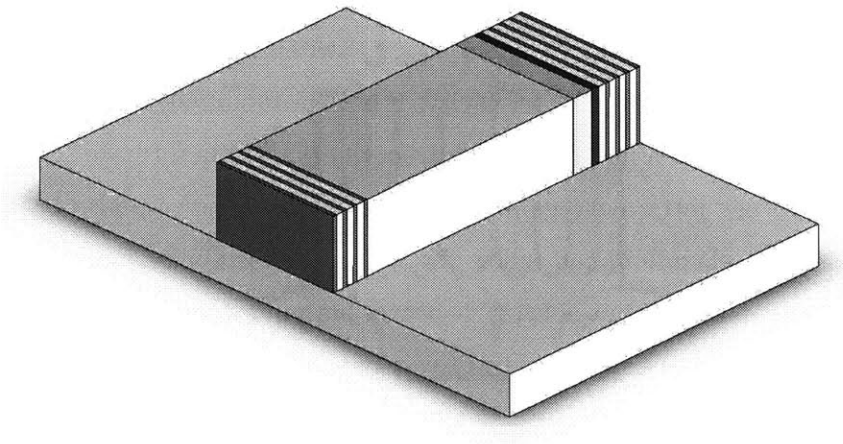

Figure 1-5: Schematics of the mode-locked waveguide laser.

single silicon chip a complete EPIC can be built, consisting of microprocessor and control electronics as well as of a photonic integrated circuit. In a subsequent fabrication step, the mode-locked waveguide laser can be integrated on the same substrate to supply the EPIC with an optical pulse train (sections 1.1 - 1.3). Waveguide amplifiers, consisting only of the gain section of a waveguide laser, are deployed in optical communication networks today. Their small size and weight make them ideal as preamplifiers for detectors and as amplifiers that compensate for losses in passive PICs. Mode-locking has to date only been demonstrated in waveguide lasers with extended cavities, where the waveguide amplifier served as the gain element [72, 73]. Mode-locking of 1.5 μm waveguide solid-state lasers at the fundamental repetition rate, determined by the length of the gain medium, has not been shown to date, due to the issues outlined in the following section.

1.4.2 Challenges to passive mode-locking and monolithic integration

The high repetition rates and the monolithic character of microchip and waveguide lasers lead to two significant challenges in mode-locking of these devices, that have been addressed in this thesis.

(i) First of all, the high repetition rate of these lasers combined with the long upper state lifetime, typical for solid-state gain media at communications wavelengths, lead to a high susceptibility to Q-switching instabilities. Q-switching can arise from the presence of a saturable absorber (SA) in the laser cavity. It is an instability of net gain and intracavity power that results when a fluctuation in intracavity power can saturate the saturable loss faster than the net intracavity gain, limited in its dynamic response by the low-pass character of gain relaxation, can follow [74, 70]. This instability manifests itself in the emission of giant pulses from the laser. It occurs both in cw lasers and as a superposition to mode-locking. The susceptibility to Q-switching is particularly pronounced in 1.5 μm high repetition rate lasers mode-locked with saturable absorbers, since the short round trip time allows changes in net gain to become effective on timescales, to which the net gain of the laser cannot respond due to its long upper state lifetime. This problem is further

magnified in waveguide lasers by the large amount of saturable loss, that is needed to offset the large linear losses in this type of cavity. Different schemes of Q-switch stabilization, including strong saturation of the SA [74, 70, 75, 76], the addition of an inverse saturable absorber [77, 78, 79, 80, 81, 82, 83, 84] and the use of an active feedback loop controlling the gain of the laser [65, 85, 86], have been demonstrated to date. While applicable to discrete laser cavities at intermediate repetition rates, all these schemes fail in the multi-GHz microchip or waveguide lasers targeted in this thesis (Chapter 2). To unify the plethora of approaches to laser stabilization, in this thesis the dynamics of the SA mode-locked laser are studied from a control systems viewpoint (Chapter 2). A feedback scheme, controlling the intracavity loss of the laser, is introduced first in theory and then validated experimentally in Chapters 3 and 4. Unlike the feedback stabilization via gain control this scheme extends even to highest repetition rates, and is thus also applicable to mode-locked microchip and waveguide lasers.

(ii) The other major challenge to the fabrication of mode-locked microchip and waveguide lasers is the monolithic integration of gain medium and saturable absorber. To satisfy the requirements of robustness and reliability, the absorber must either be wafer-bonded to the gain medium or must be created in the same fabrication process as the laser itself. The latter holds especially in the case of the waveguide laser. In both cases, full compatibility between materials systems of absorber and gain medium is required. This condition is violated in traditional III-V semiconductor-based saturable Bragg reflectors [87], motivating the quest for a new, materials system for SBRs. In this thesis we report the fabrication of the first saturable absorber in the Si-SiO_2-Ge materials system that offers full compatibility and potential for future integration with the erbium-doped gain media envisioned for mode-locked microchip lasers (Chapter 5).

1.5 Thesis outline

To unify the existing approaches to laser stabilization, this thesis begins with the analysis of laser stability in the framework of control systems theory. The control systems method gives qualitative insights to the origin of Q-switching instabilities and it renders

the plethora of tools in control systems engineering available to problems of laser stabilization. Once the control systems perspective is introduced, we use it in Chapter 2 to analyze different methods of laser stabilization, and review approaches that have been demonstrated to date in the control systems context: We discuss the stability condition of the laser mode-locked with a slow saturable absorber by means of root-locus and frequency response techniques and use them to derive the well-know stability condition. We then proceed with an analysis of stabilization via active feedback controlling gain and intracavity loss. In particular, we derive a criterion that allows us to decide which active stabilization scheme is most applicable to a given laser system. We conclude our theoretical analysis with a discussion of passive laser stabilization via inverse saturable loss.

The control systems analysis of laser stability in Chapter 2 identifies active laser stabilization with an intracavity loss modulator as a control scheme, that is universally applicable to lasers deep within the unstable regime, *i.e.* multi-GHz repetition rate lasers. In Chapter 3 we demonstrate for the first time the stabilization of such an unstable laser, operating three orders of magnitude apart from stability, with active feedback controlling the intracavity loss. An acousto-optic modulator (AOM) controls the intracavity losses in a mode-locked Erbium-waveguide laser, allowing for suppression of noise by 40 dB in a laser that exhibits Q-switching instabilities when the controller is not engaged. Robust stabilization is demonstrated and stability over the entire parameter range of the system is attained by means of an automatic gain control. This experiment shows that active feedback can eliminate instabilities on a slow timescale without negatively affecting the fast pulse shaping dynamics at the laser repetition rate. Suppression of noise is limited in this experiment by the narrow bandwidth that results from phase lag and propagation delay in the AOM. In Chapter 4 a fast Lithium-Niobate electro-optic modulator replaces the AOM. Its wide control bandwidth allows suppression of noise by over 75 dBc, showing that actively stabilized lasers can reach noise characteristics similar to passively stabilized systems. In summary, in Chapters 2-4 we demonstrate both theoretically and experimentally that active laser stabilization via control of intracavity loss can reliably suppress Q-switching instabilities. This stabilization scheme is universally applicable even at high-

est repetition rates and reaches a noise performance equal to that of passively stabilized systems. The control electronics developed for high performance feedback systems, optimized for wide bandwidth, low group delay and low excess noise, is discussed in appendix A.

The other major challenge to the fabrication of integrated microchip and waveguide lasers, the materials compatibility of gain medium and saturable absorber, is addressed in Chapter 5. We have developed a process for wafer-scale fabrication of silicon—silicon dioxide high reflectors with 99.8% peak reflectivity and over 700 nm bandwidth at the communications wavelength. Combined with a germanium absorber layer, these reflectors form the first saturable Bragg reflector in the silicon-germanium materials system to date. Their unparalleled optical bandwidth combined with their sub-picosecond recovery time, render them highly attractive for use as a fast saturable absorber in mode-locked lasers in general. Moreover, their materials are fully compatible with doped glasses in mode-locked microchip and waveguide lasers, solving the integration challenge outlined above. The CMOS-compatibility of their fabrication process makes them attractive candidates for a variety of applications in electronic-photonic integrated circuits. The silicon-germanium saturable absorbers were used to mode-lock a bulk Erbium-Ytterbium:glass laser (Chapter 6), producing the shortest pulse in this class of lasers to date. An optical spectrum spanning the C-band of optical communications was observed. It demonstrates the potential of mode-locked Erbium-doped glass lasers as multi-wavelength sources that provide a pulse train with components across the entire spectrum of optical communications.

In summary, this thesis has addressed critical challenges in the areas of laser stability, materials compatibility and laser performance. The solutions presented in the following Chapters pave the way to the fabrication of fully integrated mode-locked microchip and waveguide lasers.

Chapter 2

Theory and suppression of Q-switching instabilities in mode-locked lasers — a control systems approach

2.1 Introduction

The suppression of Q-switching instabilities is one of the key challenges to the construction of solid-state mode-locked lasers with multi-GHz repetition rates, such as mode-locked microchip and waveguide lasers (section 1.4.2). The commercial application of these lasers, *e.g.* in next-generation optical communication systems and high-speed optical analog-to-digital converters (sections 1.1 - 1.3), requires a reliable and robust mode-locking mechanism, which is provided by the use of saturable Bragg reflectors (SBRs) [66, 67]. However, at the high repetition rates required by these applications, SBRs lead to instability — especially in cavities with large saturable losses, in laser media with long upper state lifetimes and at low intracavity power.

The basic stability condition of the SA mode-locked laser was derived by Haus in 1976 [74], and since then a number of active and passive stabilization schemes, targeting

an extension of the stable regime to the operating point of the desired laser, have been demonstrated. However, none of them provides the reliability, robustness and versatility needed for stabilizing high repetition rate lasers against Q-switching: The simplest scheme, the strong saturation of the saturable absorber (SA) [74, 70, 75, 76, 88, 89] aims at a reduction of the saturation slope at the operating point of the laser. This scheme allows the extension of the stable regime, but fails in bulk microchip and waveguide lasers at the targeted repetition rates in the multi-GHz regime (section 1.4). An alternative stabilization approach, the use of inverse saturable loss [77, 78, 79, 80, 81, 82, 83, 84], *e.g.* two-photon or free carrier absorption, leads to a very narrow window of laser parameters, between Q-switching instabilities on one side and breakup into multiple pulses on the other. In lasers with discrete cavities, manual fine-tuning allows one to reach this stable operating regime. However, due to monolithic integration of microchip and waveguide lasers the key parameters of the laser, such as spot size on the absorber and repetition rate are fixed, such that the operating conditions of the laser are set after completion of the fabrication process. This lack of tunability prevents the use of stabilization via inverse saturable loss in these cavities, since the narrow operating window is difficult to meet without higher flexibility. Finally, it has been proposed to suppress Q-switching instabilities with active feedback stabilization [65, 85, 86], controlling the gain of the laser. While this scheme is straightforward to implement, and robust in application where it actually succeeds, it is not suitable in gain media with very long upper state lifetimes at the high repetition rates encountered in microchip and waveguide lasers.

Nevertheless, beyond a basic stability analysis [74, 70, 75] no further investigation of the laser dynamics has been undertaken. In this Chapter, a unified view of active and passive Q-switching suppression is presented, using linear control theory to model a SA mode-locked laser which is stabilized with active or passive techniques. This approach makes the well-established methods of control systems engineering accessible to the synthesis of robust stabilization schemes for mode-locked lasers. It also provides deeper insights into the general structure, the advantages and the limitations of active stabilization schemes. The control systems approach provides a unifying view on previous attempts to stabilization, whose discussion is included in the respective sections. This approach

provides guidelines for the choice of an optimal controller and identifies stabilization via intracavity loss modulation (section 2.6) as a universally applicable stabilization scheme.

Our discussion is opened with an introduction of saturable absorber mode-locking and a stability analysis of SA mode-locked lasers in the control systems context. First, a control systems representation of the laser rate equations is derived by means of transfer functions and block diagrams (section 2.3). Next, the stability of the laser without additional stabilization is examined in this framework (section 2.4). The discussion proceeds with active laser stabilization, either with a controller acting on the pump power [85, 65] (section 2.5) or by direct control of the intracavity loss (section 2.6) [73]. The general structure of these controllers and their applicability to different laser systems is studied, and design guidelines for controller gain and bandwidth are provided. Finally, the passive laser stabilization by inverse saturable absorption [77, 78, 79, 81] is examined in the context of control systems (section 2.7).

2.2 Mode-locking with a saturable absorber

We begin our discussion of laser stability with a brief conceptual introduction of mode-locking with a saturable absorber (SA), namely with a saturable Bragg reflector. To generate a steady pulse train from a laser, a highly nonlinear element, a saturable absorber, is added to the laser cavity. It offers a starting mechanism for formation of a pulse, it stabilizes the pulse — once developed — in the cavity and it shapes the temporal form of the pulse. The saturable absorber provides an intensity dependent loss that is the pre-requisite for passive mode-locking: For low pulse energies, or even continuous-wave (cw) light, the absorber merely adds loss to the cavity. In contrast, its loss is saturated in the presence of higher energy pulses. Therefore, a pulse is subject to lower round-trip losses than cw-light in the laser. Consequently, the energy balance is shifted towards mode-locking in the presence of a saturable absorber and pulsed operation of the laser constitutes the stable operating point. Mode-locking is typically examined in the context of Haus' master equation [90, 91, 74] describing the full temporal dynamics, containing much more detail than conveyed in the highly simplified discussion of mode-locking in

this section.

Numerous and highly performing mechanisms of saturable absorption have been developed, such as the fast processes of Kerr-lens mode-locking [92] and nonlinear polarization evolution [93]. However, for the compact and eventually monolithic integrated mode-locked high repetition rate lasers targeted in this thesis semiconductor saturable absorbers [66] offer the advantage that they can be integrated in a compact manner with the gain medium and that they offer a reliable self-starting mechanism of mode-locking. Deposited on a semiconductor substrate is first a Bragg reflector on top of which resides a bulk semiconductor layer or semiconductor quantum well (QW) in a peak of the standing wave pattern formed by the electromagnetic field (Fig. 2-1a). This absorber layer absorbs incident cw light. Its absorption properties can be adjusted via the material composition and the layer thickness. In contrast, high intensity pulses bleach the absorption of the bulk material or of the quantum well absorber layer via band filling, such that the absorption is saturated. If the saturable absorber is operated in reflection, *i.e.* if it is a saturable Bragg reflector, the device reflectivity increases as the absorption is reduced (Fig. 2-1b). In this reflective configuration the saturation is a function of fluence [1]. Ignoring linear losses, the intensity dependent reflectivity $R(F_A)$ is characterized as

$$R(F_A) = 1 - q(F_A) \ , \tag{2.1}$$

where $q(F_A)$ is the energy dependent loss for a certain fluence on the saturable Bragg reflector. Typical semiconductor saturable absorbers are slow SAs. Unlike in fast SAs their absorption does not react instantaneously to the incident pulse intensity, but instead it is bleached by the pulse, and has a slower recovery characterized by the absorber recovery time τ_A, as shown in Fig. 2-1c. For mode-locking a recovery time shorter than the cavity round trip time is needed, such that the SA fully recovers between two subsequent pulses. Since various techniques for shortening the recovery time exist [94, 95, 96], this condition can be fulfilled even for laser repetition rates $f_r = 1/T_R$ in the multi-GHz range. All computations in this Chapter are based on a slow saturable absorber, *i.e.* an absorber

[1] Pulse energy per unit area.

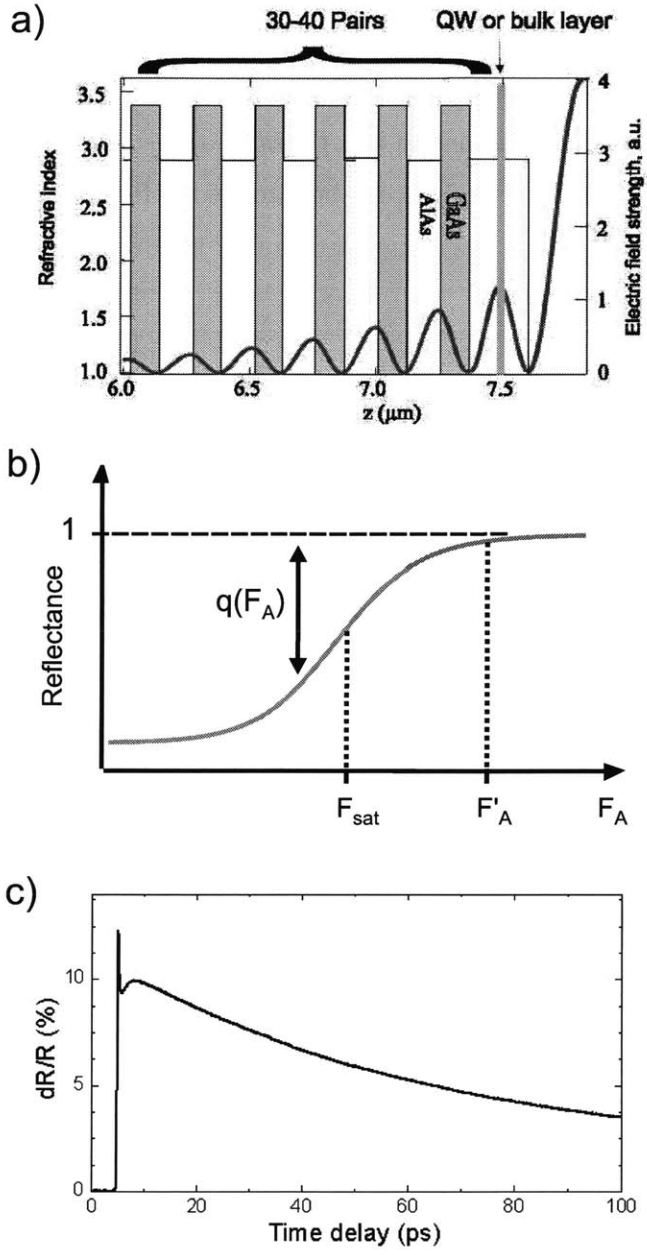

Figure 2-1: **a)** Typical semiconductor saturable absorber structure. **b)** Saturation characteristics (schematically) of typical semiconductor saturable absorber. **c)** Pump-probe trace of the saturable absorber employed of the experiment in Chapter 3.

whose recovery time τ_A is longer than the pulse duration τ_P. This absorber integrates over the pulse envelope and thus saturates as a function of pulse energy rather than responding instantaneously to the field intensity. This choice of a slow saturable absorber in our calculation is motivated by the robust self-starting behavior it offers in the monolithic integrated laser cavities envisioned in this thesis. However, with a calculation similar to the one presented in [78], our analysis can be extended to fast saturable absorbers as well. With these two assumptions, the saturable absorber in eq. (2.1) is fully characterized by the energy-dependent loss [70]:

$$q(W) = q_0 \frac{1 - \exp(-\frac{W}{E_A})}{\frac{W}{E_A}}, \tag{2.2}$$

where $E_A = F_{\mathrm{sat,A}}\, A_{\mathrm{eff,A}}$ denotes the saturation energy of the absorber, defined by the effective spot size $A_{\mathrm{eff,A}}$ on the absorber, and the saturation fluence $F_{\mathrm{sat,A}}$, which is defined by the structure and material parameters of the saturable absorber. In the following section begin our analysis of laser stability by introducing a model of the temporal dynamics based on which a control systems representation of the system is derived.

2.3 Representation of the SA mode-locked laser as a control system

Q-switching is an energy instability that can occur in both continuous-wave (cw) and mode-locked lasers. Due to the long upper-state lifetimes in solid-state lasers, the timescales for energy decay in the photon field and for changes in population inversion are typically much slower than the other degrees of freedom in the laser dynamics. The latter, comprising for example changes in pulse duration and nonlinearity, are damped and instantaneously follow the macroscopic conditions established by the interplay of pulse energy and gain in the cavity. Therefore, the temporal stability of a mode-locked laser is fully characterized by the rate equations representing the dynamics of pulse energy W in the

resonator and power gain g in the gain medium [74, 70], similar to a cw-laser:

$$T_R \frac{\partial W}{\partial t} = \Big(g - l - q(W)\Big) W \tag{2.3}$$

$$T_R \frac{\partial g}{\partial t} = -\frac{g - g_0}{T_L} - \frac{gW}{E_L}. \tag{2.4}$$

T_R denotes the cavity round trip time, t the time variable, g_0 the small signal gain and l the intracavity roundtrip power loss. The laser medium is characterized by the upper-state lifetime τ_L, the normalized upper-state lifetime $T_L = \tau_L / T_R$, and the saturation energy $E_L = A_{\text{eff,L}} F_{\text{sat,L}}$. Here, $A_{\text{eff,L}}$ represents the effective laser mode area, $F_{\text{sat,L}} = h\nu/(2\sigma_L^*)$ the saturation fluence in the gain medium, and ν the frequency of laser radiation. The stimulated emission cross section σ_L^* takes the values 2 and 1 in a linear and in a ring cavity, respectively.

For the subsequent analysis of the laser dynamics in the frequency domain, we linearize equations (2.3) and (2.4) at the steady state operating point $W = W_s + \Delta W$, $g = g_s + \Delta g$, $l = l_s + \Delta l$ and $g_0 = g_{0s} + \Delta g_0$ and then take the Laplace transform. Here, W_s, g_s, l_s, and g_{0s} represent the steady state values at the operating point, while the remaining terms denote the time-dependent deviations from these values. The resulting expressions describe the fluctuations of pulse energy $\widetilde{\Delta W} = \mathcal{L}(\Delta W)$ and gain $\widetilde{\Delta g} = \mathcal{L}(\Delta g)$ in frequency space, influenced by variations in loss $\widetilde{\Delta l} = \mathcal{L}(\Delta l)$ and small signal gain $\widetilde{\Delta g_0} = \mathcal{L}(\Delta g_0)$:

$$sT_R \widetilde{\Delta W} = -\frac{\partial q}{\partial W}\Big|_{W_s} W_s \, \widetilde{\Delta W} + W_s \, \widetilde{\Delta g} - W_s \, \widetilde{\Delta l} \tag{2.5}$$

$$sT_R \widetilde{\Delta g} = -\frac{g_s}{E_L} \widetilde{\Delta W} - \frac{1}{T_L'} \widetilde{\Delta g} + \frac{1}{T_L} \widetilde{\Delta g_0}. \tag{2.6}$$

In our analysis, we investigate the stability of pulse energy and gain against fluctuations, as well as the influence of active feedback stabilization with an additional controller. We rewrite the rate equations eq. (2.5) and eq. (2.6) in matrix form

$$sT_R \begin{pmatrix} \widetilde{\Delta W} \\ \widetilde{\Delta g} \end{pmatrix} = \begin{pmatrix} A_{11} & A_{12} \\ A_{21} & A_{22} \end{pmatrix} \begin{pmatrix} \widetilde{\Delta W} \\ \widetilde{\Delta g} \end{pmatrix} - \begin{pmatrix} G_l(s) \\ G_g(s) \end{pmatrix} \widetilde{\Delta W} \tag{2.7}$$

where the first term represents the interplay between pulse energy and gain and the second

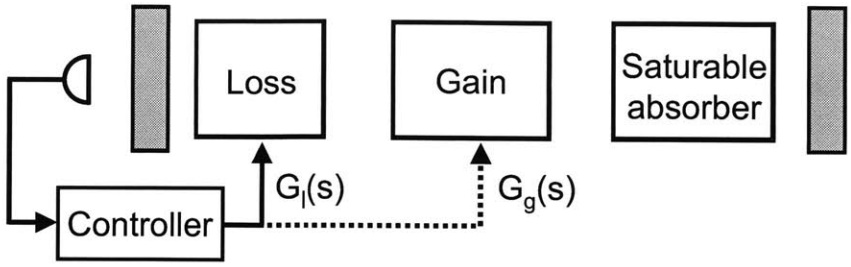

Figure 2-2: Schematics of the active feedback stabilization via gain or loss control

the influence of the active controller. In this linearized model, the action of the controller is treated as proportional to $\widetilde{\Delta W}$, since the control electronics monitors the output power of the laser and responds to fluctuations thereof (Fig. 2-2). The feedback system either acts on a loss modulator controlling the intracavity loss via Δl or it acts on the gain of the laser via Δg_0 by changing the pump power. The corresponding transfer functions of the controller are denoted as $G_l(s)$ and $G_g(s)$ in eq. (2.7), while the matrix elements A_{ij} are given by

$$A_{11} = -\left.\frac{\partial q}{\partial W}\right|_{W_s} W_s$$
$$= q_0 \frac{1-(1+\frac{W_s}{E_A})\exp(-\frac{W_s}{E_A})}{\frac{W_s}{E_A}} > 0 \tag{2.8}$$
$$A_{12} = W_s > 0 \tag{2.9}$$
$$A_{21} = -\frac{g_s}{E_L} < 0 \tag{2.10}$$
$$A_{22} = -\frac{1}{T_L'} = -\frac{rT_R}{\tau_L} < 0 \tag{2.11}$$

where $r = 1 + P/P_{sat,L}$ is the pump parameter. The terms A_{11} and A_{22} represent the action of the saturable absorber and of gain relaxation, and express the interaction of pulse energy and gain: The saturable absorber lets a growing pulse energy ΔW grow even further ($A_{11} > 0$), while the effects of increasing gain are dampened by gain relaxation ($A_{22} < 0$). In contrast, the terms A_{12} and A_{21} stand for the coupling from gain to pulse energy fluctuations and vice versa. While the feedback terms $G_g(s)$ and $G_l(s)$ for both

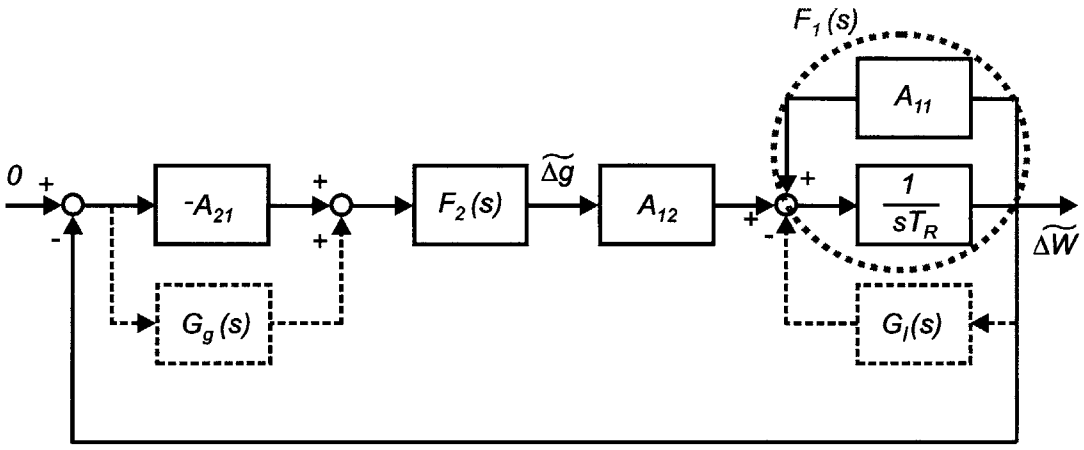

Figure 2-3: Block diagrams of the laser (solid lines) with feedback controllers (dashed lines) in standard feedback form with unity gain in the feedback branch. All blocks of the system contain terms of positive sign.

gain and loss modulation appear in eq. (2.7), only one of the two feedback methods will be used in a practical implementation of the feedback stabilization scheme at a time. The comparison of the rate equations eq. (2.5) and eq. (2.6) with eq. (2.7) yields the relations

$$\widetilde{\Delta l} = G_l(s)\,\frac{\widetilde{\Delta W}}{W_s} \tag{2.12}$$

$$\widetilde{\Delta g_0} = -T_L\,G_g(s)\,\widetilde{\Delta W}\ . \tag{2.13}$$

between pulse energy fluctuations ΔW and the quantities controlled by the feedback stabilization, Δl and Δg_0 in the frequency domain. This pair of equations determines loss and gain variations as functions of controller gain $|G_{g,l}(s)|$ and the spectrum of pulse energy fluctuations $\widetilde{\Delta W}$ and allows us to calculate the required modulation depth for a given stabilization scheme (sections 2.5 and 2.6).

The laser system is transformed into a block diagram (Fig. 2-3) in standard feedback form [97, 98], by solving the linearized rate equations eq. (2.7) for $\widetilde{\Delta W}$ and introducing

the transfer functions

$$F_1(s) = \frac{1}{sT_R - A_{11}} \ , \ A_{11} > 0 \tag{2.14}$$

$$F_2(s) = \frac{1}{sT_R - A_{22}} \ , \ A_{22} < 0 \ . \tag{2.15}$$

All functional blocks lie in the forward branch of the system, while the feedback branch exhibits unity gain and negative feedback. The control system represents fluctuations Δg and ΔW of gain and pulse energy in the frequency domain — since both vanish in equilibrium, the system tracks a zero input signal (Fig. 2-3). Solid lines represent the behavior without additional controller, while dashed lines indicate the behavior with active stabilization by gain or loss feedback. The input for either controllers is the spectrum of pulse energy fluctuations $\widetilde{\Delta W}$. The active control of loss modulation $G_l(s)$ is a cascaded subsystem immediately counteracting $F_1(s)$, while the gain controller $G_g(s)$ lies in the forward branch of the loop parallel to A_{21}. Based on this control systems representation, we will analyze laser stability and stabilization in the following sections. Root locus plots serve for the discussion of general controller structure, while frequency response techniques are employed to derive requirements for the controller bandwidth [97, 98]. We illustrate the application and limitations of different stabilization schemes with three example laser systems whose parameters are summarized in Table 2.1.

2.4 Stability of the laser without additional stabilization

We begin our discussion of laser stability with the analysis of Q-switching instabilities in lasers without additional feedback control. The basic stability condition for this class of lasers was derived by means of the Routh-Hurwitz criteria [97] by Haus [74]. This approach allows to determine the boundaries of the stability region, but fails to convey a more detailed understanding of the origin of Q-switching dynamics. To alleviate this shortcoming, we introduce the perspective of control systems theory used throughout our

Table 2.1: Parameters of Lasers

	laser A	**laser B**	**laser C**
material	Nd:YVO_4	Yb:glass	Er-Yb:glass
repetition rate	100 MHz	1 GHz	40 GHz
T_R	10 ns	1 ns	25 ps
τ_L	100 μs	2 ms	8 ms
E_L	100 μJ	300 μJ	300 μJ
r	25	20	20
W_s	50 nJ	5 nJ	0.5 nJ
g_s	1%	1.5%	1%
q_0	0.5%	1.0%	0.5%
W_s/E_A	5	10	3

discussion of laser stability and present a stability analysis based on root-locus arguments and the frequency response technique. This view of laser stability offers qualitative insights into the individual system components contributing to stability or destabilization and thus shows different ways to stabilization of the cavity. The laser system without additional stabilization, given by solid lines in the block diagram of Fig. 2-3, is represented by the open-loop transfer function

$$\begin{aligned} F_0(s) &= -A_{12}A_{21}F_1(s)F_2(s) \\ &= -\frac{A_{12}A_{21}}{(sT_R - A_{11})(sT_R - A_{22})} \ . \end{aligned} \tag{2.16}$$

It has two system poles p_1 and p_2. The pole $p_2 = A_{22}/T_R$ is stable due to its negative real part [97, 98]. It represents the low-pass filter $F_2(s)$ established by gain relaxation in the laser medium [eq. (2.4)], which blocks fast variations in pulse energy ΔW from affecting the saturated gain g. Its corner frequency $\omega_2 = |A_{22}|/T_R = r/\tau_L$ [eq. (2.11)] corresponds to the inverse stimulated lifetime, that depends only on the pump parameter and the upper state lifetime of the gain medium. In media with long stimulated lifetime τ_L/r, such as rare-earth doped glasses (*e.g.* Er-doped or Yb-doped glasses), ω_2 can be as low as several kHz. Due to this low-pass filter, Δg only responds to slow variations in ΔW.

In contrast, the pole $p_1 = A_{11}/T_R$, representing the action of the saturable absorber, lies in the right half of the s-plane. The positive feedback A_{11} to the integrator $1/sT_R$ renders $F_1(s)$ unstable (Fig. 2-3): Fluctuations in pulse energy ΔW saturate the loss $q(W)$ in the absorber [eq. (2.2)]. As a result, the overall intracavity loss *decreases*, and the round-trip gain can *increase* if it is not balanced by subsequent fast gain saturation. Thus, the pulse energy fluctuation can grow more and more by further saturation of the loss $q(W)$ until a giant pulse, a Q-switch cycle, is established in the cavity. This positive feedback via A_{11} can destabilize the laser, leading to Q-switching instabilities [74, 70], as discussed in the following.

2.4.1 Stability via root-locus techniques

The open loop transfer function eq. (2.16) in standard feedback form allows the direct application of the root-locus technique [97, 98]. We include a discussion of this approach primarily for reasons of completeness — the frequency response technique (section 2.4.2) offers a more intuitive view on stability of the mode-locked laser. However, in the following we show, that the root-locus method allows to draw the same conclusions and leads to the same stability condition as the Routh-Hurwitz and frequency response methods. Since the root-locus technique is well suited to the design of active feedback controllers, we decided to include a discussion of the most basic case, the unstabilized laser, in this framework.

To apply the root-locus method to a standard feedback system [98], the open-loop transfer function $F_0(s)$ eq. 2.16 is factorized:

$$F_0(s) = k\,\frac{\prod_\mu (s - z_\mu)}{\prod_\nu (s - p_\nu)} = k\,\frac{P_0(s)}{Q_0(s)}\,, \tag{2.17}$$

where z_μ and p_ν denote the zeros and poles of $F_0(s)$ respectively. k contains all constant factors, including the gain of a feedback controller. In a standard feedback system the controller is typically a block in the forward branch of the open loop, such that changes in controller gain lead to variations of k. However, changes in k do not modify the position of the poles and zeros p_ν and z_μ of $F_0(s)$ in eq. (2.17). By solving the characteristic

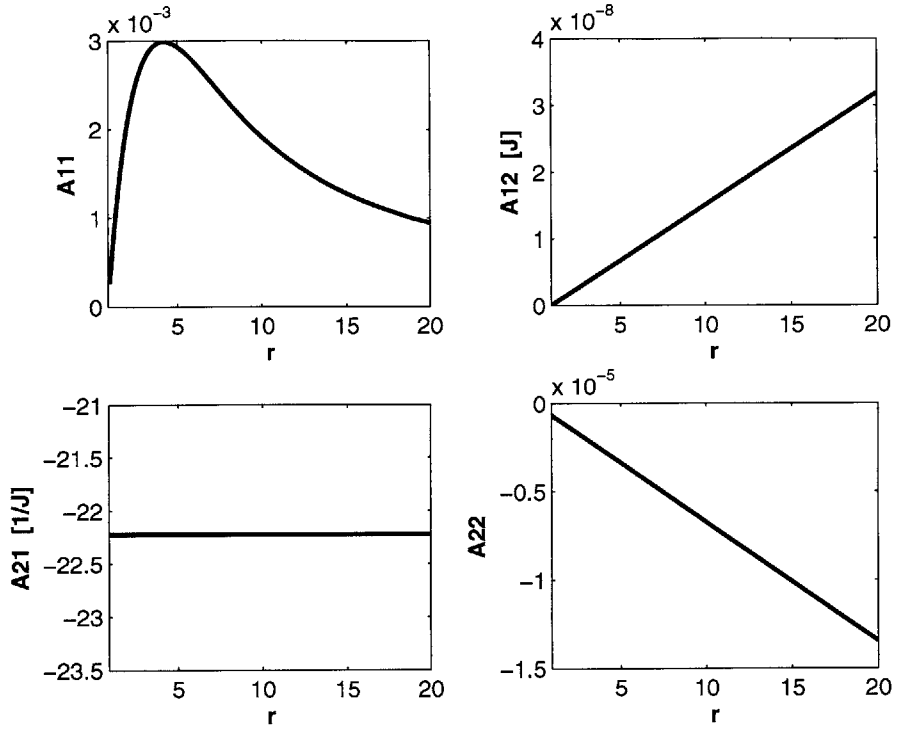

Figure 2-4: Matrix elements A_{ij} of the control system as function of pump parameter r.

equation

$$F_0(s) + 1 = 0 \tag{2.18}$$

the poles of the closed-loop transfer function eq. (2.16) are obtained for a given value of k. By solving (2.18) for all values of k and plotting the solutions in the complex s-plane, the location of poles of the closed-loop transfer function (2.16) can be tracked. Since each value of k corresponds to a certain value of controller gain, the root-locus plot obtained by this method gives insights in the system stability for different controller gains. The system is stable for values of k, for which all corresponding poles are located in the left half-plane. The beauty of the root-locus method is its power to show the location of poles as a function of controller gain. It allows to identify the stability regions of the overall closed-loop system from the open-loop transfer function.

When applied to the unstabilized mode-locked laser with SA, the root-locus technique can illustrate the position of system poles as a function of pump parameter $r = 1 + P/P_{sat,L}$, and thus show regions of stability and Q-switching. However, when r is varied,

not only the constant factor k in eq. (2.17) , containing all constant factors, changes. Instead, the location of system poles and zeros p_μ and z_ν in $F_0(s)$ varies as well. Fig. 2-4 shows the matrix elements A_{ij} determining the values of the system poles as a function of pump parameter r to illustrate this behavior. Since both the factor k and the location of poles and zeros in eq. (2.17) vary when r is changed, eq. (2.18) has to be evaluated for every value of r in order to calculate the root-locus of the SA mode-locked laser. As a consequence, the familiar rules for estimating the approximate root-locus [97, 98] do not hold in this case, and a computerized evaluation of eq. (2.18) is indispensable. Figure 2-5 shows the root-locus plot of laser A from Table 2.1 as a function of pump parameter r. The root locus emerges from the poles $p_1 = A_{11}/T_R$ and $p_2 = A_{22}/T_R$ calculated at $r = 0$. For very small values of r the system is stable, but then both poles move into the right half-plane, indicating instability. For $r > 14$ the poles cross the imaginary axis again, and the system is stable for all pump parameters above this threshold. This result fully agrees with the stability region obtained via the frequency-response method, as shown in Fig. 2-7a and discussed in section 2.4.2.

Finally, we can derive the well-known condition for stability against Q-switching in the root-locus framework. Considerations of asymptotic behavior [98] reveal that the system with two poles on the real axis can only be stable if the center δ between both poles is located in the left half of the s-plane:

$$\delta = \frac{p_1 + p_2}{2} = \frac{1}{2\,T_R}\,(A_{11} + A_{22}) < 0 \;\Leftrightarrow\; tr(A) < 0\,. \tag{2.19}$$

Evaluating this expression with (2.8) and (2.11) we obtain

$$-\left.\frac{\partial q}{\partial W}\right|_{W_s} W_s = q_0 \frac{1 - (1 + \frac{W_s}{E_A})\,\exp\,(-\frac{W_s}{E_A})}{\frac{W_s}{E_A}} < \frac{r T_R}{\tau_L}\;, \tag{2.20}$$

the well-known condition for stability against Q-switching in a laser mode-locked with a slow saturable absorber. However, while (2.20) guarantees that an asymptote would be located in the left half-plane, a second stability condition has to be met: The constant factor $k = A_{12}A_{21}\,/\,A_{11}A_{22}$ in eq. (2.17) must be large enough to ensure that the poles

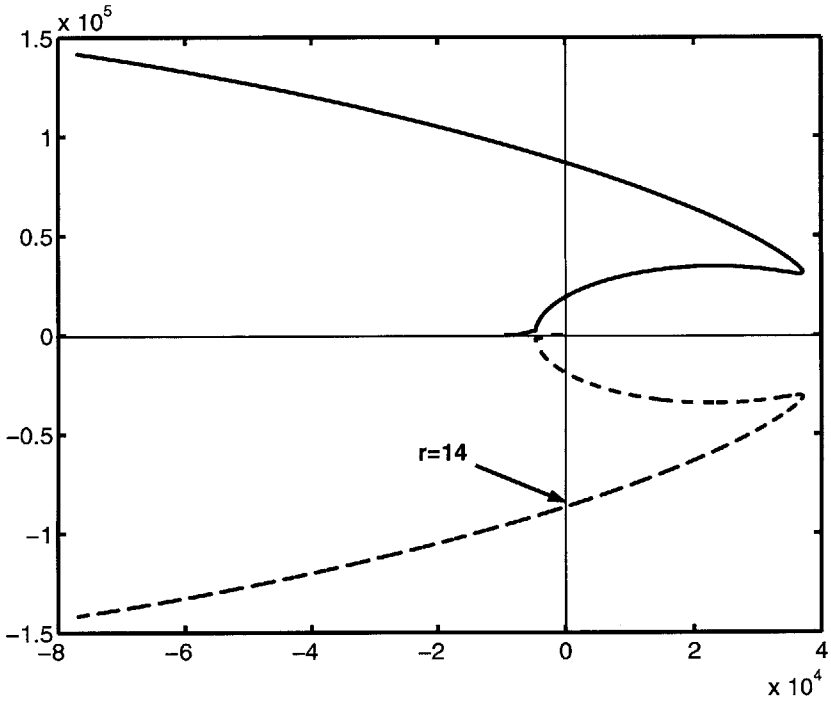

Figure 2-5: Root-locus plot of laser A from table 2.1 with saturable absorber only and no active feedback applied. For $r > 14$ both roots are located in the left half-plane, rendering the system stable.

are actually located in the left half-plane. To determine this second stability criterion, we calculate the value k' where the root-locus crosses the imaginary axis:

$$k' P_0(j\omega) + Q_0(j\omega) = 0 \ , \tag{2.21}$$

where we have set $s = j\omega$. Solving (2.21) for k' reveals

$$k' = -1 \ , \tag{2.22}$$

and thus the second stability condition, that the root-locus has actually crossed the imaginary axis, can be expressed as

$$k = -\frac{A_{12}\, A_{21}}{A_{11}\, A_{22}} > k' = -1 \Leftrightarrow \ det(A) > 0 \ . \tag{2.23}$$

With a short calculation this expression can be rewritten as

$$-\frac{\partial q}{\partial W}\bigg|_{W_s} < -\frac{\partial g}{\partial W}\bigg|_{W_s} \ , \tag{2.24}$$

which is fulfilled, if the gain saturates much stronger in the operating point than the saturable absorber. This condition is typically fulfilled [70, 76].

In summary, the root-locus method leads to the well-known stability criteria (2.20) and (2.23) for the laser mode-locked with a slow saturable absorber and provides a visualization of the pole distribution and thus the stability behavior of the laser as a function of pump parameter. However, the dependence of pole locations on the pump parameter r prevents plotting the root-locus with the approximate rules of thumb applicable to standard control systems [98, 97]. Instead, the root-locus has to be evaluated with a computer, in contrast to the design of active feedback controllers (section 2.5 and 2.6). In the latter case, the root-locus method can be applied in the usual manner, since only the constant factor k of eq. (2.17) but not the poles change with variations of the controller gain. The movement of the poles as a function of the pump parameter r greatly reduces the benefit of using the root-locus method in the unstabilized laser.

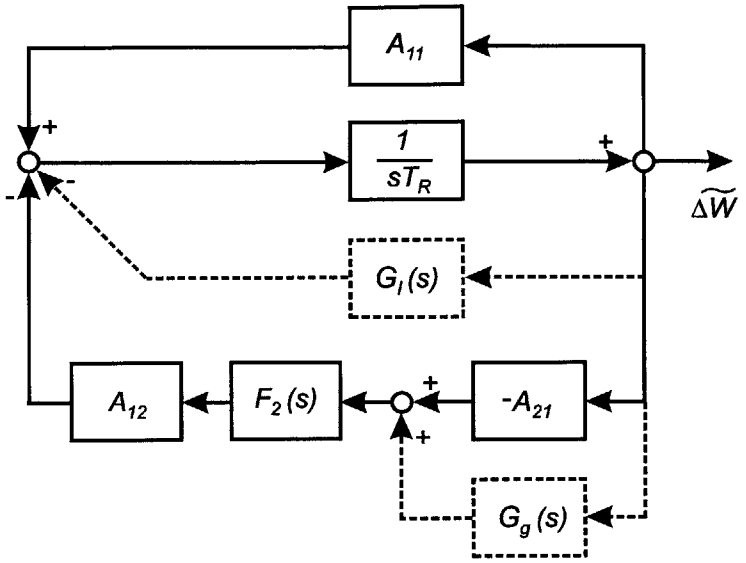

Figure 2-6: Modified block diagram of the laser (solid lines) with feedback controllers (dashed lines), containing only an integrator $1/sT_R$ in the forward branch.

2.4.2 Stability via frequency response techniques

The derivation of the stability criteria (2.20) and (2.23) with the root-locus method demonstrates that this method is applicable to the stability analysis of the SA mode-locked laser. However, further insight in the dynamic behavior of the laser, and into the factors leading to instability, can be gained from the frequency response technique.

The stability limits of the laser can be determined when both the saturable absorber A_{11} and the gain relaxation $A_{12}A_{21}F_2(s)$ are considered as feedback to the integrator $1/sT_R$, as shown in the modified block diagram of Figure 2-6. Besides illustrating the concept of parallel feedback from saturable absorber and gain relaxation, this system representation enables the application of frequency response techniques to the SA mode-locked laser: A Bode diagram of the control system is only meaningful, if all poles of the open-loop transfer function are stable [98]. This necessary condition is violated by the system in Figure 2-3 since $F_1(s)$ is unstable, but fulfilled in the modified systems

representation of Figure 2-6. Here, the open-loop system transfer function becomes

$$F_B(s) = \frac{1}{sT_R}\left(-A_{11} + \frac{A_{12}A_{21}}{A_{22}}\,\frac{1}{1 - sT_R/A_{22}}\right) . \tag{2.25}$$

As mentioned before, the saturable absorber, represented by the term $-A_{11}$ in eq. (2.25), destabilizes the system by means of positive feedback to the integrator (Fig. 2-6). In contrast, the gain relaxation branch $A_{12}A_{21}F_2(s)$ contributes to system stability by providing negative feedback (Fig. 2-6). An increase in pulse energy, ΔW, reduces the saturated gain g [see eq. (2.4)] and therefore prevents energy fluctuations in the laser from growing further, while the saturable absorber is found to enhance them. The stabilizing effect of gain relaxation is reflected in the positive sign of the term $A_{12}A_{21}/A_{22}$ in eq. (2.25). In fact, below the corner frequency ω_2 the laser is always stable, since the negative feedback from gain saturation exceeds that of the saturable absorber:

$$-A_{11} + \frac{A_{12}A_{21}}{A_{22}} > 0 \quad \Leftrightarrow \quad det(\mathbf{A}) > 0 . \tag{2.26}$$

This relation always holds, since in the steady state operating point the gain saturates more strongly than the saturable absorber does [74]. As a result, for $\omega \ll \omega_2$ the transfer function $F_B(s)$ accumulates a phase shift $\varphi_{F_B} < \pi$. We judge stability using the Nyquist criterion: A closed-loop system is stable if signals fed back from its output to its input, that experience greater than unity gain, have a phase shift $\varphi < \pi$ [97], [98]. Applied to the laser system of Fig. 2-6, the open-loop transfer function $F_B(s)$ in eq. (2.25) is stable under this criterion for $\omega \ll \omega_2$. While the system is stable at low frequencies, the stabilizing gain relaxation term $A_{12}A_{21}/A_{22}$ in eq. (2.25) is attenuated by the low-pass $1/(1 - sT_R/A_{22})$ at frequencies above ω_2. For $\omega \gg \omega_2$, the destabilizing effect of the saturable absorber A_{11} dominates the bracket in eq. (2.25) and the system becomes unstable.

Thus, to keep the laser stable, the term A_{11} must be attenuated below unity by the integrator $1/sT_R$ before the low-pass filter begins to reduce the stabilizing gain feedback term at frequencies above ω_2. To meet this condition, we demand that A_{11}/T_R falls below

unity gain at the corner frequency $\omega_2 = |A_{22}|/T_R$:

$$\left.\frac{A_{11}}{sT_R}\right|_{s=\omega_2} = \frac{A_{11}}{|A_{22}|} < 1 \quad \Leftrightarrow \quad tr(\mathbf{A}) < 0 \tag{2.27}$$

Evaluating this expression with eq. (2.8) and eq. (2.11) yields the well-known condition for stability against Q-switching in a laser mode-locked with a slow saturable absorber [70], [76]

$$-\left.\frac{\partial q}{\partial W}\right|_{W_s} W_s = q_0 \frac{1 - \frac{W_s+E_A}{E_A}\exp(-\frac{W_s}{E_A})}{\frac{W_s}{E_A}} < \frac{rT_R}{\tau_L}. \tag{2.28}$$

The left-hand side of this equation denotes the reduction of losses per round trip by saturation of absorption, whereas the right side represents the maximum additional saturation of the gain per round trip. The laser is only stable, if the gain saturates faster than the saturable loss — if the negative feedback via $A_{12}A_{21}F_2(s)$ exceeds the destabilizing effect A_{11} of the saturable absorber.

Our analysis of laser stability from a control systems viewpoint may be illustrated with an example. We have chosen a laser similar to the one published in [65], but have slightly adjusted the laser parameters to yield a larger difference between stable and unstable operation (laser A in Table 2.1). In the experiment, the laser was found to exhibit Q-switching instabilities at intermediate power levels, while it was stable at higher values of pump power around the operating point listed in Table 2.1. This behavior is readily understood from the stability condition eq. (2.27), which is studied in Fig. 2-7a: For low to intermediate pump power levels, the laser is unstable and Q-switching is observed in the experiment, since $A_{11} > A_{22}$. In contrast, for higher values of the pump parameter r the system reaches stability, since $A_{11} < A_{22}$.

The fundamental difference in the system state, between stable mode-locking and Q-switching, is shown in two exemplary cases in Fig. 2-7b and 2-7c. This figure shows the Bode plots of the individual terms of $F_B(s)$ in eq. (2.25) as well the the phase φ_{F_B} of F_B. In Fig. 2-7b the state of the unstable laser is shown for an intermediate pump parameter of $r = 5$. The reason for instability of the system becomes apparent when the Nyquist criterion is applied to $F_B(s)$: At the corner frequency of the low-pass filter

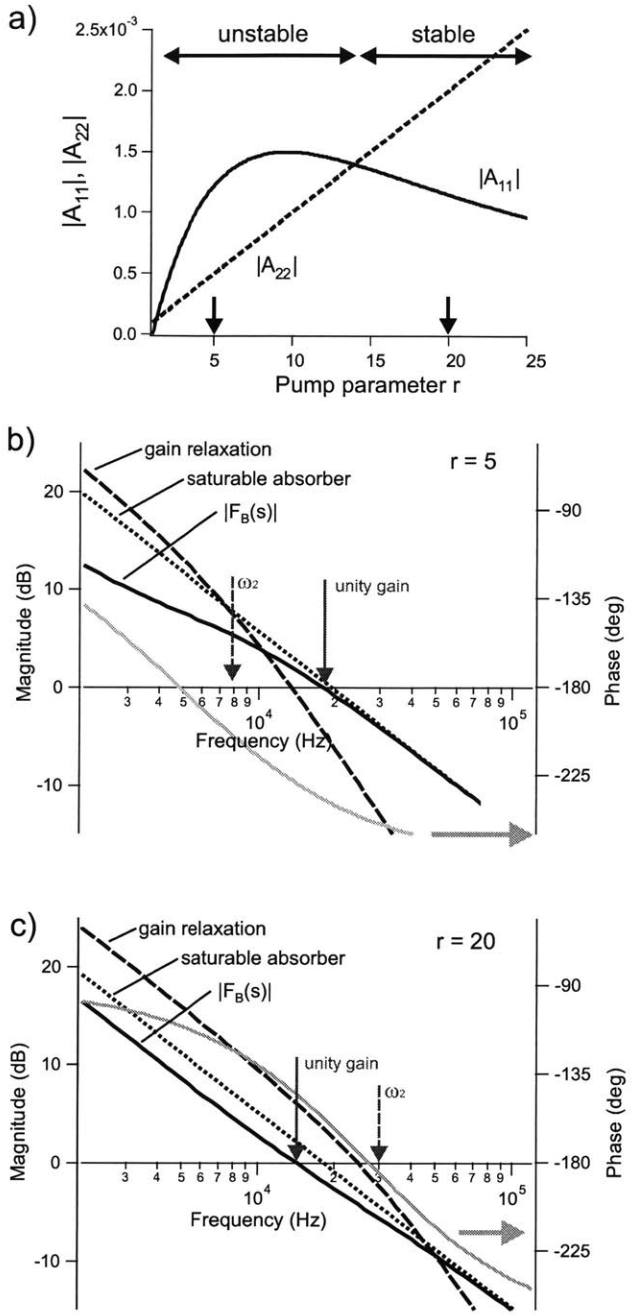

Figure 2-7: Stability analysis of laser A (Table 2.1). **a)** $|A_{11}|$ versus $|A_{22}|$ as a function of pump parameter r. **b)** Frequency dependence of the individual terms of $F_B(s)$ entering eq. (2.25) for the unstable laser at $r = 5$ and **c)** for the stable laser at $r = 20$. Stabilizing gain relaxation (dashed line), positive feedback from the saturable absorber (dotted line), $|F_B(s)|$ (solid black line) and $arg(F_B(s))$ (solid grey line).

$\omega_2 = 2\pi \cdot 8$ kHz, the positive feedback from the saturable absorber A_{11}/sT_R experiences a gain greater than unity, violating condition (2.27) as indicated by the dashed vertical line in Fig. 2-7b. At frequencies $\omega > \omega_2$ the saturable absorber begins to dominate $F_B(s)$, due to the attenuation of the stabilizing gain feedback term by the low-pass filter $F_2(s)$, and drives the phase φ_{F_B} rapidly towards -270deg. At the unity gain point of $F_B(s)$, indicated by the solid vertical line in Fig. 2-7b, φ_{F_B} has dropped below the critical value of -180deg, rendering the system unstable according to the Nyquist criterion. This detailed comparison of the competing influences from stabilizing gain feedback and destabilizing absorber effects show, that the Q-switching instability stems from the attenuation of the stabilizing gain feedback term by the low-pass filter $F_2(s)$.

In contrast, in the stable regime, illustrated for the pump parameter $r = 20$ in Fig. 2-7c, the destabilizing absorber term A_{11}/sT_R is attenuated below unity at the corner frequency of the low-pass filter $\omega_2 = 2\pi \cdot 32$ kHz. In this case the stability condition (2.27) is met. In comparison to the previous case A_{11} is smaller due to stronger saturation of the absorber, and ω_2 has grown from $2\pi \cdot 8$ kHz to $2\pi \cdot 32$ kHz. The laser system is stable, and gain saturation ensures system stability over the entire frequency range: Up to the unity-gain point of $F_B(s)$, indicated by a solid vertical line in Fig. 2-7c, the stabilizing gain feedback term dominates the open-loop transfer function. At this frequency, $F_B(s)$ experiences a phase of about -145 deg, enjoying a healthy phase margin of 35 deg. While we have chosen the laser parameters in this example to accentuate the difference between stability and Q-switching, the same considerations hold for the real laser system in [65], where the two regimes are closer together.

From this discussion of laser stability, two approaches for active feedback stabilization of the mode-locked laser emerge. (i) Stability can be achieved with a controller that mitigates the destabilizing effect of the pole A_{11}. This can be achieved by direct control of the intracavity loss (Fig. 2-6), when a branch of negative feedback $G_l(s)$ is added in parallel to the saturable absorber, instantaneously compensating for the destabilizing positive feedback. (ii) Alternatively, a filter $G_g(s)$ can be introduced in the gain saturation branch (Fig. 2-6) to compensate for the low-pass filter $F_2(s)$ and thus to extend the stabilizing feedback via gain relaxation over a wider frequency range. In the following

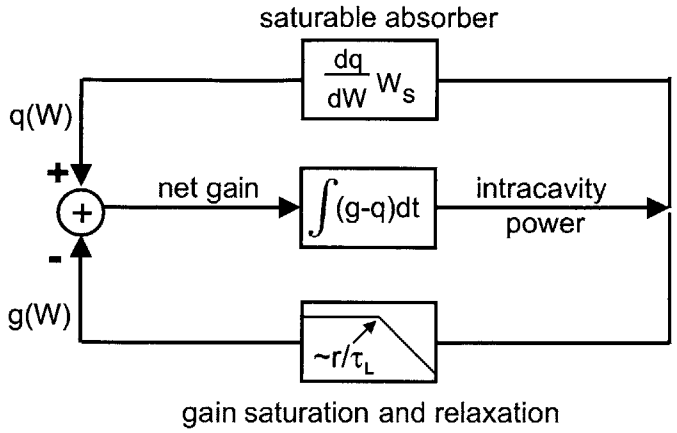

Figure 2-8: Simplified version of the control system of Fig. 2-6.

section, we continue our discussion by first introducing the stabilization via gain control.

2.4.3 Time-domain perspective of laser stability

So far we have discussed laser stability only in the control systems context in the frequency domain. Before we proceed with the discussion of laser stabilization by active or passive control schemes, in this section we briefly summarize, what stability or instability means in the time domain and how it manifests itself in the laser. To address physical intuition rather than applying the rigid formalism of control systems theory, we have re-drawn the system block diagram of Fig. 2-6 labelled with the laser components responsible for the dynamics rather than the corresponding matrix elements (see Fig. 2-8).

The desired, stable state of the laser, cw mode-locking with a saturable absorber (SA), is shown in the left column of Figure 2-9. The timescale of the processes shown in the figure (Fig. 2-9a) extends about one order of magnitude beyond the pulse duration. Thus, the full scale shown in this schematic might correspond to 10 ps in a typical high repetition rate laser, where about 1 ps pulse duration can be expected. The gain assumes a fixed value and does not fluctuate, neither when a pulses passes nor on a longer timescale. Like the gain, the intracavity power is fixed since the laser is stable: All the energy stored in the electromagnetic field is concentrated within the pulse circulating in the cavity (dashed

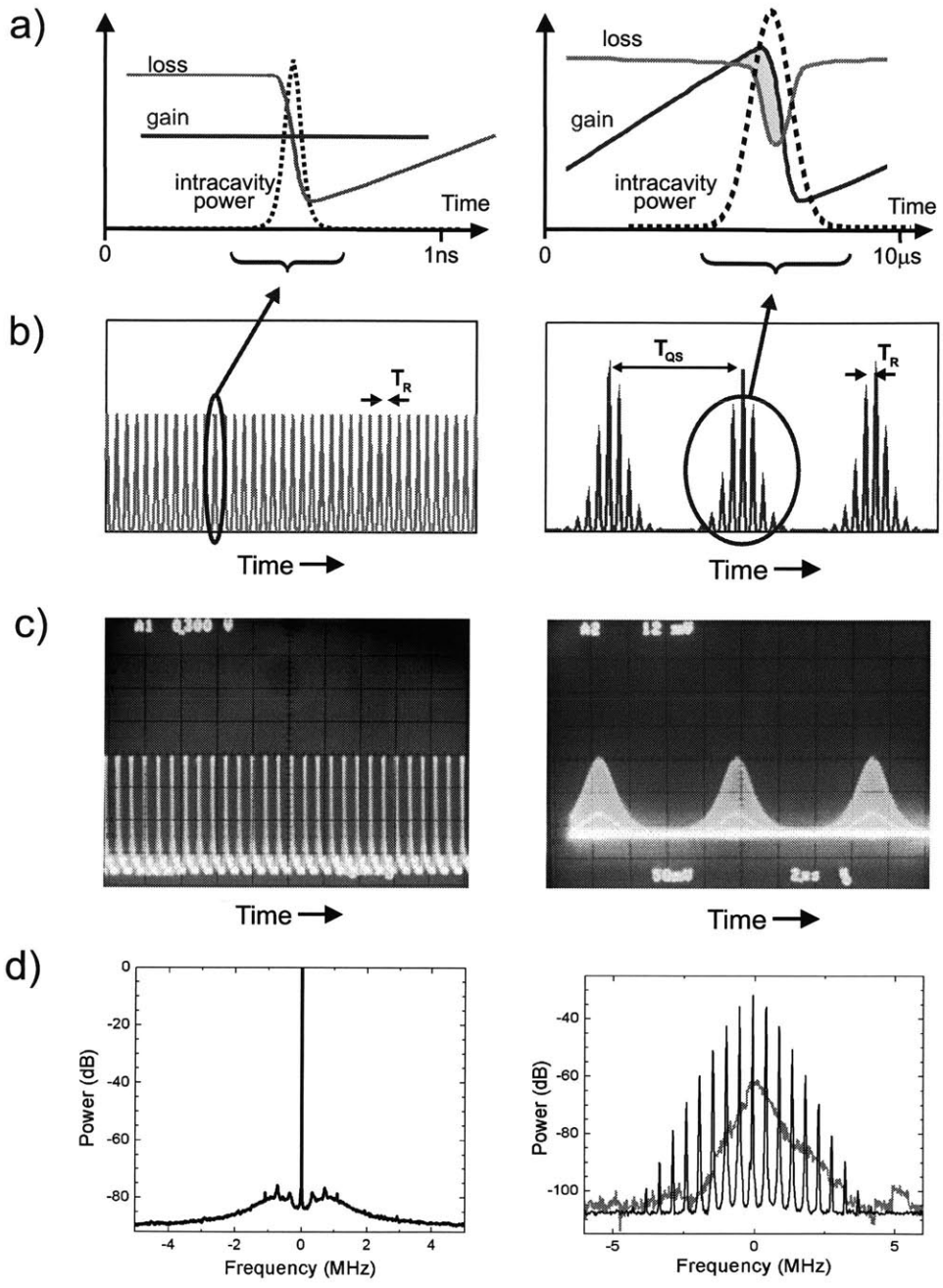

Figure 2-9: cw mode-locking (left column) and Q-switched mode-locking (right column) of the laser. **a)** Dynamics of gain, loss and intracavity power during a pulse (left) or a Q-switch cycle (right). **b)** Simulated mode-locked pulse train (left) and train of Q-switch cycles (right). **c)** Oscilloscope traces of the mode-locked pulse train and the envelope of Q-switch cycles. **d)** Microwave spectrum of the cw mode-locked laser (left) and of two different Q-switch mode-locked lasers.

line). While concentrated within a picosecond or less, the overall value of intracavity power remains constant over the time of multiple roundtrips. In contrast, when a pulse hits the saturable absorber, the latter saturates and opens a net gain window due to its slow recovery time (a slow SA was assumed), in which the pulse but not the surrounding background on a larger timescale, the continuum [99], is amplified. The stable cw mode-locked state is characterized by constant values of gain and intracavity power, the two 'state' variables in Fig. 2-8. As a result, the laser emits a highly stable and regular train of pulses, each pulse with the same power and duration (Fig. 2-9 b and c, left). Individual pulses are separated by the cavity round trip time T_R. While Fig. 2-9b was obtained by simulation of the temporal dynamics, Fig. 2-9c depicts an oscilloscope trace taken from the stabilized waveguide laser discussed in Chapter 3. The regularity of the pulse train is reflected in the microwave spectrum of the pulse train, consisting of frequency components at multiples of the laser repetition rate. Figure 2-9d (left) shows the RF spectrum within a 10 MHz bandwidth around the repetition rate of the laser. To allow for comparison with Q-switched lasers at different repetition rates (Fig. 2-9d, right), the frequency axis is normalized to the repetition rate. The noise, resulting from perturbations of the ideal state is suppressed by over 75 dBc in this laser, indicating highly stable operation.

In contrast, the unstable, or Q-switched state of the laser is characterized by large fluctuations of gain and intracavity power (Fig. 2-9, right column). As mentioned in the previous section, the instability is caused by an excessive amount of positive feedback of the saturable absorber (see also Fig. 2-8), preventing the laser from ever reaching a stable state. The dynamics of Q-switching can be illustrated with Figure 2-9 a (right), showing the evolution of a Q-switch-cycle. The timescale of the processes shown covers the inverse of the Q-switch repetition rate, ranging from 10 kHz to 1 MHz in lasers with 100 MHz ... 10 GHz repetition rate. Thus, a timeframe of about 1 μs ... 100 μs, much larger than in the cw mode-locked case, is shown in this figure. For the initial state at $t = 0$ in this example we assume a depleted gain, either after the laser is just turned on or after a Q-switch cycle just passed. The gain is pumped and when it reaches the level of the overall cavity loss, at threshold, the intracavity power builds up in the cavity. Increasing intracavity power saturates the loss in the SA. The saturation of loss in the SA occurs instantaneously, since

the SA responds directly to the incident fluence (Fig. 2-8). Therefore, the saturation of loss follows the incident fluence immediately and also recovers instantaneously. If the system were to be stable, the gain would also saturate instantaneously via gain saturation as the intracavity power grows. However, the response of the gain is limited in its speed by the low pass filter established by gain relaxation (Fig. 2-8), such that former cannot follow the fast increase in intracavity power. As a result, decreasing intracavity loss, yet steady gain lead to a widening of the net gain window between gain and overall cavity loss (gray shaded area in Fig. 2-9a, right). As a result, the growing pulse is amplified even further, leading to yet higher saturation of the SA. This way, a giant pulse builds up in the cavity that fully saturates the SA. Eventually, with an effective delay caused by the low-pass filter, the gain saturates as well and falls well below the level it would assume in steady state. A giant pulse, a full Q-switch cycle, has developed. Now, the initial conditions of Fig. 2-9a (right) are restored — the gain has fallen below the losses, the laser is below threshold and the entire cycle is repeated. The Q-switch cycles form an envelope under which mode-locking can still persist (Fig. 2-9b). To the right of Figure 2-9c an oscilloscope trace of a highly regular Q-switched laser is shown. While the envelope of each Q-switch cycle is apparent, individual pulses are invisible in this trace, due to the long recording timescale: Each Q-switch cycle lasts for about 2 μs, while the round trip time in this cavity was on the order of 10 ns. Thus, a single Q-switch cycle lasts about 200 round trips, whose pulses cannot be discerned at this resolution. The high regularity of Q-switching is repeated in the microwave spectrum (black trace to the right of Fig. 2-9d). The mode-locked pulse train leads to evenly spaced frequency components at multiples of the laser repetition rate, here at zero-frequency due normalization of the frequency axis. The Q-switched pulse formation leads to an additional modulation of this pulse train, that manifests itself as additional sidebands to the repetition rate, separated by the Q-switch repetition frequency, here about 450 kHz [2]. Besides the microwave spectrum of a regular Q-switched laser, Fig. 2-9d shows the RF spectrum of a laser that is spiking and Q-switching in a very irregular manner (gray trace). Here, the individual Q-switch

[2]For a detailed discussion of the Q-switching repetition rate and its dependence on the round trip time see section 2.6.

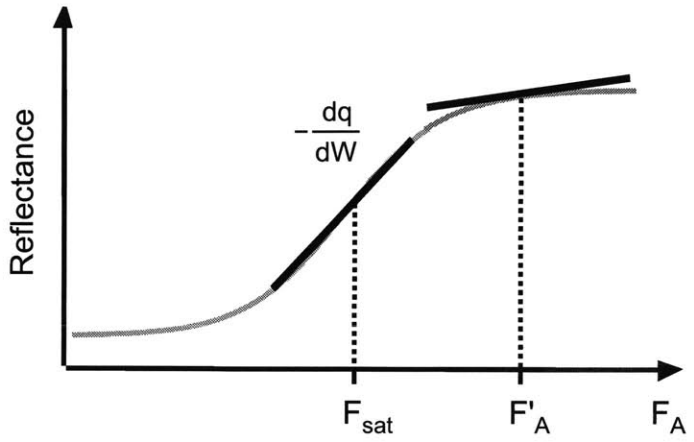

Figure 2-10: Reflectance vs. fluence response of the saturable absorber. Black lines indicate the slope of the saturation curve.

sidebands cannot be discerned, and in fact, the oscilloscope showed a highly irregular occurrence of giant pulses. Such irregular instabilities were encountered much more often in the lasers discussed in Chapter 3, than the regular one depicted in Fig. 2-9c.

The discussion of the Q-switched laser shows, that Q-switched mode-locking is in fact a superposition of two independent phenomena, the mode-locked pulse formation at the laser repetition rate and the Q-switching instability at a much lower frequency. The active control systems discussed in sections 2.5 and 2.6 aim at suppressing the instability of the intracavity power envelope without disturbing the fast mechanism of mode-locked pulse formation.

2.4.4 Implications for laser stabilization via strong saturation of the SA

The stability condition eq. (2.28) of the SA mode-locked laser without additional stabilization points to different ways of stabilizing this system. The variables on the right hand side of eq. (2.28) are predetermined in a given laser system: Upper state lifetime τ_L and pump parameter r are determined by the chosen laser medium and output coupling ratio.

The cavity round trip time T_R results from the desired repetition rate, *e.g.* 10 GHz or 40 GHz in lasers for next generation optical communication systems (section 1.1). The same holds for the pulse energy W_s on the left of eq. (2.28) — it depends fully on the chosen repetition rate and the intracavity power reached in a given operating state. Thus, only the term $\partial q/\partial W$, the slope of saturable loss in the operating point, can be chosen within certain limits.

One way of reducing the destabilizing effect of the SBR is a reduction of the modulation depth q_0 of the saturable absorber. In high repetition rate lasers at optical communications wavelengths this can be achieved by adjusting the absorption coefficient of the common absorber material, out of which the quantum well region is typically grown, $In_xGa_{1-x}As$, via the Indium content. However, a lower limit for the saturable loss is given by the need for sufficient pulse shaping of the SBR and by its ability to stabilize the laser: Lower values of q_0 have a smaller effect on the incident pulse and lead to longer pulse durations [100]. Furthermore, a certain amount of saturable loss is required to compensate for filter losses and to stabilize the pulse against a breakthrough of the continuum [99, 101], establishing a minimum value for the appropriate amount of saturable loss.

Instead of decreasing the overall saturable loss q_0 in the SA, the saturation slope $\partial q/\partial W$ can also be reduced by operating the laser at a larger fluence incident on the SA. This is illustrated in Fig. 2-10 for the two fluence values F_{sat} and F'_A of a fictitious SA: For an incident fluence exceeding the saturation fluence by an order of magnitude or more, the absorption slope is significantly reduced, and with it the amount of destabilizing, positive feedback (compare also Fig. 2-8). This strong saturation of the saturable absorber, which might be implemented as a saturable Bragg reflector (SBR), may be achieved by focusing the laser mode onto a small spot on the SBR, for example onto a spot of less than 10 μm in Gaussian waist. However, hard focussing leads to a high thermal load on the SA, that can result in long-term thermal damage and a change of the absorption characteristics of the SA due to heating [88]. The danger of thermal damage is particularly pronounced in highest repetition rate lasers, since the pulse energy and hence the fluence on the SBR decrease inversely proportional to the repetition rate, requiring for harder and harder focusing to reach a high fluence. To avoid these detrimental effects, numerous attempts

have focused on a reduction of the saturation fluence F_{sat} itself, allowing strong saturation F_A/F_{sat} to be reached with larger spots. It has been shown that the deposition of an anti-reflection coating [102, 103] or even a resonant coating [72] on top of the fabricated SBR lead to the desired result. An additional top-reflector forms a cavity around the quantum well(s) in combination the back-mirror of the SBR, leading to a higher field intensity. This way, saturation fluence values as low as 1 μJ/cm^2 have been demonstrated. A further reduction of saturation fluence has been demonstrated by use of self-assembled quantum dot absorbers, permitting fluence values as low as 1.7 μJ/cm^2 [104], while typical fluence values of saturable absorbers grown in III-V or group-IV semiconductor materials without modification are about 30 μJ/cm^2.

This discussion shows that a careful selection of the operating point of the saturation curve (Fig. 2-10) and special designs of saturable absorbers allow to extend the stable regime, by up to one or two orders of magnitude. However, this approach requires either a laser cavity with a small mode size on the SBR or special absorbers, with resonant coatings or particular quantum dot band edge engineering. In the robust laser cavities for commercial applications, such as microchip and waveguide laser (section 1.4.1), the spot size on the absorber is given by the size of the laser mode due to a monolithic cavity setup. Thus, the spot size on the absorber cannot be chosen at random. Furthermore, hard focussing on the saturable absorber can lead to rapid material damage. These shortcomings have motivated our quest for flexible and universally applicable stabilization schemes.

2.5 Active laser stabilization via gain control

Active stabilization of the laser, either by gain or by loss control, aims for suppression of the Q-switching instability without affecting the mode-locking dynamics. Active laser stabilization is possible, since Q-switching instabilities and mode-locked pulse formation occur on vastly different timescales. On a slow timescale corresponding to the kHz to MHz-range the feedback controller interacts with the laser to prevent the occurrence of Q-switching. In contrast, it is inactive at very high frequencies corresponding to the

repetition frequency of the laser and above. In this frequency range the mode-locked pulses are formed by a number of passive mechanisms that the controller should not disturb. To prevent the electronics from affecting the mode-locking mechanism, all active controllers discussed in this Chapter consist of a low-pass filter with a high-frequency roll-off below the laser repetition rate f_R, so that the feedback signal vanishes at this frequency. When a controller bandwidth close to the laser repetition rate f_R is desirable, a low-pass filter with a very steep slope is required to reach the desired attenuation at f_R. For example, in [73] a 4th-order Bessel filter is employed to suppress the control signal at f_R by over 40 dBm.

2.5.1 Noise reduction in cw lasers

The most straightforward stabilization scheme comprises a circuit that monitors the laser output with a photodiode and controls the pump power of the laser. This approach is readily implemented in diode-pumped lasers, since the feedback electronics can directly control the current of the pump diodes and no additional elements have to be added to the laser cavity. In lasers pumped by other solid state lasers, the pump intensity can be controlled with electro-optic modulators, which allow for fast responses with nanosecond delay times.

A first implementation of gain feedback control was shown to suppress the intensity noise in cw solid-state lasers by up to 46 dB [105, 106, 107, 108, 109]. The Er-Yb:glass and Tm-Ho:YAG cw laser systems investigated by Taccheo, Longhi and Svelto showed strong relaxation oscillations in the 100 kHz range that added an excessive amount of relative intensity noise (RIN), not tolerable for the targeted application. A theoretical model of the laser [107] pointed to a complex conjugate pole pair as the origin of the intensity noise spike at 100 kHz. This model also revealed that the influence of perturbations on the pump power of the laser are strongly suppressed at higher frequencies, *i.e.* at the relaxation oscillation frequency, due to a low-pass filter (LPF) at about 1 kHz, established by the Tm-Ho energy transfer process. To suppress the excess noise at the relaxation frequency via feedback on the pump power despite this LPF, a control circuit with high variable gain and with a tunable resonance of high quality factor was built [108, 106]. A fraction

of the output power of the laser was detected with a photodiode, AC-coupled into the active filter to prevent changes in the DC-level of the diode current, and finally coupled into the drive circuit of the pump diode. An exact match of the resonance frequency of the control circuit to the relaxation oscillation frequency of the laser allowed to suppress the excess noise due to relaxation oscillations by up to 46 dB in an Er-Yb:glass laser [105] and by up to 24 dB in an Tm-Ho:YAG laser [108].

While the cw-lasers investigated in this study were not affected by Q-switching instabilities, the work of Taccheo *et al.* points toward the stabilization of SA mode-locked lasers by means of gain feedback: Q-switching instabilities are essentially enhanced relaxation oscillations, and, similar to the cw case, gain feedback stabilization of lasers plagued by Q-switching instabilities is complicated by attenuation due to low-pass filtering that stems from gain relaxation. In the following section we discuss the stabilization of an unstable SA mode-locked laser via gain feedback, derive rules for controller design and discuss the limitations of this approach.

2.5.2 Q-switch suppression in SA mode-locked lasers

Feedback stabilization via gain control, *i.e.* with a controller $G_g(s)$ in the gain relaxation branch of the laser (Fig. 2-6), supports the negative feedback via gain relaxation $A_{12}A_{21}F_2(s)$ by compensating for the destabilizing effect of the low-pass filter $F_2(s)$. The control electronics monitors the laser output proportional to ΔW and controls the small signal gain g_0 via the pump power [65]. In this section, we first derive design rules for corner frequencies and gain of the controller and then discuss the limitations and applicability of this approach to different laser systems. To compensate for the attenuation of the low-pass filter $F_2(s)$ in the gain relaxation branch, the feedback electronics constitutes a proportional-derivative controller (PD-controller, phase-lead-controller, [97])

$$G_g(s) = a_g \frac{1 + s/\omega_{g1}}{1 + s/\omega_{g2}} . \tag{2.29}$$

Between ω_{g1} and ω_{g2}, with $\omega_{g1} < \omega_{g2}$, (Fig. 2-11a) the controller $G_g(s)$ provides derivative gain to compensate for $F_2(s)$. At a significantly higher frequency ω_{g3} the

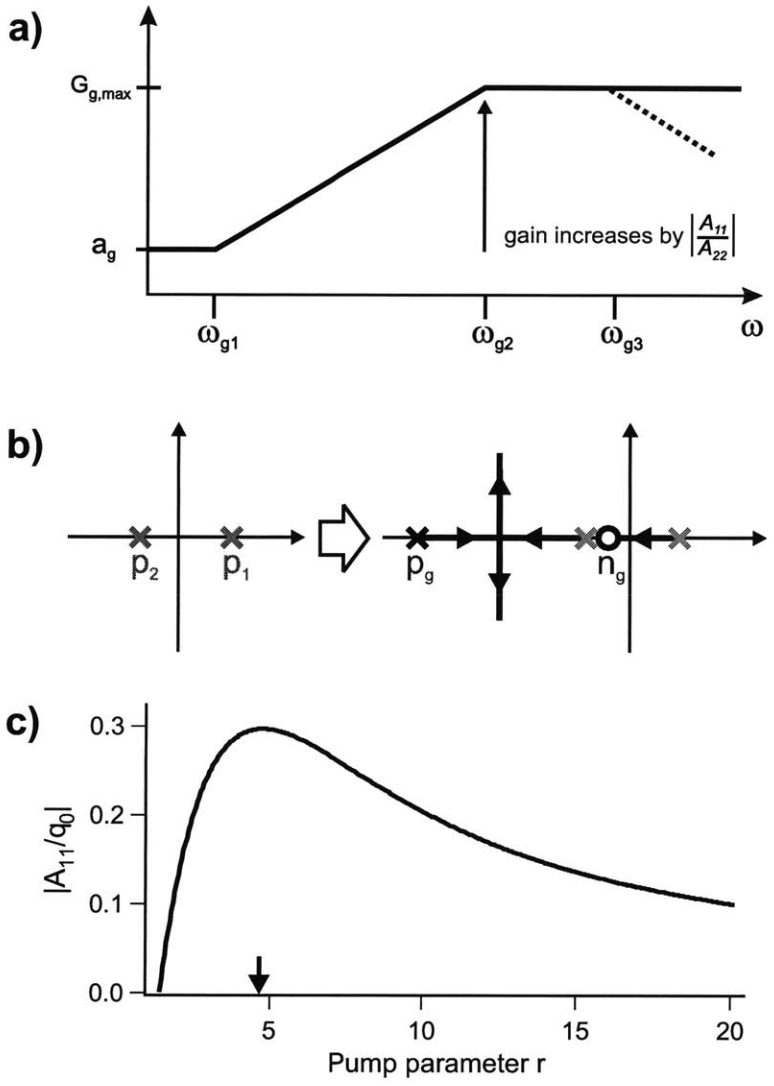

Figure 2-11: **a)** Magnitude response of the gain feedback controller $G_g(s)$. Solid: ideal gain controller. Dashed: Real gain controller with limited bandwidth ω_{g3}. **b)** Root locus plot of the unstable system (left) and of the system stabilized with a gain controller (right) as a function of controller gain a_g. **c)** Parameter A_{11}/q_0 of laser B as a function of pump parameter r.

Table 2.2: Parameters of gain controllers

	laser A	**laser B**
$\omega_{g1}/2\pi$	15 kHz	350 Hz
$\omega_{g2}/2\pi$	24 kHz	480 kHz
ω_{g2}/ω_{g1}	1.6	1340
$(\Delta g_0/g_0)^*_{max}$	0.23%	270%

$^*at\ \Delta W/Ws = 0.01$

controller gain rolls off (dashed line in Fig. 2-11a) to keep the controller from affecting the mode-locking dynamics at the repetition rate f_R. We assume that ω_{g3} is chosen large enough to not affect system stability and therefore ignore it in both (2.29) and in the following discussion. The open-loop transfer function of the laser with gain feedback in Figure 2-6 becomes

$$\begin{aligned} F_B^g(s) &= \frac{1}{sT_R}\Big(-A_{11} + A_{12}(G_g(s) - A_{21})\,F_2(s)\Big) \\ &= \frac{1}{sT_R}\Big(-A_{11} + \frac{A_{12}A_{21}}{A_{22}}\frac{1}{1 - sT_R/A_{22}} \\ &\quad -a_g\,\frac{A_{12}}{A_{22}}\,\frac{1 + s/\omega_{g1}}{1 + s/\omega_{g2}}\,\frac{1}{1 - sT_R/A_{22}}\Big)\ . \end{aligned} \tag{2.30}$$

To obtain a simple and robust controller, the controller parameters are chosen to yield a positive phase margin to $F_B^g(s)$ for all values of s, regardless of the additional contribution from gain feedback via A_{21} (Fig. 2-6). The null $n_g = -\omega_{g1}$ of the gain controller compensates for the roll-off introduced by the low-pass filter $F_2(s)$: $\omega_{g1} \leq A_{22}/T_R$. A large bandwidth $p_g = \omega_{g2} \geq A_{11}/T_R$ of the derivative gain ensures that the controller provides stability for all frequencies at which the saturable absorber destabilizes the system, *i.e.* for $|A_{11}/sT_R| > 1$. Finally, the gain of the controller is chosen to stabilize the system for frequencies between ω_{g1} and ω_{g2}. With the gain $a_g \geq -A_{11}A_{22}/A_{12}$ the controller compensates for the saturable absorber A_{11}, such that the bracket in (2.30) is always positive and the laser remains stable.

This choice of controller parameters leads to the root-locus plot shown in Figure 2-

11b. The null n_g and pole p_g added by the controller introduce a dominant pole. The asymptote of the poles originating in p_2 and p_g is parallel to the imaginary axis. For sufficiently high controller gain a_g the dominant pole is the left half plane, rendering the closed-loop system stable. If an additional corner frequency ω_{g3} would be added to the controller preventing the electronics from affecting the pulse formation at the repetition rate (dashed line in Fig. 2-11a, effect not shown in Fig. 2-11b), the branches of the asymptote would slightly bow to the right. If ω_{g3} is large enough, system stability is not affected.

The challenge of feedback stabilization via gain control lies in the large frequency range, from $\omega_{g1} \approx |A_{22}|/T_R$ to $\omega_{g2} \approx A_{11}/T_R$, over which the controller has to provide derivative gain. In systems with long upper state lifetimes, high repetition rates, and large saturable losses, the corner frequencies of the controller $|A_{22}|/T_R$ and A_{11}/T_R can differ by several orders of magnitude (*e.g.* laser B in Table 2.1 and 2.2). Consequently, the controller gain $|G_g(s)|$ rises from its minimum value a_g to a maximum gain value at ω_{g2} that is $|A_{11}/A_{22}|$ times as large (Fig. 2-11a):

$$|G_{g,max}| \geq A_{11}^2/A_{12} \quad . \tag{2.31}$$

At high frequencies, the absolute controller gain can become so large that it leads to saturation of the output for small fluctuations at the controller input. To provide an estimate of this effect, we calculate how the the small signal gain g_0, the physical variable controlled by the feedback electronics, responds to input fluctuations $\widetilde{\Delta W}/W_s$. With eq. (2.13), eq. (2.31) and $g_0 = r\, g_s$ the relative change of the control variable becomes:

$$\frac{\widetilde{\Delta g_0}}{g_0} = \frac{\tau_L\, A_{11}^2}{r T_R\, g_s}\, \frac{\widetilde{\Delta W}}{W_s} \quad . \tag{2.32}$$

In lasers with large τ_L and small T_R, pulse energy variations $\Delta W/W_s$ on the order of a few percent can already saturate the controller output. For example, the controller output of laser B can be completely saturated by a relative input variation $\widetilde{\Delta W}/W_s$ of as little as 7%, if the controller parameters are calculated at the laser operating point listed in Table 2.1

($r = 20$). During saturation, the controller varies the small signal gain $\Delta g_0/g_0$ by as much as 100%, *i.e.* it even completely turns off the pump power for stabilization. However, it is unable to respond to input variations exceeding 7%. This example illustrates that in lasers with a large ratio $q_0\tau_L/T_R$ the gain feedback stabilization cannot force the laser from Q-switched mode-locking to pure cw-mode-locking. In the presence of Q-switching, the input variable changes by several hundred percent, far beyond the output range available to the controller. The controller cannot respond over the full range of a Q-switch cycle and is unable to stop the Q-switching.

A possible solution to the limited dynamic range of the control variable was presented in [86]: The gain controller is active while the pump power is adiabatically increased from threshold to the operating point, keeping the laser stable over the entire pump parameter range and preventing the evolution of Q-switching right from the beginning. However, now the controller parameters a_g, ω_{g1} and ω_{g2} have to meet the design criteria mentioned above, not only in the steady-state operating point of the laser, but over the entire pump parameter range. An even larger maximum controller gain $|G_g(\omega_{g2})|$ may be needed, since the parameter A_{11} changes nonlinearly with the pump parameter r, as illustrated for laser B in Figure 2-11c. While the strong saturation of the absorber $W_s/E_A = 10$ results in a moderate value of A_{11} at the maximum pump parameter r, A_{11} peaks for $r_{\text{peak}} = 4.5$. At this point, where $A_{11,max} = 0.3\,q_0$, the maximum relative change of the control variable g_0 becomes

$$\left(\frac{\Delta g_0}{g_0}\right)_{max} = \frac{0.09\,\tau_L\,q_0^2}{r_{\text{peak}}\,T_R\,g_s}\,\frac{\Delta W}{W_s} \quad . \tag{2.33}$$

Feedback stabilization via gain control is only possible if $\Delta g_0/g_0$ does not exceed reasonable values for the expected pulse energy fluctuations during adiabatic power ramp-up of the laser.

The feasibility and limitations of laser stabilization via gain control may be illustrated by two examples. In [65] the stabilization of a 100 MHz Nd:YVO_4 laser was demonstrated. Equation (2.33) based on the parameters of laser A shows that this system can be very well stabilized via gain feedback, even at $r_{\text{peak}} = 9.6$ (Figure 2-7). The above-mentioned choice of controller parameters leads to no more than 23% variation of controller output

$\Delta g_0/g_0$ for a 100% variation in ΔW in this point. Thus, by adiabatically ramping up the pump power of the laser, stability can be maintained over the entire pump parameter range. The reason is that the unstabilized system is rather close to stable operation: Even at $r = r_{\text{peak}}$, when the destabilizin effect of the absorber is strongest, the corner frequencies ω_{g1} and ω_{g2} differ by less than a factor of three (Table 2.2).

In contrast, the long upper state lifetime and short cavity round trip time of laser B render stabilization very difficult. For stabilization over the entire parameter range, the controller has to provide derivative gain over three orders of magnitude (Table 2.2) to allow for stabilization even at $r_{\text{peak}} = 4.5$. At this pump parameter an input variation of as little as 1% would require a change in control variable of 270%, completely saturating the controller output, according to eq. (2.33). Therefore, gain feedback stabilization of this laser is extremely difficult.

In summary, gain feedback control is a highly effective and straightforward method of laser stabilization, when (i) the pump power of the laser is well controllable and (ii) when the dynamic range eq. (2.33) needed for stabilization is not too large. Gain feedback control is especially suitable for systems with moderate values of q_0 and τ_L/T_R, *i.e.* systems that are not too far from stable operation. In contrast, systems with large q_0, τ_L and f_R that require a very large dynamic range eq. (2.33) can hardly be stabilized via gain feedback control. Stabilization via intracavity loss modulation (see next section) is more appropriate in this case.

2.6 Active laser stabilization via intracavity loss control

Stabilization via control of intracavity losses is a universal approach to laser stabilization, applicable even to lasers with large saturable loss and at highest repetition rates. The loss controller $G_l(s)$ provides feedback in parallel to the saturable absorber A_{11} (Fig. 2-6). It interacts with the laser by means of an intracavity loss modulator. By direct compensation of the instability, loss control stabilization circumvents the problem of low-pass filtering

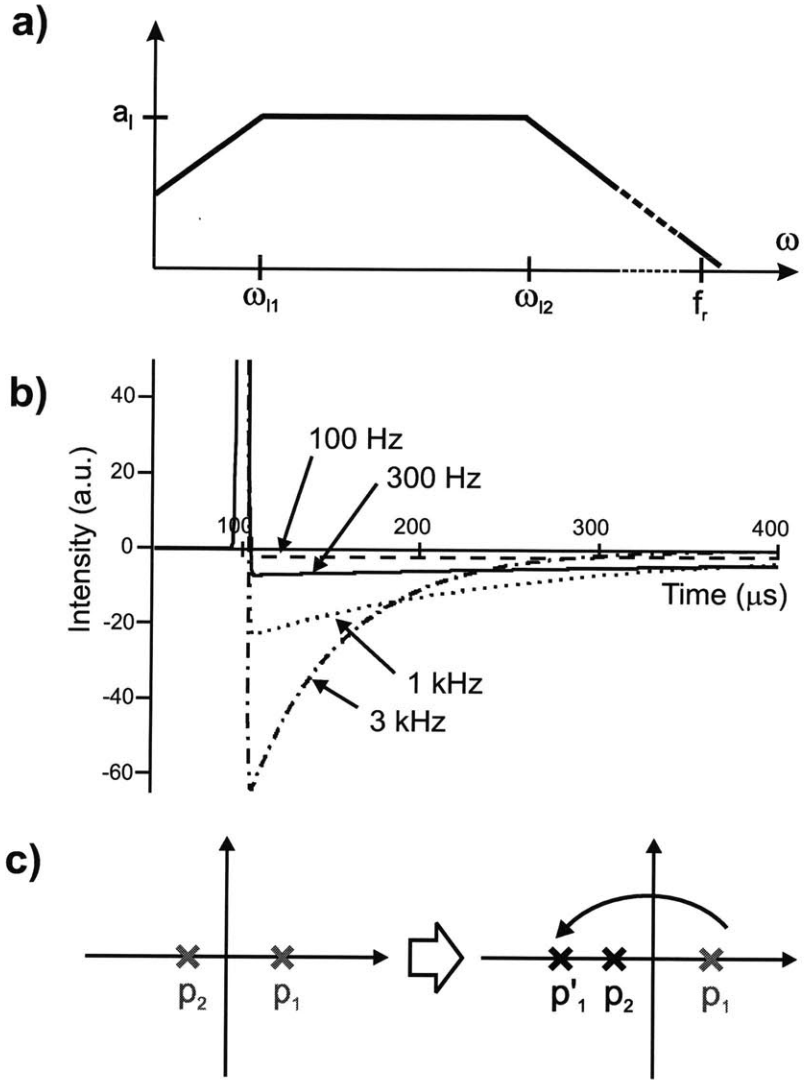

Figure 2-12: **a)** Magnitude response of the loss feedback controller $G_l(s)$. **b)** Impulse response of the loss controller to a Q-switch cycle of $3\mu s$ duration for different corner frequencies $\omega_{l1} = 2\pi f_{l1}$ of the differentiator $1/(1+\omega_{l1}/s)$. **c)** Principle of laser stabilization via loss control. The pole $p_1 = A_{11}/T_R$ is shifted to the left half plane by the controller.

that limits the applicability of gain feedback control (section 2.5). As a response to a rising pulse energy ΔW, the controller increases the intracavity loss, directly compensating for the bleaching of the saturable absorber. We implement the controller as a bandpass filter with proportional gain at medium frequencies around the Q-switch repetition rate (Fig. 2-12a):

$$G_l(s) = a_l \frac{1}{(1+\omega_{l1}/s)(1+s/\omega_{l2})} \quad . \tag{2.34}$$

Low-pass filtering at high frequencies limits the controller bandwidth to $\omega_{l2} \ll f_r$ (Fig. 2-12a), in order to preclude the active stabilization from interacting with individual pulses at the laser repetition rate. If the desired controller bandwidth is much smaller than the repetition rate, first order low-pass filters similar to the one in eq. (2.34) provide sufficient damping of the carrier signal, otherwise higher-order filters with a steeper slope can be employed [73]. In contrast, at frequencies below ω_{l1}, the controller gain is rolled off by AC coupling the input signal (Fig. 2-12a) to prevent the controller from changing the steady-state intracavity loss with its loss modulator. This AC coupling corresponds to a differentiation of the input signal. The corner frequency of the differentiator ω_{l1} must be chosen carefully if the loss controller is supposed to handle the transition of the laser from Q-switching to stable cw mode-locking. For large values ω_{l1}, the response of the controller to a typical Q-switch cycle of 3 μs duration changes the intracavity loss balance for several hundred microseconds (Fig. 2-12b), preventing stabilization of the system. This detrimental effect can be avoided with a sufficiently small value $\omega_{l1} \approx 2\pi \cdot 100$ Hz, allowing the controller to return to its original state after passage of the Q-switch cycle.

In the overall laser system, the intracavity loss controller acts as a cascaded subsystem (Figure 2-6), resulting in the open-loop system transfer function

$$F_B^l(s) = \frac{1}{sT_R}\Big(-A_{11} + \frac{a_l}{1+\omega_{l1}/s}\,\frac{1}{1+s/\omega_{l2}} + A_{12}A_{21}F_2(s)\Big) . \tag{2.35}$$

The negative feedback via $G_l(s)$ stabilizes the laser against Q-switching instabilities by shifting the unstable pole $p_1 = A_{11}/T_r$ from the right to the left of the complex plane (Fig. 2-12c). With controller gain $a_l > A_{11}$ the controller ensures system stability independent of the stabilizing gain relaxation $A_{12}A_{21}F_2(s)$. To satisfy the Nyquist criterion [97], [98]

the controller bandwidth ω_{l2} must exceed the frequency where the positive feedback of the SA reaches unity gain:

$$\omega_{l2} > A_{11}/T_R \, . \tag{2.36}$$

This condition, valid for lasers deep in the unstable regime, states that the required controller bandwidth depend linearly on the round-trip time. The linear relation can be understood intuitively from the following consideration: The frequency of Q-switching and relaxations oscillations is readily obtained from Equation 2.7 as

$$\omega_{QS} = \frac{1}{2T_R}\sqrt{-4A_{12}A_{21} - (A_{11} - A_{22})^2} \, . \tag{2.37}$$

In the absence of a saturable absorber (*i.e.* when A_{11}=0) this expression can be simplified to yield the relaxation oscillation frequency

$$\omega_{rel} = \frac{1}{2T_R}\sqrt{-4A_{12}A_{21} - A_{22}^2} = \sqrt{\frac{2l(r-1)}{\tau_L T_R} - \left(\frac{r}{2\tau_L}\right)^2} \approx \sqrt{\frac{2l(r-1)}{\tau_L T_R}} \, . \tag{2.38}$$

The relaxation oscillation frequency scales with the square root of the repetition rate, assuming an upper state lifetime much longer than the cavity round trip time. However, when the laser becomes unstable due to the addition of a saturable absorber in the cavity, and when the laser Q-switches, according to Eq. (2.27) $A_{11} > |A_{22}|$ such that the Q-switching repetition rate can be calculated from Eq. (2.37) as

$$\omega_{QS} = \frac{1}{2T_R}\sqrt{-4A_{12}A_{21} - A_{11}^2} = \sqrt{\frac{2l(r-1)}{\tau_L T_R} - \left(\frac{A_{11}}{2T_R}\right)^2} \, . \tag{2.39}$$

If the laser is only slightly unstable, the Q-switching instability can be understood as an enhancement of the relaxation oscillations. In this regime, the instability changes the relaxation oscillation frequency only by a small amount and the Q-switching oscillation frequency ω_{QS} shows a square root dependence on the round trip time. In contrast, for systems deep in the unstable regime, such as in the high repetition rate laser C of Table 2.1, the Q-switching oscillation frequency increases linearly with repetition rate, since in this regime the first term of Eq. (2.39) can be neglected. It is apparent that the controller

bandwidth must exceed the Q-switching frequency in order to suppress this instability. This consideration explains the linear dependence of controller bandwidth on the round trip time in Eq. (2.36), that makes it difficult to stabilize lasers at GHz repetition rates. The large required controller bandwidth ω_{l2}, leads to high demands on the permitted time lag in the controller. For example, for stabilization of laser C in Table 2.1 over the entire pump parameter range, a controller gain of $a_l \geq A_{11,max} = 0.3\,q_0$ and a controller bandwidth of $\omega_{l2} = 2\pi{\cdot}10$ MHz are required. To ensure a sufficiently small controller phase lag $\varphi_l \leq \pi/4$ at the corner frequency $\omega_{l2} = 0.3\,q_0/T_R$, the propagation delay T_l in the controller must satisfy $T_l \leq \pi/(4\,\omega_{l2}) = 13$ ns. To build a feedback controller with a delay below this value, all system variables, such as the travel time of the light, the response of photodetector and modulator, and the circuit propagation delay have to be optimized. In Appendix A we present the circuit components for the required wide-band control electronics and thus show that the feedback stabilization of even lasers at multi-GHz repetition rates is feasible. However, while the controller bandwidth scales linearly with the laser repetition rate in highly unstable systems, our example of a 40 GHz mode-locked laser shows that even for the highest repetition rate systems interesting in the applications we are considering in this thesis, a modest controller bandwidth on the order of several tens of megahertz is sufficient for stabilization — a value still three decades below the actual laser repetition rate.

While loss control might demand a relatively large controller bandwidth in lasers at high repetition rates, it poses only a modest demand to the modulation depth of the controller. In fact, the modulation depth must just be large enough to compensate for the maximum saturable loss in the saturable absorber. With the controller gain $a_l = A_{11,max} = 0.3\,q_0$ and with eq. (2.12) the controller responds to a 100% input variation $\Delta W/W_s$ in laser C of Table 2.1 with a loss modulation as small as $\Delta l = 1.5 \times 10^{-3}$. Thus, as long as the laser is kept in stable operation during the ramp-up from threshold and operating point, and as long as the evolution of Q-switch oscillations is prevented from the beginning, a relatively small modulation depth is sufficient for maintaining laser stability. In summary, the simplicity of feedback stabilization via loss control, combined with modest requirements on modulation depth and bandwidth, render this approach

attractive for application in lasers at high repetition rates.

2.7 Passive laser stabilization via inverse saturable absorption

In addition to laser stabilization via *active* feedback control, the *passive* stabilization by means of inverse saturable absorption has been investigated theoretically end experimentally as well [77, 79, 81, 80, 78, 82, 83]. Similar to the passive stabilization by strong saturation of the SA (section 2.4.4 and Fig. 2-10), the addition of an inverse saturable absorber aims at a flat saturation slope $\partial q/\partial W$ in the operating point of the laser in order to reduce the destabilizing effect of the absorber. As shown in Fig. 2-13 the addition of an inverse saturable absorber leads to a maximum of the saturation curve with a flat slope, compared to the SA without an inverse contribution. The slop reduction allows to meet the stability condition against Q-switching [eq. 2.28] or, thinking in the control systems context, to reduce the destabilizing matrix element A_{11} (Fig. 2-6).

Alternatively, the contribution of inverse saturable absorption can be considered as separate negative feedback (Fig. 2-13). In the following, we summarize this viewpoint briefly to complete our analysis of laser stabilization and to contrast active and passive stabilization techniques. In the presence of both saturable loss $q_A(W)$ and inverse saturable loss $q_I(W)$, the total intensity-dependent loss becomes

$$q_{tot}(W) = q_A(W) + q_I(W) \quad . \tag{2.40}$$

The inverse saturable absorption (ISA) reduces the intensity dependent reflectivity $R_{tot}(W) = R_{ns} - q_A(W) - q_I(W)$ of the saturable Bragg reflector (Fig. 2-13a). For short pulse widths in the 100-fs range, ISA is predominantly caused by two-photon absorption (TPA), scaling with peak intensity and therefore with pulse width. In contrast, for longer pulses with a duration well above 1-ps, inverse saturable absorption is primarily caused by direct free carrier absorption (FCA) and by FCA which is triggered by TPA-induced carriers in the saturable Bragg reflector [80, 78]. While TPA and direct-FCA both scale linearly with

pulse energy, the TPA-induced FCA shows a quadratic dependence. Motivated by the need for sub-1-ps pulses in the targeted applications of high repetition rate laser technology, we limit the following discussion to the case of TPA induced by sub-1-ps pulses. However, similar to [78] the calculation can readily be extended to include FCA as well.

The linear dependence of the inverse saturable loss on pulse energy is given by [78, 83]:

$$q_I(W) = \frac{W}{F_I\, A_{eff,A}} \quad . \tag{2.41}$$

It is characterized by the inverse saturation fluence $F_I \approx \tau_P/(z_{eff}\,\beta_{TPA})$, that depends on the pulse width τ_P, the two-photon absorption coefficient β_{TPA} of the spacer layer in the absorber [78], and the effective layer thickness z_{eff}, determined by geometrical thickness and standing-wave effects. The nonlinear reflectivity of the absorber increases monotonically with fluence, under the influence of saturable loss $q_A(W)$, while the inverse saturable loss reduces the reflectivity for high fluence values, resulting in a roll-off in the reflectance curve. Both effects are illustrated in Figure 2-13a for a saturable absorber with an ideal reflectance $R_{ns} = 100\%$, a modulation depth $q_0 = 1.5\%$, and typical fluence values of $F_A = 30\mu J/cm^2$ and $F_I = 30mJ/cm^2$ [83].

In section 2.4 we discussed the destabilizing effect of positive feedback via A_{11}^A, established by the saturable loss $q_A(W)$. In contrast, by reducing the reflectivity for very high fluence values, the inverse saturable loss constitutes instantaneous negative feedback to the integrator $1/sT_R$ (Fig. 2-13c). Its impact on system stability is evaluated by calculating the two components of the overall feedback term $A_{11} = A_{11}^A + A_{11}^I$:

$$A_{11}^A = -2\frac{\partial q_A}{\partial W}\bigg|_{W_s} \quad W_s > 0 \tag{2.42}$$

$$A_{11}^I = -2\frac{\partial q_I}{\partial W}\bigg|_{W_s} \quad W_s = -\frac{2\,W_s}{F_2 A_{eff,A}} < 0 \ . \tag{2.43}$$

Fig. 2-13b depicts the individual terms of the expanded stability condition eq. (2.27); $A_{11,tot} = A_{11}^A + A_{11}^I < |A_{22}|$ for laser A with a stronger saturable loss of $q_0 = 1.5\%$. Without additional ISA, the strong saturable loss keeps the system unstable for all values

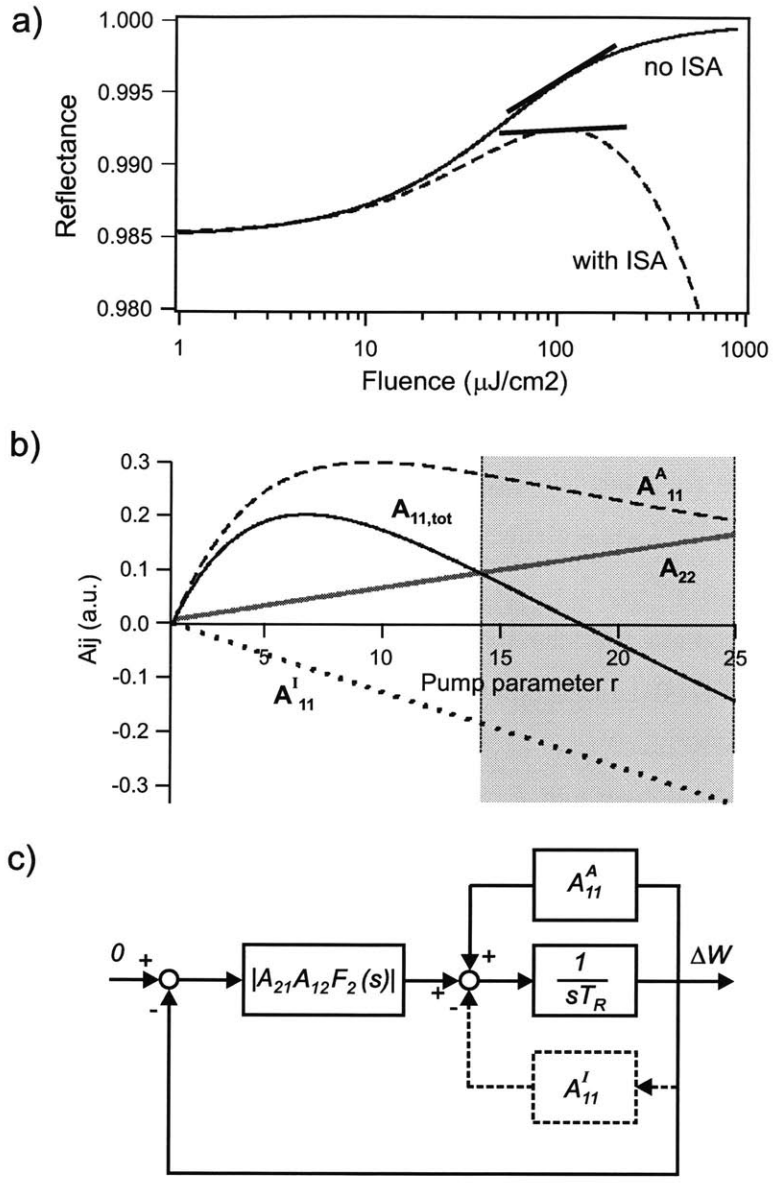

Figure 2-13: **a)** Intensity-dependent reflectance of a saturable Bragg reflector with $q_0 = 1.5\%$ saturable loss (solid line) and inverse saturable loss as describe in the text (dashed line). **b)** Terms of the stability condition for laser A. Stability is achieved for $r > 16$, when $A_{11,tot} < |A_{22}|$. For $r > 18.4$ the pulse breaks up into multiple pulses, such that stable single-pulse operation can only be achieved in the gray shaded range. **c)** Block diagram of the laser stabilized via inverse saturable absorption. ISA constitutes instantaneous negative feedback via A_{11}^I.

of r, since $A_{11}^A > |A_{22}|$ (compare Fig. 2-7a, where $q_0 = 0.5\%$). However, the monotonic reduction of $A_{11,tot}$ due to the negative contribution of inverse saturable loss A_{11}^I renders the system eventually stable for $r > 14$.

From a control systems viewpoint, A_{11}^I provides instantaneous negative feedback to the integrator, counteracts $q_A(W)$, and thus contributes to system stability (Fig. 2-13c). In fact, by reducing the overall value $A_{11,tot}$, the ISA shifts the destabilizing pole $p_1 = A_{11,tot}/T_R$ towards the left half-plane, similar to the stabilization via loss control (Fig. 2-12c). Depending on its strength, inverse saturable absorption may be employed to either fully stabilize the laser, *e.g.* in Fig. 2-13b for $r > 14$, or to merely bring the system closer to stability, facilitating active feedback stabilization via gain or loss control.

The advantages of using inverse saturable absorption for passive laser stabilization are, that no additional feedback electronics are needed and that the dual functionality of pulse formation and system stabilization is integrated in a single optical component. However, stabilization is only achieved at the expense of a narrow operating window between stability and breakup into multiple pulses [78]. At fluence values beyond the rolloff in reflectivity the laser pulse splits into two pulses, each with a lower pulse energy. The breakup into multiple pulses occurs, when each of the pulses with half the pulse energy experiences a lower loss than a single pulse in the cavity [75]. In our example, this point is reached at a fluence of $150\mu J/cm^2$, corresponding to a pump parameter of $r = 25$ (Fig. 2-13b). Consequently, only a narrow operating window of $14 < r < 25$ remains for stable single-pulse operation. Typically the desired operating regime, limited by Q-switching instabilities on the one side and multiple-pulse-breakup on the other, requires to meet the target fluence on the saturable absorber within a factor of two, similar to our example. While such a small parameter range is already difficult to find in a laboratory experiment, it might constitute severe obstacles to a manufacturing process that requires large tolerances. In contrast, the active stabilization schemes discussed in sections 2.5 and 2.6 are designed to operate over the full pump parameter range, providing a robust approach to laser stabilization. Active stabilization also decouples stability issues from pulse shaping dynamics, allowing for operation of the laser under optimum pulse forming conditions.

2.8 Conclusion

In summary, in this Chapter we have introduced a control systems representation of the laser mode-locked by a saturable absorber and identified a low-pass filter describing gain relaxation as the source of Q-switching instabilities. Gain and loss controllers can be employed for active laser stabilization, the former compensating for this low-pass filter, the latter directly counteracting the destabilizing effect of the saturable absorber. Design guidelines for controller structure, loop gain and loop bandwidth have been derived, that help to choose an optimum controller for a given laser system. Gain controllers are mostly applicable for lasers rather close to the stability limit, *i.e.* for moderate values of q_0 and τ_L/T_R. At higher repetition rates their applicability is limited by the growing demand for dynamic range. In contrast, loss controllers allow for laser stabilization with only a small modulation depth, in systems with large saturable loss and up to highest repetition rates. Both approaches to active laser stabilization decouple the stability of the laser from the pulse shaping dynamics, allowing for robust laser systems stable over the entire pump parameter range, while the passive stabilization via inverse saturable absorption requires operation within a narrow parameter window.

Chapter 3

Suppression of Q-switching instabilities with a slow intracavity loss modulator (AOM)

In the previous Chapter we have outlined the benefits of active laser stabilization and identified feedback control with an intracavity loss modulator as a universally applicable control scheme (sections 2.6 and 2.5): Electronic feedback control relieves the saturable absorber (SA) from providing *both* pulse shaping *and* stabilization, allowing for a choice of absorber parameters that fully optimize the pulse shaping dynamics [99, 100]. In particular, a larger amount of saturable loss q_0 can be tolerated, permitting for shorter pulses, and strong saturation of the absorber (section 2.4.4) leading to premature device damage, can be avoided. To date, active feedback stabilization of SA mode-locked lasers has been demonstrated experimentally only by gain control with a derivative controller acting on the pump power of the laser (section 2.5) [65, 110]. This technique reaches its limit in high-repetition rate lasers based on certain gain media such as Er-Yb:glass with long upper state lifetimes (section 2.5 and [86]), since the gain medium acting as a low-pass filter strongly dampens all fast modulations. The relaxation oscillation frequency, at which the controller acts, lies up to three orders of magnitude above this cutoff frequency in Er- and Yb-doped laser systems, that are the most attractive for fabrication of GHz-repetition rate mode-locked microchip and waveguide lasers due to the feasibility of diode-pumping.

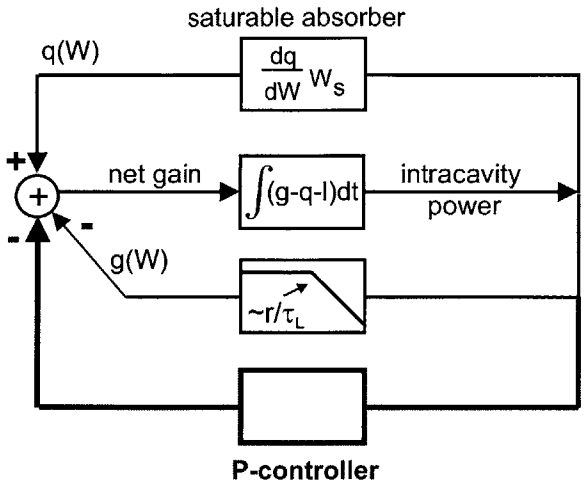

Figure 3-1: Block diagram of the control system with active feedback stabilization via loss control.

For example, in the low repetition rate Er-doped waveguide laser discussed in this Chapter, the corner frequency of the low-pass filter, determined by the inverse stimulated lifetime of the gain medium, was about 1 kHz, whereas Q-switch repetition rates of 25 kHz...50 kHz were observed. The microchip and waveguide lasers anticipated in section 1.4.1 would be built at a 1000 times higher repetition rate, where Q-switching instabilities are observed in the MHz frequency range [71], widening the gap between corner frequency of the low-pass and the Q-switch oscillation by another 1.5 orders of magnitude. These examples illustrate, that feedback signals applied to the pump power would be damped by over 30 dB in the targeted high repetition rate laser systems, severely limiting the applicability of gain feedback control (section 2.5).

In this Chapter, we demonstrate suppression of Q-switching in a continuous-wave mode-locked (cw-ML) laser with an intracavity loss modulator. An automatic gain control accomplishes stability over the entire parameter range of the laser. As discussed in section 2.6, the control of intracavity losses avoids undesired low-pass filtering of the feedback signal inherent in gain-feedback stabilization schemes, since it *directly* compensates for the saturable loss causing the instability (Fig. 3-1). Consequently, it extends the well-known active stabilization schemes [111, 85, 65, 110] to lasers with a long upper state lifetime, a

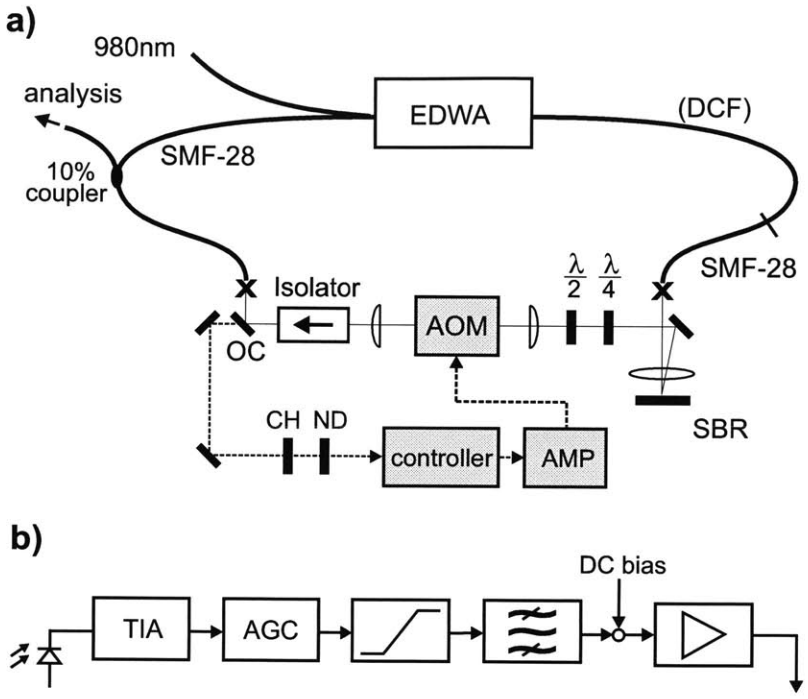

Figure 3-2: **a)** Experimental setup. Abbreviations: EDWA Er-doped waveguide amplifier, DCF dispersion compensated fiber, SMF single mode fiber, SBR saturable Bragg reflector, TLS tunable laser source, OC output coupler, CH optical chopper, ND neutral density filter, AMP driver and amplifier, AOM acousto-optic modulator. **b)** Block diagram of control circuit. Abbreviations: TIA transimpedance amplifier, AGC automatic gain control.

large amount of saturable loss and the highest repetition rates. The primary advantage of this scheme is that it allows stability of mode-locking independent of the characteristics of the gain medium and of specific combinations of pump power, pulse energy and saturable absorption.

3.1 Experimental setup

To test the proposed gain feedback scheme experimentally, we built a fiber laser with an Er-doped waveguide amplifier (EDWA) as the gain medium [112]. We are thankful to Professor Frank Wise of Cornell university, who made the EDWA available to us. Our choice of the gain medium has been motivated by the uncommonly long upper state

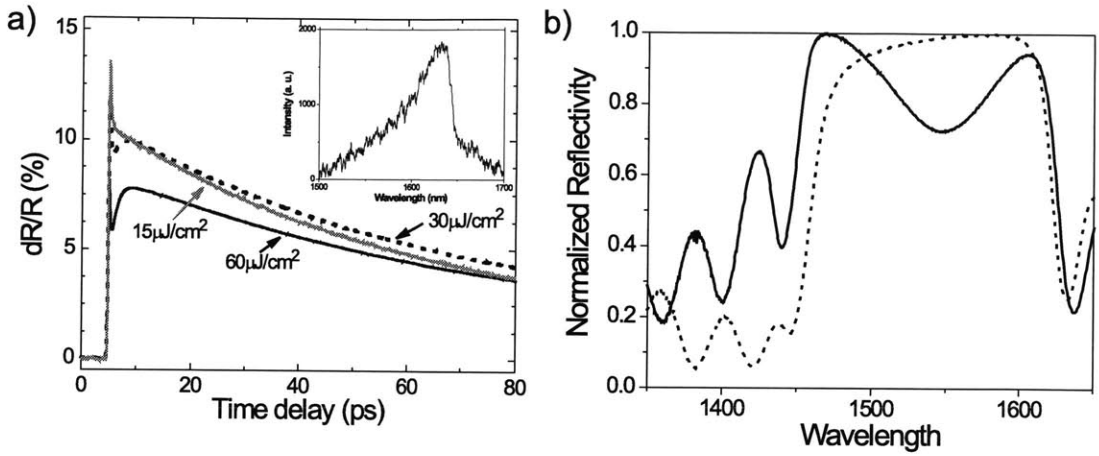

Figure 3-3: Characteristics of the saturable Bragg reflector (sample R921). **a)** Pump-probe traces taken at 1530 nm and (inset) photoluminescence measurement of the device. **b)** Reflectance of the uncoated SBR (dashed) and SBR with a resonant coating (solid). Data courtesy of Juliet Gopinath.

lifetime of the Er-doped glass (7.9 ms), the ease of experimentation in the diode-pumped fiber-coupled laser system and the similarity of the gain medium to that targeted for high repetition rate lasers at communications wavelengths. The laser cavity, illustrated in Fig. 3-2, comprises the Er-doped waveguide amplifier (EDWA), which is pumped by a 980 nm laser diode with up to 300 mW pump power. The EDWA is fiber-coupled and co-packaged with the WDM coupler providing the pump power. The lead fibers of the EDWA and the 10% output coupler of the cavity are SMF-28, with a total length of 5.4 m. A 0.9 m-long segment of dispersion-compensating fiber (DCF, +90,000 fs^2) keeps the net cavity dispersion close to zero (-20,000 fs^2) to permit short and energetic pulses [112].

The laser is mode-locked with saturable Bragg reflector (SBR), which was grown in Professor Kolodziejski's group at MIT. It is composed of 12 $In_{0.5}Ga_{0.5}As/InP$ quantum wells, the material composition leading to a band edge at about 1640 nm (Fig. 5-5a, inset). The wells are embedded in a full wavelength InP layer. They are split into two groups, each located in a different peak of the standing wave pattern of the electromagnetic field [113]. Each well was designed to be 10 nm wide with a 7 nm wide InP barrier between wells. The quantum well structure is deposited on a 22-pair GaAs/AlAs Bragg mirror, centered at 1540 nm. The SBR was coated with a resonant coating by Peter O'Brien at

Lincoln Lab, comprising a half-wave low-index layer and one quarter-wave SiO_2 / Si layer pair [1]. Figure 5-5b shows the reflectance of both the uncoated device, characterized by a modest absorption, and the absorber with a resonant coating, with over 20% loss at 1540 nm. Pump-probe measurements (Fig. 5-5a) carried out in Professor Ippen's group by Juliet Gopinath determine the saturable loss to reach up to 13.5% at 1540 nm, with a relatively slow recovery time of 43 ps. The laser mode is focused with an f=8 mm achromatic lens (Thorlabs C240TM-C) onto a 13 μm spot on the SBR. A pick-up mirror deflects the beam reflected from the SBR and sends it through the remaining part of the free-space section of the laser cavity. A half-wave and a quarter-wave plate are placed to convert the polarization of the light rotated in the fiber section to p-polarization, in alignment with the isolator and the acousto-optic modulator (AOM), that serves as an intracavity loss modulator. The isolator provides for unidirectional propagation. Linearly polarized light is coupled back into the fiber to avoid accidental amplitude modulation due to nonlinear polarization rotation. A dielectric 5% output coupler (OC) provides the feedback control electronics with output power, while a 10% fiber coupler supplies light to the analysis equipment, optical spectrum analyzer, RF analyzer and the autocorrelator, whose input is amplified to a constant power level of about 10 mW with a home-built Erbium-doped fiber amplifier (EDFA) [2]. The corresponding repetition rate of the laser cavity is 29 MHz. Higher repetition rates of 39 MHz and 101 MHz were also studied and will be discussed below.

The feedback control circuit constitutes a proportional controller (P-controller) rather than the derivative controller used in previous work [111, 85, 65, 110]. The electronics consists of a photodiode with a 70 MHz transimpedance amplifier (TIA), a limiting amplifier, an automatic gain control circuit (AGC), a bandpass filter and a gain stage with adjustable DC-bias. It is discussed in full detail in appendix A. The use of an AGC is motivated by the observation, that the output power feeding the control circuit is pro-

[1]The exact SBR structure is: Bragg mirror - 74 nm InP - 6x (10 nm $In_{0.5}Ga_{0.5}As$, 7 nm InP) - 147 nm InP - 6x (10 nm $In_{0.5}Ga_{0.5}As$, 7 nm InP) - 74 nm InP - 577 nm SiO_2 - 119 nm Si - 288 nm SiO_2. source: [113]

[2]To block residual 980 nm pump light at the output of the EDFA, a fiber-coupled isolator was added between EDFA and autocorrelator. This way, cw-saturation of the photomultiplier tube could be prevented.

portional to the intracavity power, *i.e.* it rises from zero to its maximum value as the laser is pumped from threshold to its operating point. As a result, the magnitude of the stabilizing feedback, the term $G_l(s)$ in Fig. 2-6, grows as the pump power increases. However, to compensate for the destabilizing effect of the saturable absorber, the matrix element A_{11} in Fig. 2-6a, a highly nonlinear gain as a function of pump parameter r, would be needed. Without AGC the feedback gain increases linearly with pump power, similarly to the matrix element A_{22} in Fig. 2-7a. It leaves either a region of instability due to insufficient negative feedback (like the value of A_{22} depicted) for small r, or it runs the danger of oscillations in the feedback loop for high feedback gain at large values of r, since the feedback controller operates on a very small phase margin, as discussed below. Ideally, the feedback gain follows the magnitude of destabilizing feedback A_{11} of the saturable absorber as the pump power is increased to stabilize the laser over the entire parameter range. In a rough first-order approximation of this characteristic the AGC implemented in this experiment provides an almost constant value of negative feedback as r increases. It is implemented as a resistive voltage divider with a 100 Ω resistor and a field effect transistor (2N7000) used as a variable resistor. The AGC does not effect the phase characteristics of the overall feedback controller, since the excess phase stays below 5 deg for frequencies smaller than 3 MHz (for circuit details see appendix A). The fact that a constant value of feedback gain, instead of a gain varying proportional to $A_{11}(r)$, is able to stabilize the laser over its entire parameter range is attributed to significant hysteresis effects, especially in the regime of very low intracavity power, where Q-switching seems to be easier to prevent.

The controller incorporates a bandpass filter blocking both DC signals and higher frequencies in order to preserve this operating point regardless of either pump power or the mode-locking state (QSML vs. cw-ML) and to prevent the circuit from interfering with the individual pulses at the repetition rate. The output of the transimpedance amplifier is AC-coupled to the next stage of the circuit. The corner frequency of $\omega_{l1} \approx 2\pi \cdot 300Hz$ was selected to facilitate the transition from Q-switched mode-locking to stable cw-operation, as discussed in detail in section 2.6 and illustrated in Fig. 2-12b. At higher frequencies, a steep roll-off at 6 MHz is implemented by a 4th order Bessel filter that suppresses

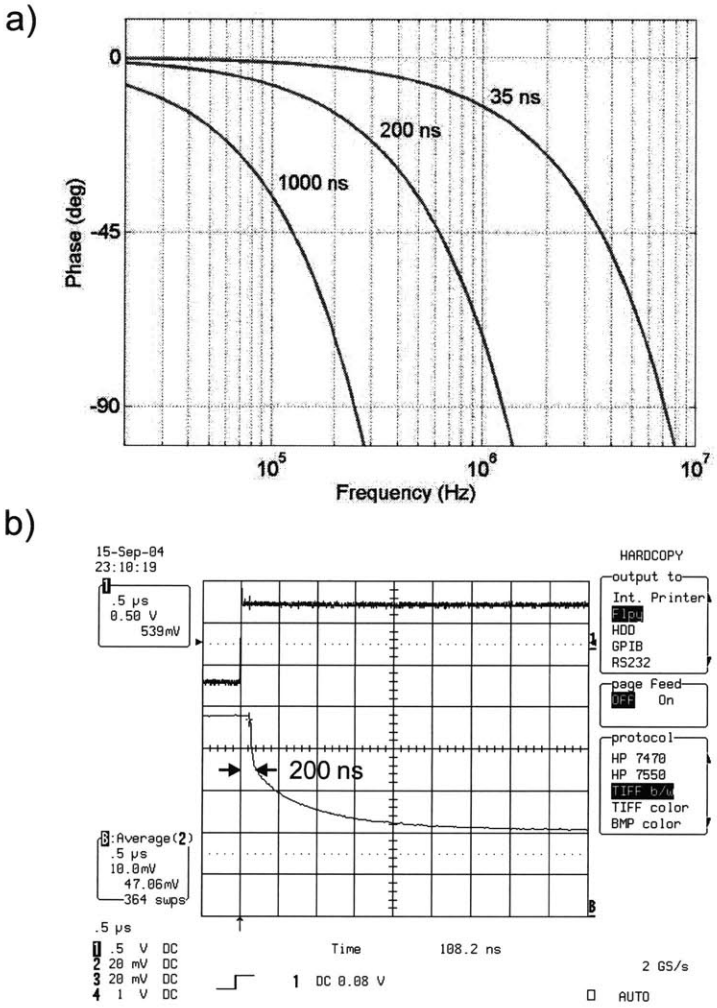

Figure 3-4: **a)** Phase lag introduced by the AOM as a function of frequency for different values of propagation delay T_{AOM} . **b)** Oscilloscope recoding of AOM drive signal (upper trace) and modulation response (lower trace).

the repetition rate and its harmonics by at least 40 dB while allowing for maximum controller bandwidth. The gain of the P-controller is adjusted with a variable neutral density filter (ND) in the beam incident on the photodiode, while a fast limiting amplifier avoids oversaturation and subsequent slow recovery from a Q-switch cycle by keeping the output signal of the controller within the limits of the AOM driver.

The signal of the controller feeds a commercial AOM-driver, whose output is amplified by an RF-amplifier (AMP) to achieve a maximum modulation depth of 45%. Since the diffraction efficiency of the $PbMoO_4$ (lead molybdate) AOM (Isomet model 1205C-1) is decreases by 50% from 800 nm to 1500 nm, a high drive power of about 10 W is applied to the AOM to reach the desired modulation depth. The AOM, specified for only up to 2 W of RF power, is water-cooled and was eventually destroyed in an attempt to reach even higher suppression of the relaxation oscillations. The loss introduced by the AOM is proportional to the cosine squared of the applied drive voltage. To reduce this nonlinearity, the AOM is slightly biased and permanently introduces a small amount of loss, such that it can both increase and decrease intracavity losses. To increase the diffraction efficiency, the laser mode is focused to a 40 μm spot inside the AOM by two 50 mm achromats, separated by two focal lengths. The key challenge of using the AOM as an intracavity loss modulator is the propagation delay T_{AOM} of the acoustic wave between transducer and laser mode (sound velocity in $PbMoO_4$: 3630 m/s). While high modulation speeds of up to 50 MHz can be reached in this AOM for sinusoidal modulation, the delay, which typically ranges close to 1 μs, limits the use of an AOM in feedback applications. To minimize the delay, the housing of the AOM was removed, allowing proximity of the laser mode to the transducer. A tight focus inside the AOM reduces the beam width, allowing for even closer proximity. However, the alignment of laser mode and AOM at a 17 mrad Bragg angle, combined with the 20mm length of the AOM, limit the minimum distance between transducer and laser mode. The shortest propagation delay T_{AOM} we achieved at a reasonable modulation depth was 200 ns. For alignment, the EDWA is seeded with 5 mW power from a commercial single-frequency laser, resulting in 10 to 20 mW of light at 1534 nm passing through the lenses and the AOM. Received with a photodetector, this setting allows for translational and rotational fine-tuning of the AOM. Finally, when

Bragg angle and minimum delay have been adjusted, photodetector and seed laser are removed and the cavity is closed, operating the EDWA now as a gain medium rather than as an amplifier.

Figure 3-4b shows a typical modulation response of the AOM (lower trace) to the drive signal (upper trace). After a delay of about 200 ns the modulation sets in. The additional slope of the diffraction is due to the finite beam width of the laser mode. Figure 3-4a illustrates the detrimental phase effect caused by this delay. It results in a phase $\varphi_{AOM} = 2\pi \cdot f \cdot T_{AOM}$ that linearly increases with frequency. The open-loop transfer function of the laser control system in Fig. 2-6 is characterized by the integrator $1/sT_R$ established by the cavity [see also eq. (2.35)]. It consumes already 90 deg of the total 180 deg phase margin, leaving only 90 deg phase margin for the control circuit. As shown in Fig. 3-4, the phase φ_{AOM} reaches this margin at a frequency of 200 kHz for a delay of 1 μs, rendering the typical AOM unsuitable for this feedback application. In contrast, the reduction of the delay to 200 ns makes room to a 1 MHz controller bandwidth, just sufficient for active stabilization in this experiment. Figure 3-4 also depicts the phase of a 35 ns delay, established by a steep 6^{th} order Butterworth filter in the control electronics used in the stabilization experiment of Chapter 4. This electronic group delay limits the effective bandwidth of the controller used in the stabilization experiment with a fast LiNb modulator (Chapter 4) to 8MHz. In contrast, the 5ns group delay of the 4th order Bessel filter in the AOM-stabilization electronics of this Chapter has no major impact on the overall bandwidth, compared to the 200 ns propagation delay.

3.2 Measurement results

With a pump power of 200 mW an output power of 0.6 mW is obtained from the 10%-coupler (0.3 mW from the 5% output coupler). In the stabilized cw-mode-locked laser, this corresponds to an intracavity pulse energy of 210 pJ at 29 MHz repetition rate. The corresponding fluence on the saturable absorber, and the fluences incident on the SBR in experiments at higher repetition rates, are within $\pm$ 50% of the estimated saturation fluence $F_{sat} \approx 30\mu\text{J/cm}^2$ of the SBR. Thus, the saturation behavior during laser operation

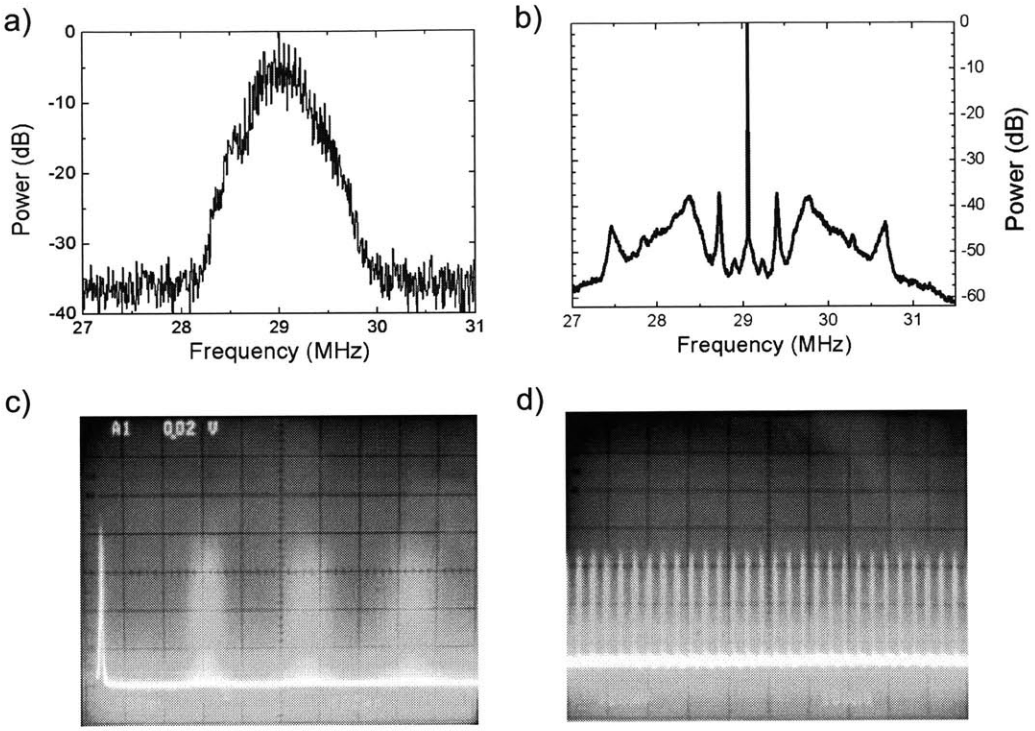

Figure 3-5: Temporal characteristics of the unstable and stabilized laser at 29 MHz. **a)** RF-spectrum in QSML operation and **b)** in stabilized mode-locked state. **c)** Oscilloscope recording of four Q-switch cycles and **d)** of the stabilized mode-locked pulse train.

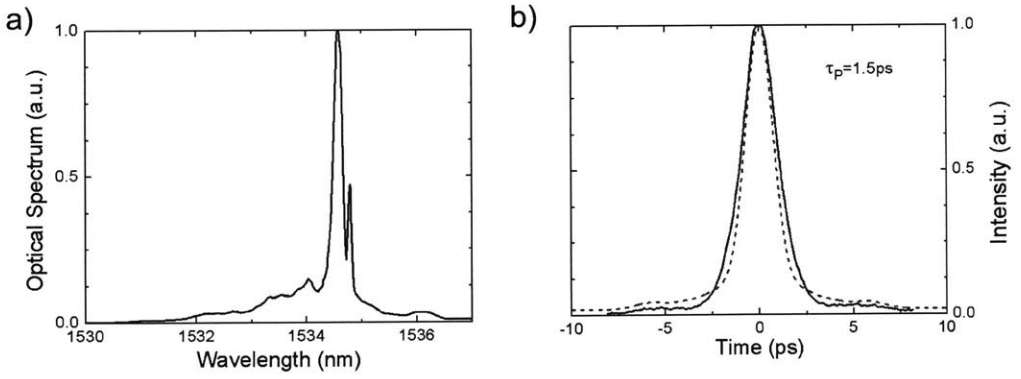

Figure 3-6: Temporal characteristics of the stabilized laser at 29 MHz. **a)** Optical spectrum. **b)** Autocorrelation (solid) and autocorrelation of zero-phase Fourier transform of optical spectrum (dashed).

corresponds approximately to that shown in the dashed trace of Fig. 5-5a. Due to operation at the saturation fluence, close to the point of greatest instability, the laser operates deep within the Q-switching region, the destabilizing effect of the saturable absorber in the stability condition eq. (2.28) assuming a value about three orders of magnitude larger than the stabilizing, negative feedback term on the right-hand side. Consequently, the laser exhibits either pure Q-switching (QS) or Q-switched mode-locking (QSML) at pump powers ranging from lasing threshold to maximum available power (Fig. 3-7c). This behavior is evident from the RF spectrum of the laser without active stabilization (Fig. 3-5a). The laser Q-switches in a highly irregular manner, such that the RF-spectrum shows frequency components distributed over a 1.5 MHz bandwidth around the repetition rate. On the oscilloscope (Fig. 3-5c) a highly unstable Q-switched pulse train appears, with individual Q-switch cycles following the trigger signal washed out (compare the regular Q-switching in Fig. 2-9c). In contrast, when the feedback controller is engaged [3] the Q-switch sidebands are suppressed by 38 dB, resulting in a clean RF spectrum with no further sidebands at higher frequencies (Fig. 3-5b). The pulse train of the stabilized laser shows regular pulses, yet low suppression of noise by only 38 dB manifests itself in a slight pulse-to-pulse jitter that lets the individual pulses appear somewhat smeared out. The stabilized laser shows a smooth optical spectrum centered at 1534.5 nm (Fig. 3-6a). The full-width at half-maximum (FWHM) pulse duration is inferred to be 1.5 ps from the autocorrelation measurements, assuming a Gaussian pulse shape. The measured pulse duration exceeds that extracted from the zero-phase Fourier transform by 20% (Fig. 3-6b). The suppression of noise in the sidebands of the repetition rate is limited only by the available control loop bandwidth, which is dominated by the phase lag introduced by the propagation delay in the AOM. For higher values of feedback gain, the feedback loop becomes unstable and begins to oscillate.

Once engaged, the feedback controller suppresses the slow fluctuations of intracavity

[3]To stabilize the laser it is initially operated in QSML. Light from the 5% output coupler (Fig. 3-2) passes an neutral density (ND) filter wheel with discrete filters (ND 0.5 ... 3.0) *and* a continuously adjustable ND-filter (ND 0.5 ... 1.5). It is focussed with a lens onto the photodiode of the control circuit. First, the photodiode signal is maximized while the output signal of the controller is monitored open-loop with an oscilloscope. Then, the beam is highly attenuated with neutral density filters. Finally, the control loop is closed and the optical attenuation is gradually reduced until the laser reaches stability.

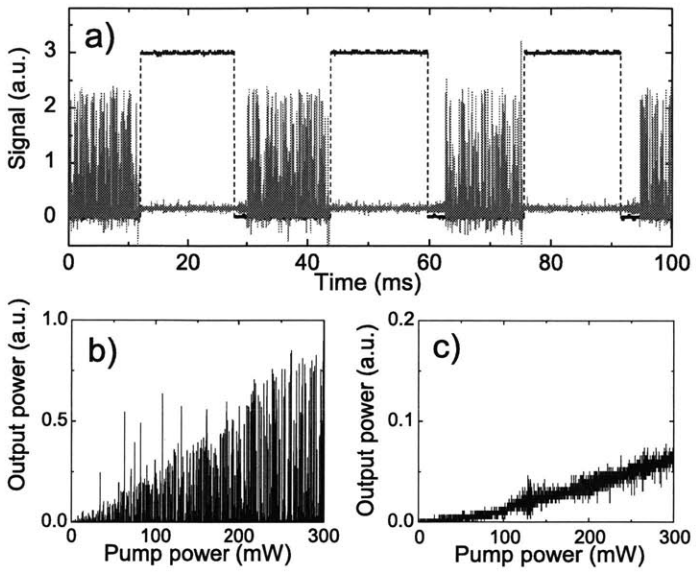

Figure 3-7: **a)** When the controller is blocked by an optical chopper (black dashes), the laser (grey solid) Q-switches, while it is cw-modelocked when the controller is effective. **b)** During rampup of the current the laser Q-switches for all pump power levels without the controller, while in **c)** the instabilities are suppressed by the feedback.

power that constitute the envelope of the Q-switched mode-locked (QSML) pulse train, such that the laser is kept in a stable cw mode-locked state. The controller should be able to both *keep* the laser in stable state, and also be able to *reach* the stable state from unstable QSML. In more general terms, the present system state at any given time depends on the full history of the system [86], and the controller should be able to reach stability regardless of the starting conditions. A particular challenge is established by the transition from the unstable to the stable state, since gigantic power fluctuations have to be levelled out. To test the capability of the controller in this respect, feedback control was periodically turned on and off by blocking the input photodetector of the control circuit periodically with a chopper (CH) (Fig. 3-2). When blocked, the controller is inactive and consequently the laser Q-switches. When the controller is active, suppression is attained reliably within a few Q-switch cycles, as shown in Fig. 3-7a. Computer simulations showed that a sufficient modulation depth, exceeding the amount of saturable loss in the cavity, a low corner frequency of the AC-coupled circuit input (section 2.6 and Fig.

2-12b) and a sufficient controller bandwidth are critical to achieve this robustness. The most critical of these three requirements may be the availability of sufficient modulation depth of intracavity losses. While a number of schemes for fast waveguide modulators, applicable to intracavity loss control in mode-locked waveguide lasers, have been proposed [47, 49], the short cavity length and monolithic design of mode-locked microchip lasers poses a challenge to the integration of an intracavity loss modulator. One proposed loss modulation scheme in microchip lasers utilizes optical carrier injection in an additional layer of the saturable absorber, inducing loss by free carrier absorption [114, 115, 116]. Even if it might only be able to result in a modulation depth smaller than the saturable loss q_0, in [86] it has been shown that a gradual increase of pump power can keep the laser stable at all times, if the controller is activated before the laser is turned on. However, the large modulation depth of the AOM in this experiment allows for robust stabilization, reaching stability under all starting conditions of the system. This ability of the controller, to switch the laser from irregular QSML to a stable cw-mode-locked state, was observed for all repetition rates and power levels.

Another goal of active stabilization, stability over the entire parameter range from threshold to maximum pump power, is attained by use of the AGC in the feedback circuit. This criterion becomes important in commercial applications of mode-locked high repetition rate lasers (section 1.4.1). For example, a few Q-switch cycles occurring during ramp-up of a laser in an optical communications system may lead to burst errors on other transmission channels due to induced fiber nonlinearities [117] or even to equipment damage. In this experiment, the AGC that keeps the time-varying output of the controller at a constant level regardless of the optical power incident on the photodiode (section 3.1) allows the controller to stabilize the laser over the entire parameter range of the laser, for all levels of pump power at a repetition rate of 29 MHz (Fig. 3-7c). Without feedback stabilization the laser exhibits QS and QSML for all power levels, when the pump power of the laser is ramped slowly from zero to 300 mW (Fig. 3-7b). Stability attained over the entire parameter range of the laser is one of the key advantages of active stabilization compared with passive stabilization schemes such as inverse saturable absorption (section 2.7): Passive stabilization depends on operation of the laser at a

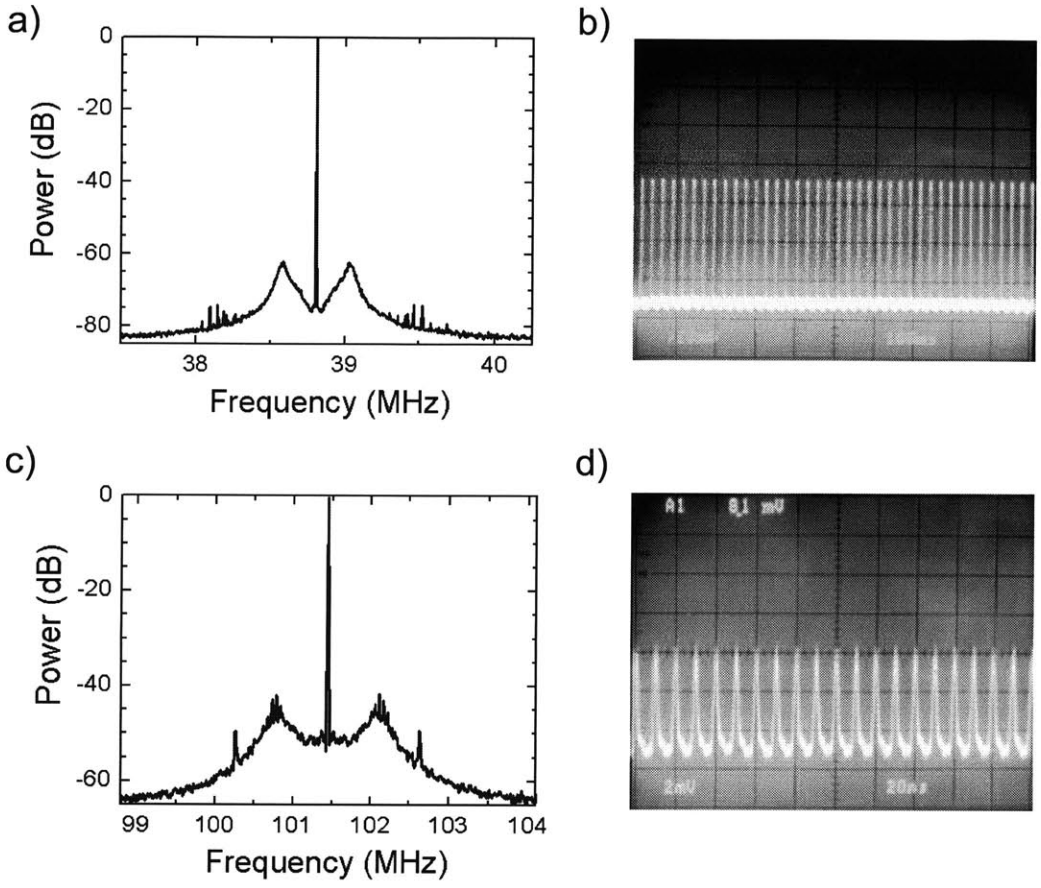

Figure 3-8: RF-spectra with activated controller and pulse train recorded with 150 MHz analog oscilloscope [**a**) and **b**)] at 39 MHz repetition rate and [**c**) and **d**)] at 101 MHz repetition rate.

certain operating point, around which stability is reached only in a narrow environment (section 2.7 and Fig. 2-13b). A narrow operating window can be hard to find under laboratory conditions, impossible to reach in mass produced devices and adds the lurking danger of losing stability once the pump power and device parameters undergo slight changes upon aging and harsh environmental conditions such as temperature fluctuations. In contrast, active feedback that stabilizes the laser over the entire parameter range is immune to slight variations between fabricated devices or surrounding conditions.

Feedback stabilization at higher repetition rates of the laser was also investigated. The fiber lengths were decreased to attain the desirable repetition rate. With the SMF length set to 4.6 m and the DCF removed from the cavity, the repetition rate increases to 39 MHz (-90,000fs^2 net dispersion). At 150 mW pump power a FWHM pulse width of 4.8 ps (12% above the Fourier limit) is observed in autocorrelation measurements, and an output power of 0.96 mW is measured at the 10%-coupler, corresponding to a pulse energy of 250 pJ. The noise level is suppressed as much as 62 dB (Fig. 3-8a) and the pulse train of the stabilized laser recorded with a 150 MHz analog oscilloscope and a 2 GHz detector shows stable and regular mode-locking (Fig. 3-8b). At even higher repetition rates, the phase lag of the AOM renders stabilization increasingly difficult. The repetition rate is increased to 101 MHz by reduction of the SMF to 1.4 m (-10,000fs^2 net dispersion). Pumped with 150 mW of pump power, the output power is 0.9 mW (90 pJ pulse energy) from the 10%-coupler. Stabilized operation is possible only for a narrow range of gain and offset values in the feedback loop. The laser can be stabilized for different values of pump power by manual fine-tuning of the control circuit parameters and a suppression of the noise level to -42 dB is achieved (Fig. 3-8c and d). However, automated stabilization over the entire range of pump power is impossible. In this state, due to the lower intracavity pulse energy and consequently smaller saturation of the absorber, longer pulses are generated.

These results show that the time-dependent loss, introduced by the intracavity modulator, does not adversely affect mode-locking. Intuitively, this can be understood by recalling that (i) the effects of controller and pulse-shaping mechanism occur on different time-scales, and (ii) once stabilized, the loss control mechanism (the AOM) practically exerts a negligible modulation.

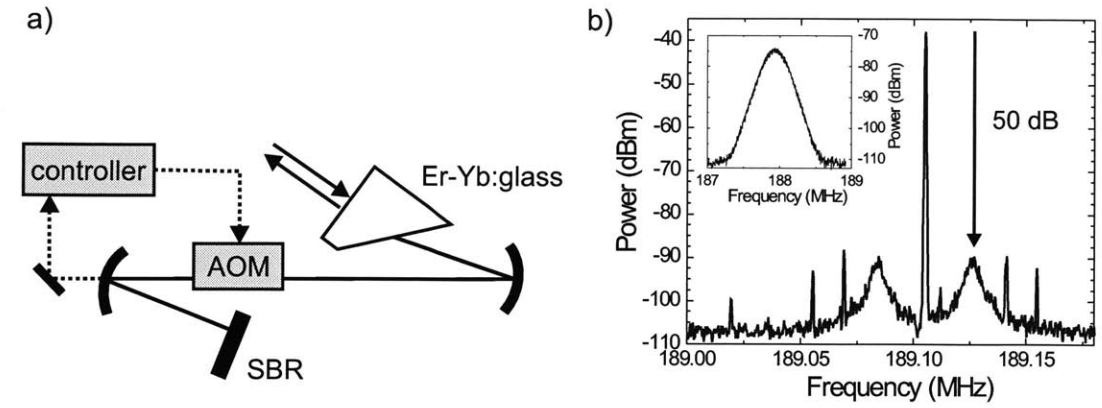

Figure 3-9: Stabilization of a bulk Er-Yb:glass laser with an intracavity loss modulator. **a)** Experimental setup. **b)** RF spectrum of the stabilized laser and (inset) of the Q-switched mode-locked laser.

In conclusion, we have demonstrated suppression of the Q-switching instability in a laser system with millisecond gain recovery time and a strong saturable absorber with 16% saturable absorption by direct feedback control of the net intra-cavity loss. In contrast to modulation of the gain through pump power, this scheme is independent of the properties of the gain medium and applicable to systems with strong saturable absorption. In the future, the demonstrated feedback scheme can be applied to the stabilization of GHz-repetition rate lasers with fast intracavity loss modulators and it permits the use of saturable absorbers in an operating point optimized for pulse shaping rather than stability [76].

3.3 Q-switch suppression in a bulk Er-Yb:glass laser

The active laser control with an acousto-optic modulator (AOM) as an intracavity loss modulator was also demonstrated in an Erbium-Ytterbium:glass (Er-Yb:glass) free-space laser at 189 MHz repetition rate, showing the wide applicability of this stabilization scheme to different laser cavities. The laser serving as the test bed for this experiment (Fig. 3-9a) was similar to the cavity employed for test of the Silicon-Germanium SBR and is discussed in more detail in Chapter 6. It consists of a 2 mm long, flat-Brewster

polished, Er-Yb:glass as the gain element, which is coated with a 0.2% output coupler on one side. The 4-element cavity represents half of a symmetric z-cavity [118, 119, 120] with two folding mirrors, focussing the laser mode to 30x45 μm and approximately 150x150 μm wide spots in gain medium and SBR, as estimated with the ABCD matrix formalism [121] from the stability diagram of the laser. Pumped with up to 300 mW light at 980 nm from a fiber-coupled pump diode, the laser reaches up to 1.5 W intracavity power and an output of 2.85 mW is measured from the output coupler deposited on the gain medium. The saturable absorber (sample m2829C), consisting of a single 3.5 nm wide $In_{0.61}Ga_{0.39}As$ quantum well, embedded in an InP half-wave layer on top of a GaAs/AlAs Bragg reflector, is operated approximately at the saturation fluence, where we assume a value of $F_{sat} = 30\mu J/cm^2$. Consequently, the laser is operated at a power level roughly two orders of magnitude away from stability, judging with the stability condition eq. (2.28). Stability of the laser could only be achieved in this configuration with a significantly smaller spot on the SBR, reached with a shorter radius of curvature of the SBR-focussing mirror.

To allow for stabilization, an AOM is inserted in the long arm at the estimated waist position of the laser mode between the focussing mirrors. With the help of ABCD-matrix calculations [122, 121] the waist size at this position is estimated to be about 250 μm. Unlike the waveguide/ fiber laser configuration, alignment cannot be performed in the open laser cavity with the gain acting as an amplifier. Instead, the bulk laser configuration demands for alignment of position and angle of the AOM during laser operation. The position of minimum waist is found with a series of knife-edge measurements of the section between the focussing mirrors. Once the AOM is inserted and the laser Q-switches, the AOM is driven with a sinusoidal test signal and its position is optimized until the maximum modulation depth and smallest delay appear on a photodetector recording the laser output. Then the feedback loop is closed.

The control circuit, similar to the one described in the previous sections, allows for suppression of Q-switching and noise by about 50 dB (Fig. 3-9b). This result demonstrates the wide applicability of the tested feedback scheme, in different laser configurations. However, the birefringence of the crystal used in the AOM prevented the laser from

reaching a clean mode-locked state: The optical spectrum (not shown) was characterized by a strong modulation and the pulse train emitted form the laser, recorded with a 40 GHz sampling scope, showed pulses of at least 1 ns in duration. Two AOMs, made out of $PbMoO_4$ (Isomet model 1205C-1) and TeO_2 (Neos model 23080-1-1.55-LTD) were tested, at different positions in the cavity and in different orientations with respect to the polarization, showing the same artifact. A solution might exist in the use of AOMs based on fused silica despite their lower modulation depth at 1550 nm. As an amorphous material, fused silica is not birefringent, preventing negative effects on the mode-locking dynamics. Furthermore, it has negative dispersion of -26 fs^2/mm at 1540 nm that contributes to reaching the net negative dispersion regime in the cavity. Finally, its high velocity of sound (5960 m/s), about twice as high as in the materials mentioned above, would reduce the propagation delay and phase lag in the AOM. An AOM based on fused silica was ordered, but never arrived, such that this experiment was no longer pursued.

In conclusion, the stabilization of the bulk Er-Yb:glass laser with an AOM demonstrates the wide applicability of this straightforward implementation of laser control via intracavity loss modulation. Applied with minimum effort to an arbitrary free-space laser, this scheme allows for stable operation. However, a suitable AOM is mandatory to prevent negative implications for the mode-locking dynamics.

Chapter 4

Suppression of Q-switching instabilities with a fast intracavity loss modulator (EOM)

In Chapter 3 we discussed the proof-of-concept experiment of active feedback stabilization with an intracavity loss modulator. Q-switching instabilities, occurring over hundreds of roundtrips, could be suppressed without negatively affecting the mode-locking dynamics on a fast timescale corresponding to the cavity roundtrip time. However, the large phase lag introduced by the acousto-optic modulator (AOM) restricts the effective control bandwidth to about 1 MHz, severely limiting the noise suppression that can be achieved in this experiment. For example, in the Er-doped waveguide laser operated at 29 MHz and 101 MHz repetition rate, noise suppression was limited to about 40 dB, resulting in a stable yet slightly washed out representation of the pulse train on an analogue oscilloscope (Fig. 3-5 and 3-8). The higher stability observed at 39 MHz repetition rate might be a result of different pulse shaping processes in the cavity that is operated at significantly more negative dispersion (-90,000 fs^2 in the 39 MHz cavity vs. -20,000 fs^2 / -10,000 fs^2 in the 29 / 39 MHz lasers).

To eliminate the bandwidth limitations on the feedback controller, the AOM was replaced with a fast, 10 GHz Lithium Niobate ($LiNbO_3$) electro-optic modulator (EOM) as shown in Fig. 4-1. This fast modulator allows for reliable suppression of instabilities

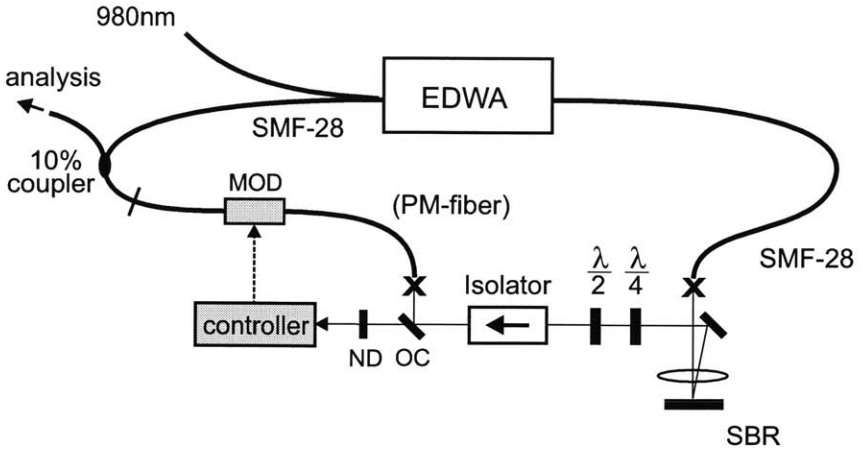

Figure 4-1: Experimental setup of the laser stabilization with a fast loss modulator. Abbreviations: EDWA Er-doped waveguide amplifier, DCF dispersion compensated fiber, SMF single mode fiber, SBR saturable Bragg reflector, OC output coupler, CH optical chopper, ND neutral density filter, AMP driver and amplifier, MOD fiber-coupled $LiNbO_3$ modulator.

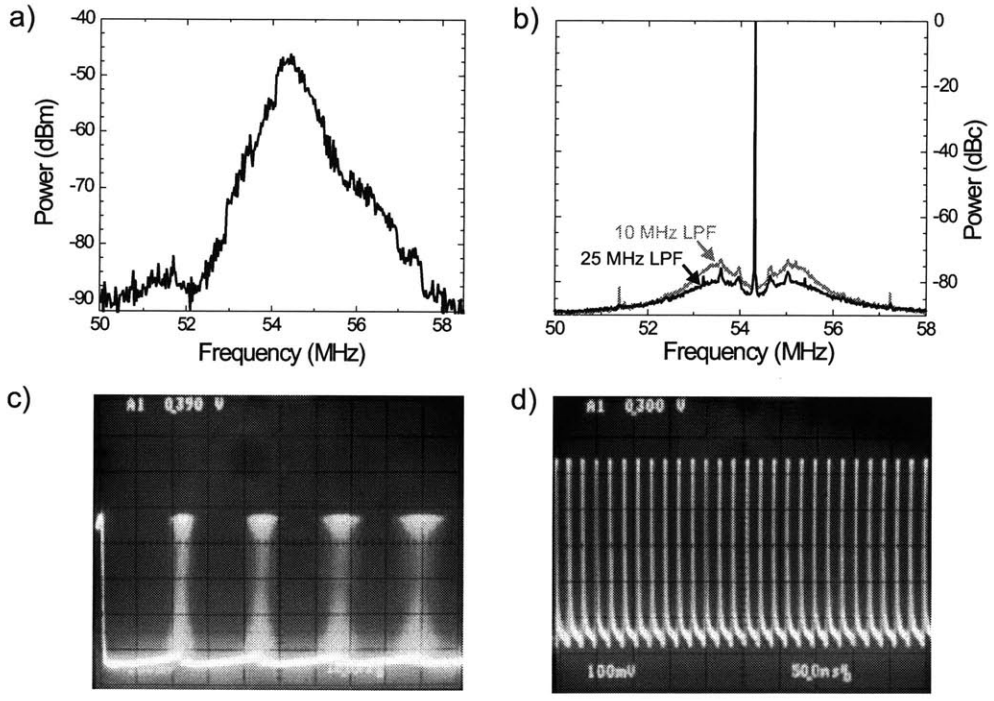

Figure 4-2: Microwave spectra and oscilloscope traces of the unstable [**a)** and **b)**] and stabilized laser [**c)** and **d)**] at 54 MHz repetition rate.

and noise by over 70 dB, resulting in a very clean and stable pulse train, showing that lasers stabilized with active feedback control of an intracavity loss modulator can perform as well as lasers stabilized by passive methods. The result presented in this Chapter confirms the conceptual feasibility of the generation of stable, low-noise and high repetition rate pulse trains in actively stabilized mode-locked microchip and waveguide lasers (section 1.4). Apart from a performance demonstration and a validation of the feedback concept, the system introduced in this section might be attractive for present applications in frequency metrology: Self-referenced optical frequency synthesizers have been limited to sub-150 MHz repetition rates until recently. However, higher repetition rates, such as employed in the 200 MHz system by Mücke *et. al.*, offer larger signal-to-noise ratios of the carrier-envelope beat signal due to increased power per mode, and allow for convenient resolution of individual comb lines in commercial wavemeters [123]. It would be ideal to combine the advantages associated with high repetition rates with the robustness and ease of use of fiber-based frequency comb systems [124]. However, while high repetition rate fiber lasers passively mode-locked via nonlinear polarization rotation [125] have been demonstrated [126], fiber lasers mode-locked with semiconductor saturable absorbers, attractive because of their reliability, have been restricted to lower repetition rates because of Q-switching instabilities. The excellent performance of active laser stabilization and the noise suppression demonstrated in this Chapter allow to combine the advantages of fiber-coupled systems with high repetition rates. The resulting laser system might be used in high repetition rate fiber-based frequency comb systems in the future.

4.1 Experimental setup

To test the stabilization with a fast intracavity loss modulator, the AOM of the system shown in Fig. 3-2 was replaced with a $LiNbO_3$-modulator (Fig. 4-1). Its lead fibers and those of the collimator collecting the light leaving the free-space section are polarization maintaining. The isolator and waveplates in the free-space section of the cavity are aligned to optimize transmission through the EOM. Apart from this change, the cavity is identical with the one discussed in detail in Chapter 3. The repetition rate is limited to 54 MHz

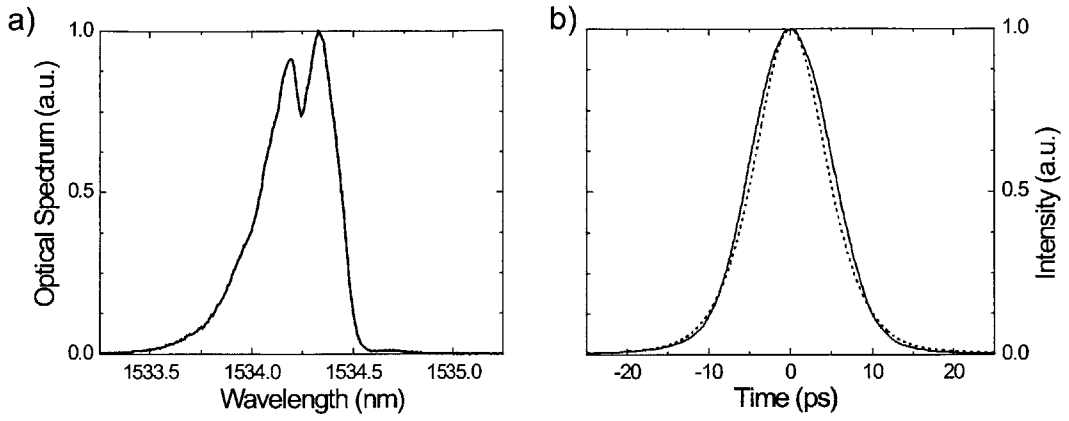

Figure 4-3: **a)** optical spectrum of the stabilized laser. **b)** autocorrelation (solid line) and autocorrelation of the zero-phase Fourier transform of the optical spectrum (dashed line).

by the length of the leads of the modulator, which we decided not to shorten excessively to allow for reuse of the device in the future.

The control electronics was slightly modified to accommodate the wide bandwidth of the modulator and the new repetition rate. The low-pass filter in the controller, preventing the feedback electronics from disturbing individual pulses, was chosen to suppress signals at or above the repetition rate by at least 40 dB. The maximum controller bandwidth resulting from this constraint is determined by the frequency where the combined phase of control electronics and filter reaches reaches 90 deg (see discussion of Fig. 3-4 in section 3.1), completely consuming the available phase margin of the control system in Fig. 3-1. Requesting 40 dB attenuation at the laser repetition rate and limiting the active low-pass to filters of no more than 6^{th} order, the largest bandwidth was found via simulations with the FilterPro^{TM} tool from Texas Instruments [127] in a 6^{th} order Butterworth filter with 25 MHz corner frequency. Its group delay combined with that of the other building blocks of the control circuit was measured as about 35 ns, resulting in an effective controller bandwidth of 8 MHz, about one order of magnitude above the bandwidth reached with the AOM (see Fig. 3-4). Apart from the 25 MHz low-pass, a 6^{th} order Butterworth filter at 10 MHz bandwidth were tested, resulting in good stabilization performance as well. After conclusion of the experiments, we realized that similar filter performance could be

achieved with passive low-pass filters of the PLP-series from Minicircuits Inc [128]. In contrast to active filters, these passive components offer greater ease of use and flexibility since they can just be inserted between controller and modulator and can be readily exchanged, rather than requiring additional circuitry on the PCB. The large group delay of 35 ns observed in our circuit may appear large at first sight. However, it is a result of the attempt to achieve maximum controller bandwidth despite a relatively low repetition rate of the laser: Laser repetition rate and controller cutoff frequency differ by only a factor of two, leading to a steep filter slope that is associated with large excess phase. This slope is unnecessary in the multi-GHz microchip and waveguide lasers targeted eventually by active stabilization, since the transfer function of the control electronics naturally rolls off orders of magnitude below the repetition rate of the laser. According to the formulas derived in section 2.6, in these systems a control bandwidth of tens of megahertz is required for stabilization, as a result of the increased Q-switching repetition rate. This bandwidth requirement can be met with conventional control electronics, as demonstrated with the circuits of appendix A, that show the feasibility of control circuitry with with 5 ns ... 10 ns propagation delay, *i.e.* with about 30 MHz effective bandwidth. Since the these high repetition rate systems the controller bandwidth lies orders of magnitude below the laser repetition rate, steep low-pass filters are not necessary.

Apart from a modified filter bank, the control electronics used in this experiment contained a unity-gain operational amplifier (OPA690) with integrated "disable" function that allows to open and close the control loop electronically with an applied voltage rather than by chopping the control signal optically. This way, the activation time of the controller is reduced from milliseconds to microseconds (compare Fig. 3-7a with Fig. 4-4d) and the high stability of the electronic signal controlling this process can be exploited, allowing for examination of the transition dynamics on the timescale of an individual Q-switch cycle. Furthermore, as detailed in appendix A.2, the automatic gain control was improved, and the resistive divider providing for attenuation of the input signal was replaced with a four quadrant multiplier that offers a propagation delay as low as 2 ns, minimizing the bandwidth-limiting excess phase.

4.2 Measurement results

The $LiNbO_3$ modulator is biased to operate at 20% loss, allowing the controller to both increase and decrease the intracavity loss. Operation of the modulator at zero loss bias is not advisable, since the sinusoidal modulation characteristics of the electro-optic modulator leads to a flat slope of the modulation at zero bias, such that small changes in applied voltage around the zero bias operating point barely introduce additional loss. In contrast, biasing the modulator at a small loss value leads to a slope of the loss vs. applied voltage curve, such that small variations in control voltage lead to the desired changes in loss. This behavior is a characteristic of the acousto-optic and electro-optic modulators used in our experiments and can be avoided with modulators that show a linear dependence of added loss on applied voltage, such as in semiconductor modulators. The output power from the 5% coupler is 0.56 mW when the laser is pumped with 200 mW pump power. With a resulting pulse energy of 100 pJ in cw mode-locked state the absorber is operated close to its estimated saturation fluence of $F_{sat} \approx 30\mu J/cm^2$, and similar to the laser discussed in the previous Chapter, the laser operates deep within the unstable region, with destabilizing feedback exceeding the negative gain feedback by three orders of magnitude in the stability condition eq. (2.28). As a result, the laser exhibits Q-switched mode-locking for all levels of pump power (Fig. 4-4b) and highly unstable QSML with a repetition rate of 45 kHz is observed in the operating point [Fig. 4-2 a) and c)]. However, the wide bandwidth of the feedback controller allows for stabilization of the laser, suppressing the noise level by 75 dB when the filter roll-off is set to 25 MHz bandwidth and by 70 dB in the 10 MHz setting (Fig. 4-2b). On a 150 MHz analog oscilloscope, a very stable pulse train is observed, showing no signs of instabilities in form of amplitude or timing fluctuations (Fig. 4-2d). A clean optical spectrum with a full-width at half maximum (FWHM) of 0.4 nm is observed (Fig. 4-3a). The FWHM pulse duration of the laser is inferred to be 6.8 ps from the autocorrelation measurements, assuming a Gaussian pulse shape. The measured pulse duration exceeds that extracted from the zero-phase Fourier transform by 12% (Fig. 4-3b).

We believe that the noise suppression of at most -75 dB (Fig. 4-2b) is limited by the

noise floor of the electronics, since both increasing and decreasing feedback gain lead to a rising noise level in the experiment: Fig. 4-4a shows the output of the feedback controller for 10 MHz and 25 MHz filter cutoff frequencies, recorded during laser operation while the controller was engaged. Within the control bandwidth a noise floor of about -75 dBm is observed. It originates from a transimpedance amplifier (TIA) that was built to have both high gain and a wide bandwidth of about 100 MHz bandwidth (appendix A.1), to serve as a general purpose front-end of the control circuit in lasers up to GHz repetition rates. The noise gain rises by 20 dB / decade above 10 MHz, as a result of the pole defined by the capacitance on the inverting node (appendix A.1). Use of an OPAMP with lower differential and common mode capacitances as well as a smaller feedback resistor might reduce the noise of the feedback electronics.

The challenge of laser stabilization with a controller whose cutoff lies just a factor of two below the repetition rate — without disturbing the pulse formation on a round-trip timescale — becomes evident from Fig. 4-4a. When the controller with 25 MHz bandwidth is engaged, the frequency component at the repetition rate is suppressed to no less than -55 dBm. In contrast, when the bandwidth is reduced to 10 MHz, the undesired frequency component at 54 MHz falls below -80 dBm, to the level of circuit noise evident in the form of randomly distributed individual spikes in Fig. 4-4a. The stabilization result summarized in Fig. 4-2b indicates that the weak interaction of controller and laser on a round-trip timescale do not perturb the mode-locking dynamics. This is attributed to the large modulation depth of the absorber, of about 16 %. However, for high stability of the pulse train, especially in potential applications in frequency combs, strong suppression of the repetition rate signal is mandatory. The result obtained with the 10 MHz filter shows that this is feasible. In high repetition rate lasers this condition is straightforward to meet this condition, since filter cutoff and repetition rate differ by several orders of magnitude.

Laser stability over the entire pump parameter range is demonstrated in Fig. 4-4b. While the unstabilized laser Q-switches for all levels of pump power (gray trace), stability is attained when the controller is engaged (black trace). This trace shows residual power fluctuations besides the presence of the controller and the AGC. The controller gain had been optimized for maximum stability at highest pump power, and the 25 MHz low-

pass filter was used. The controller gain was found to be very sensitive to deviations from the optimum value as the pump power is increased: While high stability with strong suppression of the noise floor similar to Fig. 4-2b could be achieved at every value of pump power, the constant negative feedback of the AGC provided for stability, but allowed for slight power fluctuations at values of pump power different from the targeted point. A more sophisticated, potentially microprocessor-controlled AGC that matches the negative feedback to the optimum value, following the nonlinear characteristics of A_{11} in Fig. 2-7a, should eliminate this problem.

Finally, the reliability and robustness of active laser stabilization, capable of reaching stability even when the controller is activated in the Q-switched mode-locked state, is demonstrated. For this purpose, the control loop was periodically opened and closed [Fig. 4-2b) and c)]. Without feedback, the laser Q-switches while stability is attained within microseconds after the controller is activated (Fig. 4-2c). Fast capture of the transient between QSML and cw mode-locking became possible only after an electronic chopper was added to the control circuit: When the control loop is chopped with a mechanical chopper in the optical domain (section 3.2 and Fig. 3-7a), the chop frequency is limited to the kHz regime. In addition, frequency fluctuations prevent the resolution of processes on a microsecond timescale. In contrast, when electronic chopping is employed, the control signal is supplied directly by a stable function generator. The unity-gain amplifier with disable functionality, based on an OPA690, can be activated within 25 ns and disabled within 200 ns allowing us to resolve the transients during activation of the control circuit with sub-microsecond precision. Figure 4-2d shows that the laser reaches stability within 10 μs when the controller is activated, preventing further Q-switch cycles to evolve once the controller is engaged.

In summary, the use of a fast intracavity loss modulator permits the suppression of the noise in the laser to levels typical for passively mode-locked lasers that are stable without additional feedback control, resulting in a very stable pulse train. Once the controller is engaged, no further Q-switch cycles develop, indicating the high reliability and stability of the stabilized laser. This experiment demonstrates that an actively stabilized laser can reach a performance comparable to that typical for stable passively mode-locked lasers.

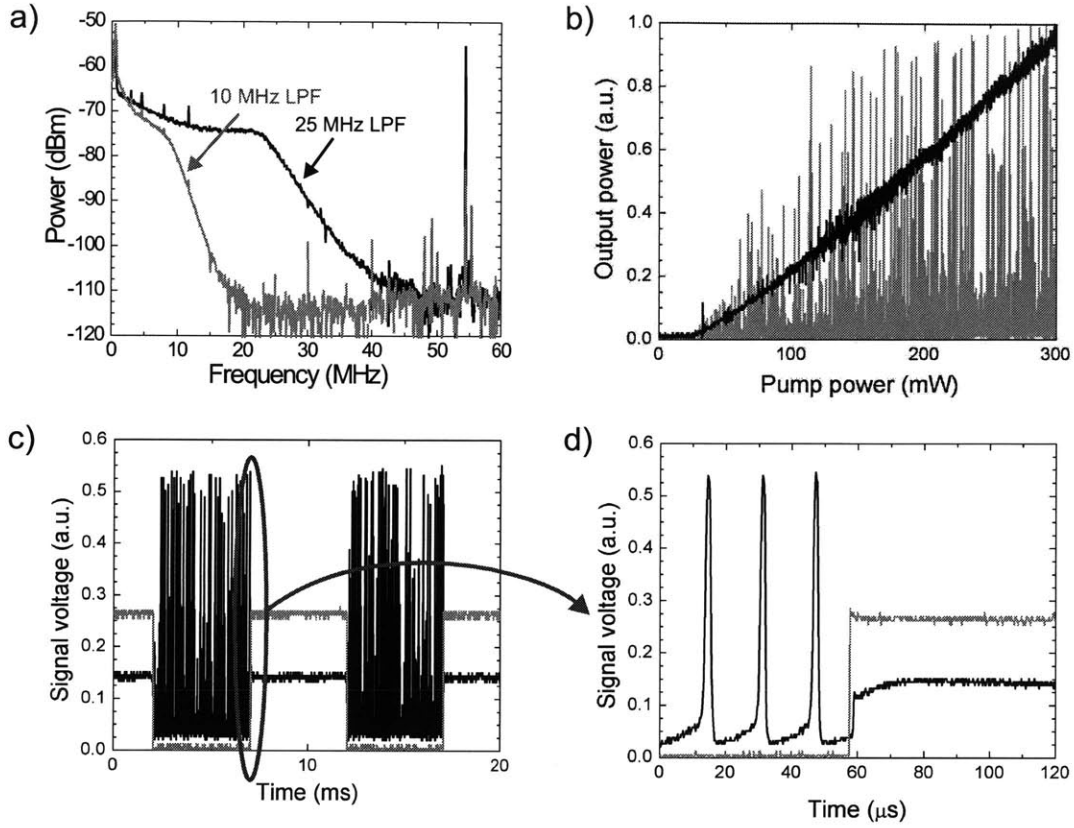

Figure 4-4: **a)** Output of the control circuit during closed-loop laser operation. **b)** Laser output while the laser is ramped from zero to maximum pump power, without (gray) and with (black) the controller engaged. **c)** and **d)** Chopping of the control signal on a long (c) and short (d) timescale. Gray trace - control signal activating the feedback circuit, and black trace - output power of the laser.

It indicates that feedback stabilization via intracavity loss control is suitable for future high repetition rate lasers in real-world applications.

Chapter 5

Silicon-germanium saturable absorbers

In Chapters 2 - 4 we have addressed one of the major challenges to the fabrication of highest repetition rate mode-locked lasers, the suppression of Q-switching instabilities with an active feedback controller. The other challenge to be solved on the way towards fully integrated mode-locked microchip and waveguide lasers is the integration of saturable absorber (SA) and intracavity loss modulator with the gain medium in a suitable materials system. To reach the desired robustness and compactness of the integrated laser, a semiconductor device is required that unites the functionality of a highly reflecting Bragg reflector and a saturable absorber in a compact manner. In this Chapter we present a solution to this integration challenge. We first introduce a fabrication process for highly reflecting silicon - silicon dioxide (Si-SiO_2) Bragg mirrors (section 5.1). The compatibility of this process with both complementary metal-oxide semiconductor (CMOS) manufacturing and with the Erbium-doped glasses used as gain media in the targeted laser systems, as well as the wide bandwidth of the resulting Bragg reflector, render it highly attractive for a wide variety of applications. Based on this Si-SiO_2 reflector we then fabricate a saturable Bragg reflector (SBR) employing a Germanium (Ge) layer as the medium providing saturable loss (section 5.2). Its ultra-fast recovery dynamics and the inverse saturable loss observed at high fluences make this structure an ideal candidate for the high repetition rate lasers envisioned in this thesis.

5.1 Si-SiO_2 high reflectors

Silicon is the material of choice in large-scale integrated electronics. The maturity of existing fabrication technology combined with the high index contrast (HIC) of silicon and its thermal oxide render it attractive for photonic applications and for fulfilling the long-held vision of co-integrated electronic and photonic circuits on a single chip [11, 12, 13, 14, 15]. By leveraging the economies of scale inherent in high-volume silicon fabrication, electronic-photonic integrated circuits (EPICs) are expected to deliver an order-of-magnitude cost-performance improvement facilitating the introduction of ubiquitous OEO-conversions (section 1.1.2), of fully or hybrid integrated mode-locked lasers in WDM systems (section 1.1.3) and of cost-effective optical AD converters (section 1.3). One key component for integrated silicon optoelectronics is a highly reflecting mirror terminated with crystalline silicon layers to allow for subsequent crystalline epitaxial growth. Highly reflecting mirrors are fundamental building blocks for a number of applications, such as photonic-bandgap (PBG) materials and optical micro-cavities [129]. The latter comprise tiny cavity volumes and very high Q-factors that allow for tailoring the spontaneous emission from gain media such as Er-doped silicon [130, 131] embedded in the cavity, permitting for either suppression or enhancement of spontaneous emission [129]. It was a Q-factor of 3.9×10^7 realized in a toroidal micro-resonator that has recently enabled the fabrication of the first laser in the silicon platform [132]. Similar progress may be possible in the future with Er-doped silicon bulk material, once higher Q-factors can be achieved in planar micro-cavities comprising the gain medium. Another major application for highly reflecting Si-SiO_2 mirrors is given by resonant cavity enhanced (RCE) photodetectors, consisting of an absorption layer embedded in a resonant cavity [133, 134]. Here, the effective absorption and consequently detector quantum efficiency are increased by the resonance, while simultaneously a thin active region and consequently high-speed operation are maintained. Finally, the high index contrast of silicon and silicon dioxide ($n_{SiO_2} = 1.45$, $n_{Si} = 3.5$) not only furnishes Si-SiO_2 Bragg mirrors with high reflectivity and broad optical bandwidth (Fig. 5-1), but also renders them omnidirectional - a continuous bandgap is attained for all incident angles and polarizations over a large range

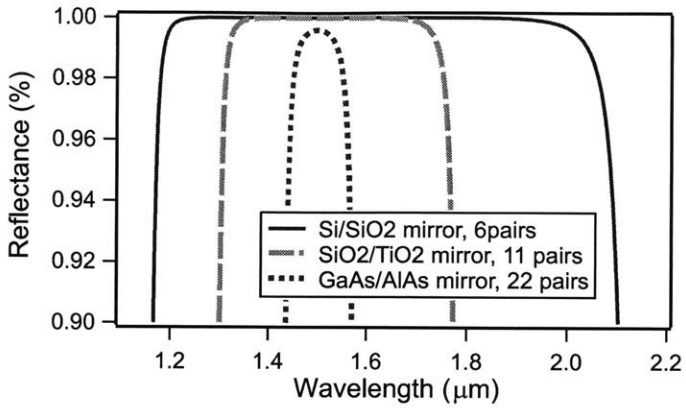

Figure 5-1: Calculated reflectance of Bragg mirrors centered at 1.5 μm in different materials systems

of wavelengths [135, 136]. Both properties make these mirrors attractive for use in solar cells, semiconductor saturable absorbers and as reflective substrates in integrated optics.

For applications in femtosecond mode-locked lasers in general two properties of Si-SiO_2 reflectors are particularly interesting: The wide bandwidth of the Si-SiO_2 reflector, by far exceeding that of integrated mirrors in the un-oxidized GaAs - AlAs materials system, eliminates bandwidth restrictions encountered in monolithic saturable absorbers fabricated in the materials system of III-V semiconductors [1] (Fig. 5-1). Numerous attempts have been made to combine the saturable absorber structure with broadband reflectors, such as metal-dielectric mirrors, requiring elaborate and non-standard processing techniques [138, 139, 140]. The use of a Ge saturable absorber and a Si-SiO_2 reflector offers the opportunity to fabricate an extremely broadband absorber device in a system of fully compatible materials. The other advantage derived from Si-SiO_2-Ge saturable absorbers in femtosecond mode-locked lasers is the fast recovery time of the germanium absorber layer. This property is discussed in detail in section 5.2.

Mode-locked microchip and waveguide lasers in particular benefit from the compatibility of the Si-SiO_2-Ge materials system with Er-doped glass, the gain medium in these lasers, and from the CMOS-compatibility of the fabrication process presented in section

[1]Note however, that recently the bandwidth of SBRs in the AlAs/ GaAs materials system could be significantly extended as well, by oxidizing the AlAs (n=2.9) layers to Al_xO_y (n$\approx$1.6) [137].

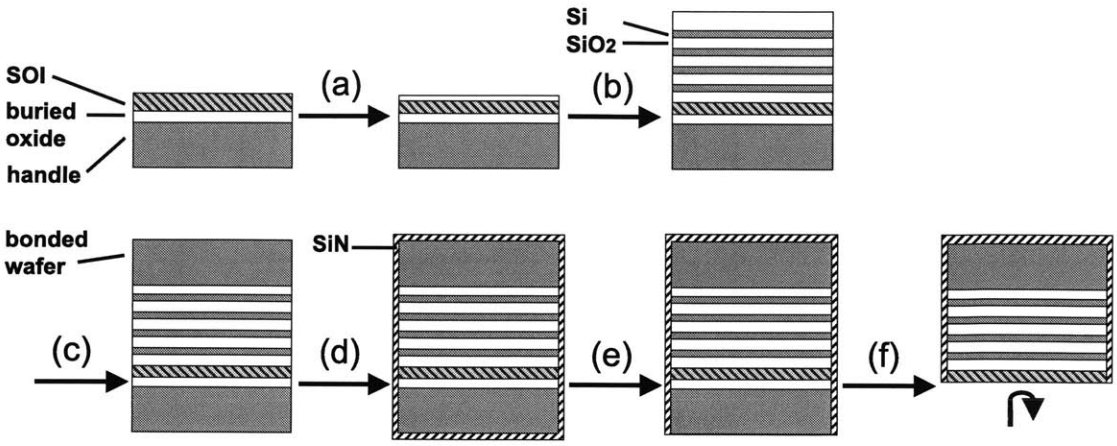

Figure 5-2: Fabrication process of the Si-SiO2 mirror.

5.1.2. It allows one to combine the laser, the saturable absorber and possibly other photonic integrated circuitry cost-effectively on a single silicon substrate.

5.1.1 Prior work on Si-SiO_2 reflectors

Common to all these applications in integrated and ultrafast optics is the challenge to fabricate Si-SiO_2 Bragg mirrors with a crystalline silicon top-layer for subsequent epitaxial growth and with low interfacial roughness preventing scattering losses. A number of approaches based on different manufacturing techniques have been demonstrated to date. First of all, Si-SiO_2 Bragg mirrors can be fabricated by deposition of the multilayer Bragg stack on a silicon substrate layer by layer. In this process, the individual layer pairs are deposited one by one via chemical vapor deposition (CVD) or via repeated deposition of a silicon layer and subsequent partial thermal oxidation, leading to a Si-SiO_2 bi-layer. While inexpensive and straightforward, this method results in amorphous or poly-crystalline material rather than in crystalline silicon films. We found that the surface roughness increases with each deposited bi-layer, resulting in a high roughness of R_{rms} = 10.9 nm (Fig. 5-3b), and in scattering losses, especially pronounced at shorter wavelengths, that reduce the reflectivity far below the value expected from calculations (Fig. 5-4a). Furthermore, we found that even thick germanium layers deposited on the

poly-silicon top-layer do not exhibit the desired absorption at 1500 nm, rendering the structure useless as a saturable absorber. An alternative process for deposition of an Si-SiO_2 reflector relies on electrochemical etching for the fabrication of porous silicon layers with indices between 1.5 and 2.7 [131, 136]. However, the resulting material is porous, preventing subsequent crystalline epitaxial growth, and grain formation limits the highest achievable reflectivity. In contrast, crystalline silicon top-layers have been obtained by repeated application of the separation-by-implanted-oxygen (SIMOX) process resulting in mirrors with 90% reflectivity [141]. The disadvantage of this process lies in the large defect density in the silicon layer caused by ion implantation and the dependence of interface morphology on the thickness ratio of Si-SiO_2 layers. Finally, repeated application of the Smart Cut process [142] has resulted in Si-SiO_2 mirrors comprising up to three bi-layers that are terminated with high-quality crystalline silicon layers [133, 143]. While providing films of highest quality, low yield and high cost limit the practical applicability of this process. A possible solution is the recent approach to deposit Si-SiO_2 mirrors from the backside in holes etched through handle and buried oxide of a silicon-on-insulator wafer (SOI-wafer) by means of CVD [144]. This process does not compromise the crystalline film quality of the SOI-layer serving as the starting material, it relies exclusively on standard fabrication processes, and a reflectivity in excess of 99% has been reported. In this Chapter, we extend this approach to the fabrication of Si-SiO_2 Bragg reflectors with high-quality crystalline top-layers that cover the entire surface area of a wafer and exhibit a very high reflectivity. Challenges similar to the one addressed here, the fabrication of broadband high reflectors in the silicon materials system, have previously been solved in the platform of III-V compound semiconductors. For example, in vertical cavity surface emitting lasers (VCSELs) which rely on a high quality active zone but also need a high reflector, Bragg mirrors fabricated in different materials systems have been attached by means of wafer fusion [145], by deposition of dielectric-metallic reflectors with subsequent substrate removal [146] or in form of Al_2O_3/α-Si top reflectors [147]. However, the manufacturing process presented here allows to fabricate a wafer-scale epitaxy-ready Si-SiO_2 high reflector in first process step, that allows one to deposit the device layers then in subsequent fabrication steps. This way the deposited device layers are not exposed

to processing other than their direct deposition, a condition useful because of the strict requirements for cleanliness in CMOS environments.

5.1.2 Fabrication process

Our CMOS-compatible fabrication process was developed in collaboration with Professor Kimerling's group, where Shoji Akiyama carried out the complete fabrication and all linear characterization. Our process relies on chemical vapor deposition of the Si-SiO_2 reflector on an SOI wafer and subsequent reversal of the multi-layer sequence with respect to layer growth (Figure 5-2). In the first step, the silicon thickness of an SOI wafer, fabricated with the Smart Cut technique [142], is reduced to its desired value (210 nm) by thermal oxidation (step a). Then, a 6-pair reflector, centered at 1400 nm wavelength, is fabricated by repeating deposition of 202 nm thick poly-silicon (620°C, 150 sccm SiH4, 200 mTorr) and subsequent wet oxidation, resulting in partial oxidation of the poly-silicon films to 103 nm poly-Si and 224 nm oxide (step b). Wet oxidation was carried out at 900°C, since lower temperatures result in impractically long oxidation times, while higher ones (1000°C, 1100°C) were found to increase interfacial roughness [148]. All deposition processes in this chapter lead to thin film deposition on both sides of the wafer, since the CVD deposition processes allow the surface reaction to occur on both sides of the wafer. Deposition of the mirror is finally completed with a thicker SiO_2 layer whose surface is then prepared by chemo-mechanical polishing (CMP) for wafer-bonding. In the next step, the processed wafer is bonded at 1050°C with a bare silicon wafer, serving as the new substrate (step c). N2-annealing is applied for 4 hours to strengthen the bonding energy. Then, an LPCVD low-stress silicon-rich nitride is deposited as a KOH mask protecting the new, bonded substrate (step d). The handle of the SOI-wafer is exposed by removing its SiN-cover with an additional CMP step (step e) and then removed in a KOH-etch (10 wt% solution, 70°C). Finally, the buried oxide of the SOI-wafer is removed in a buffered HF solution (step f), leaving the SOI-layer as the top-layer of the fabricated Si-SiO_2 Bragg reflector. The buffered HF solution provides an etch selectivity of 1000:1, resulting in a smooth surface of the mirror. The outcome of our fabrication process is a highly reflecting Si-SiO_2 reflector, terminated with a crystalline silicon layer. We have

used it [13] as a substrate for growth of a Si-Ge saturable Bragg reflector, and deposited additional Ge, SiO_2 and Si layers on the reflector (section 5.2). Limited cleanliness in our multi-user university facility limited the reliability of wafer-bonding between deposited Bragg reflector and the new substrate (Fig. 5-2, step c). Partial bonding in a 1" wide region around the edge of the 4" wafer was frequently observed. This limitation does not constitute a principal problem and can be eliminated under industrial fabrication conditions, as the high volume fabrication of SOI-wafers demonstrates [142].

5.1.3 Characteristics of the fabricated Si-SiO_2 high reflectors

The demonstrated fabrication process results in reversal of the Si-SiO_2 layer sequence of the reflector with respect to layer growth. Thus, the layers of lowest surface roughness - those that have been grown first - end up topmost in the mirror, exposed to the highest electric field strength, while the rougher layers, grown last, are buried deep in the mirror. This property is evident from the TEM image of the fabricated device, combined with the calculated field intensity at a wavelength of 1530 nm (Fig. 5-3a). The image shows very smooth interfaces adjacent to the SOI top-layer and an increasing interfacial roughness in the direction of the layer growth - towards the new, bonded substrate at the bottom of the reflector. We attribute this increase in roughness to the growth of grains in the poly-silicon material and to the variation of oxidation rates between grains and grain boundaries [149]. However, both interfaces of the SOI top-layer, coincident with the highest peaks of field strength, are formed by thermal oxidation and thus exhibit excellent morphology (Fig. 5-3a): The interface close to the surface of the structure is formed during the fabrication of the original SOI-wafer with the Smart Cut process, and the interface adjacent to the Bragg mirror by thermal oxidation in the first fabrication step of the mirror (Fig. 5-2, step a). Besides low roughness, these interfaces constitute a good passivation of the SOI-layer that can result in long carrier lifetimes in the silicon film, a property important for opto-electronic semiconductor devices, such as optical modulators based on carrier injection [49]. Altogether, the smooth interfaces of the SOI-layer, combined with the reversal of the layer sequence, significantly reduce surface roughness and scattering losses of the device.

The film quality on the surface of the fabricated Si-SiO_2 reflector was inspected with

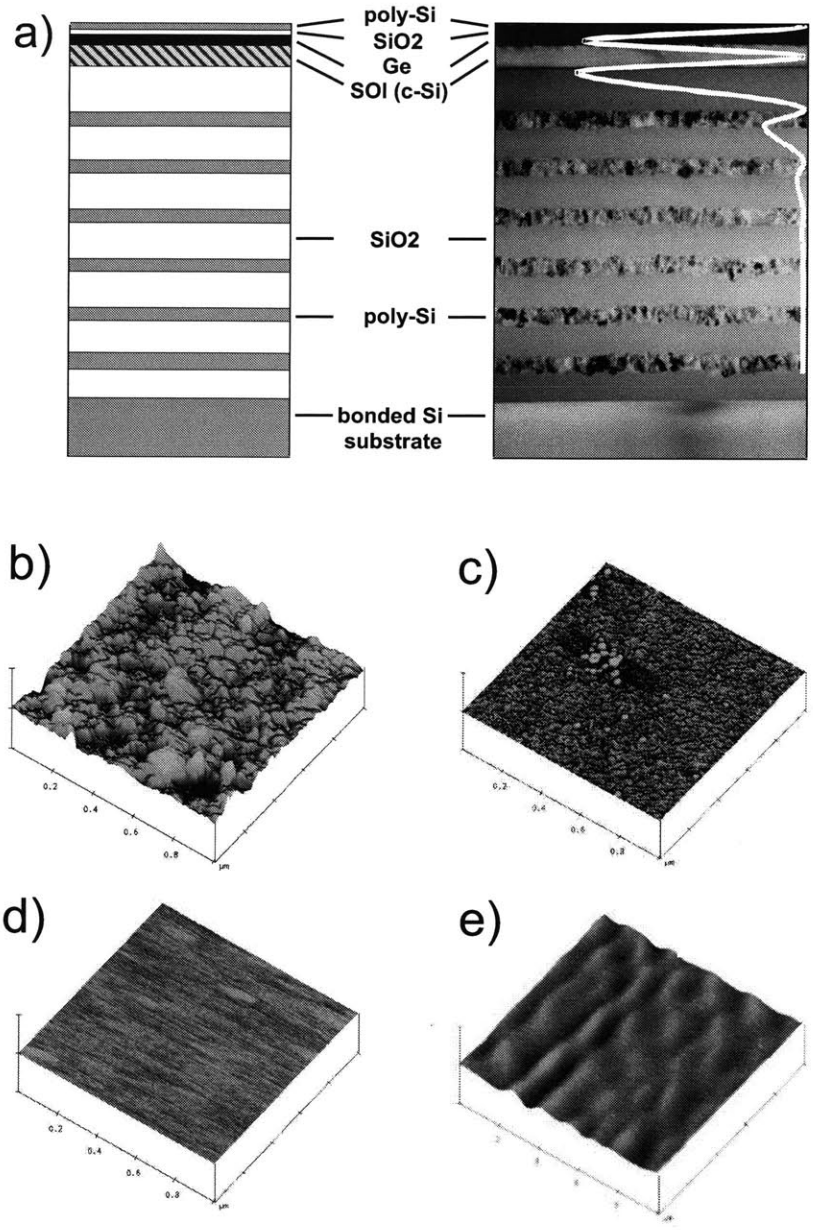

Figure 5-3: Characteristics of the Si-SiO_2 reflector. **a)** Left: Schematics of layer structure. Right: TEM photograph of a Si-Ge saturable Bragg reflector. Calculated intensity profile (white) at 1530 nm. **b)-e)** AFM images of the reflector surface. b) 6-pair mirror after deposition and before reversal of layer sequence. c) Si-SiO_2 Bragg mirror deposited on a regular Si wafer after substrate removal. d) Completed Si-SiO_2 reflector terminated with a crystalline SOI layer. e) Si-SiO_2 reflector with deposited 40 nm Ge layer. Panels b)-e) courtesy of Shoji Akiyama.

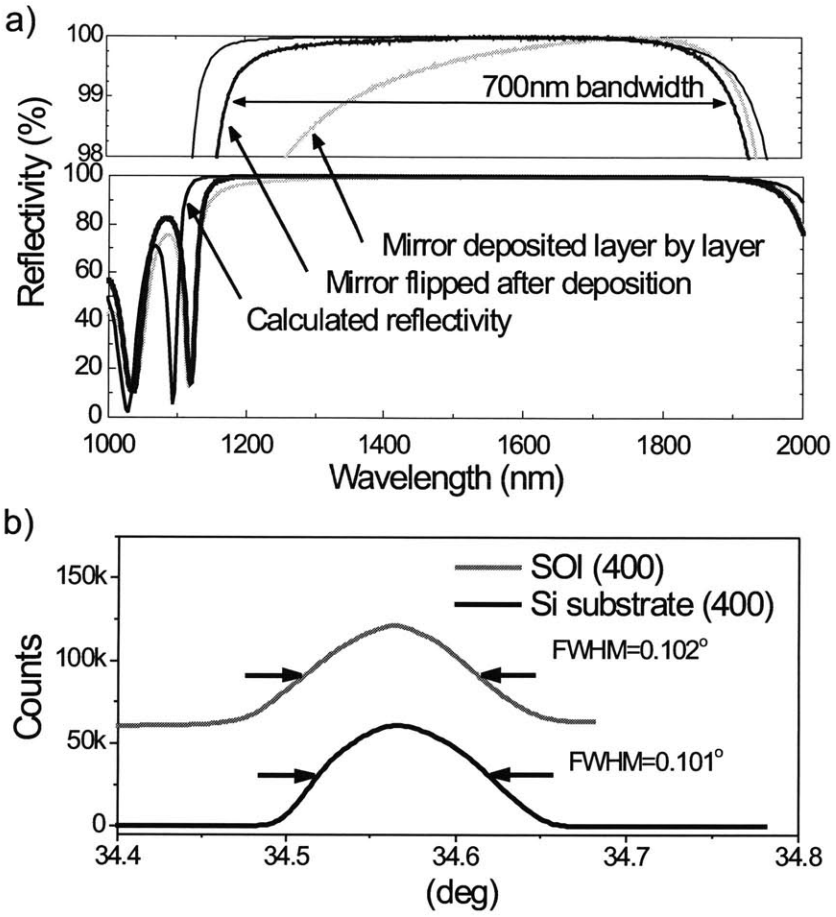

Figure 5-4: **a)** Measured and calculated reflectivity of the Si-SiO_2 Bragg mirror. **b)** X-ray diffraction image of the mirror terminated with a crystalline SOI layer. Panel b) courtesy of Jifeng Liu.

Table 5.1: Measured surface roughness of 6-pair Si-SiO_2 reflectors

Structure	**Surface roughness***
Reflector directly after deposition	10.9 nm
Reflector deposited on Si-wafer after removal of substrate and first oxide layer	0.78 nm
Reflector deposited on SOI-wafer after removal of substrate and buried oxide	0.136nm
" with additional Ge-layer	0.366 nm

* *in a 1 μm^2 area*

an atomic-force-microscope (AFM). The 6-pair reflector, deposited layer by layer out of poly-crystalline material exhibits high surface roughness of R_{rms}=10.9 nm in a 1x1 μm area (Fig. 5-3b). Reversal of the layer sequence allows us to reduce this value by more than one order of magnitude: Figure 5-3c shows the AFM-image of a 6-pair reflector, deposited on a silicon wafer, after removal of the substrate and layer reversal. The top layer of this structure is now the first poly-crystalline silicon layer deposited in the fabrication process, exposed on the surface of the device. Its roughness is evaluated as R_{rms}=0.78 nm, over ten times better than that measured on the layer stack directly after deposition. A further improvement in roughness is achieved when an SOI-wafer is used as the substrate for growth instead of a regular silicon wafer, and when both handle and buried oxide of the SOI-wafer are removed to expose the SOI-layer terminating the 6-pair reflector (Fig. 5-3d). Now, the roughness drops to R_{rms}=0.136 nm in a 1x1 μm area, revealing the potential of a crystalline top layer. This value lies well within the target of $R_{rms} <$ 0.2 nm, envisioned in the product roadmap for ultrathin SOI [150]. When an additional germanium epi-layer is deposited on the reflector with crystalline SOI-top-layer, *e.g.* in the fabrication of a saturable Bragg reflector (section 5.2), a slight increase in roughness to R_{rms}=0.37 nm is observed (Fig. 5-3e). The measured values of surface roughness are summarized in table 5.1.

The surface roughness of the different mirrors of Table 5.1 is reflected in the reflectiv-

ity values of the fabricated devices. Figure 5-4a contrasts the ideal, calculated reflectivity of the 6-pair reflector with a measured reflector deposited layer-by-layer and the measured reflector after reversal of the layer sequence according to our fabrication process. Scattering loss degrades the reflectivity, especially for shorter wavelengths, in the mirror that is deposited layer-by-layer. This loss is significantly reduced by reversal of the layer sequence after deposition, such that the reflectivity of the flipped mirror structure closely approaches the calculated value. It reaches an unprecedented 99%-reflectivity bandwidth of 700 nm (Fig. 5-4a). We attribute the remaining deviation from the calculated value mostly to undesired thickness variations in the Si-SiO_2 layers. To determine the peak reflectivity of the reflector, it was used as an end mirror in an Er-Yb:glass laser [151]. Then, the output power of the laser, obtained with the Si-SiO_2 mirror, was compared with the output power measured from the laser, when the Si-SiO_2 mirror was replaced by well-characterized mirrors of 99.5%, 99.75% and 99.95% reflectivity. From this series of measurements, the reflectivity of the Si-SiO_2 mirror is estimated to be approximately 99.8% at the laser wavelength of 1530 nm. Further enhancements can be expected from improvements in interface morphology, e.g. from SiO_2 growth via low pressure tetraethooxysilane (TEOS) deposition [152].

In addition, the crystallinity of the SOI layer was studied by X-ray diffraction with a Rigaku 250 mm high-resolution Bragg-Brentano diffractometer. Figure 5-4b shows the rocking curves of both the SOI top-layer and the bonded Si substrate. X-ray diffraction reveals that there is a small angle mismatch of about 0.3 between the (400) crystal planes of the SOI layer and the silicon wafer, introduced by the wafer bonding process. Making use of this slight offset, the rocking curves of the Ka1 (400) diffraction peaks from the SOI layer and the substrate can be separated by tilting the sample to an adequate angle. Both rocking curves have a very similar full width at half maximum (FWHM) of about 0.10°, indicating that the crystalline quality of the SOI layer is comparable to the Si substrate.

In conclusion, we have developed an Si-SiO_2 Bragg reflector with the highest reflectivity and largest bandwidth values to date at the telecommunications wavelength, terminated by a crystalline silicon layer of high quality that allows for subsequent epitaxial growth. Our fabrication process relies on standard CMOS techniques and comprises only

one step of wafer-bonding. Its inherent simplicity and high yield therefore render it well-suited for production of highest quality, epitaxy-ready silicon-based Bragg reflectors in a high-volume manufacturing environment.

5.2 Silicon-Germanium saturable absorbers

The Si-SiO_2 reflectors introduced in the previous section constitute one of the major components for the construction of a compact and monolithically integrated mode-locked laser: a cavity end-mirror. Together with the gain medium they may allow for construction of an integrated laser in the silicon platform, for example with Erbium-doped or Ytterbium-doped glass as the gain medium. However, in order to reach pulsed operation, the gain medium and the cavity established by these reflectors must be complemented by a saturable absorber (SA), a device that allows for pulse formation and stabilization in the cavity by providing intensity dependent loss [153, 91]. Saturable Bragg reflectors (SBRs) combine the functionality of a mirror with that of the saturable absorber, by incorporating a semiconductor layer that provides for saturable loss on top of a Bragg reflector. To date, SBRs have been fabricated both as bulk and quantum well devices from III-V compound semiconductor materials which are not compatible with the silicon material platform [87, 66].

In this section we present the first silicon-germanium SBR (SiGe-SBR) composed of an Si-SiO_2 Bragg reflector and a germanium (Ge) saturable absorber layer. This structure is fully compatible with the materials platform envisioned for compact mode-locked lasers (section 1.4). Our results prove the feasibility of silicon-germanium saturable absorbers, whose materials system is compatible with the gain medium erbium-ytterbium:glass. However, in this place we do not address the challenge of actually fabricating an integrated laser, which requires not only a compatible materials system but also a manufacturing process whose individual steps are compatible to each other. Besides materials compatibility, the ultra-wide bandwidth of the Si-SiO_2 reflector, its high peak reflectance of 99.8% and the broadband absorption of germanium render SiGe-SBRs highly attractive for use in mode-locked lasers in general. Octave-spanning lasers in frequency metrology [154, 123]

and synchronization of lasers with overlapping optical spectra [155, 156] require ultra-broadband optics. While laser mirrors fulfilling the bandwidth requirements are readily obtained via chirping or double-chirping of the high and low index layers [157, 158, 159], reliable semiconductor saturable absorbers that equal the bandwidth of common laser gain media used in these experiments[2] are not available to date. Broad back-mirrors have been fabricated via deposition of metallic-dielectric mirrors and subsequent substrate removal to increase the bandwidth of SBRs fabricated with III-V semiconductor materials [138, 139, 140], however the need for elaborate and non-standard processing methods has prevented wide application of this technique. In contrast, the silicon-germanium SBR (SiGe-SBR) demonstrated here consists of a CMOS-compatible Si-SiO_2 Bragg reflector and a germanium saturable absorber layer (Fig. 5-5a).

5.2.1 Device structure and characteristics

The silicon-germanium SBR comprises an Si-SiO_2 reflector that is centered at 1400 nm and is terminated with a crystalline SOI top-layer. It is fabricated with the layer-reversal and substrate removal technique discussed in section 5.1.2. On the SOI-layer a 40 nm thick germanium layer is deposited by Jifeng Liu, also of Professor Kimerlings group, that provides for saturable loss (Fig. 5-5a). The thickness of the SOI-layer was adjusted to locate the Ge layer in a peak of the electric field to maximize absorption and minimize saturation intensity. For this purpose, the thickness of the SOI layer of the SOI-wafer, that serves as starting material, was reduced by thermal oxidation (Fig. 5-2, step a). Alternatively, the thickness of the silicon layer beneath the Ge-layer could be increased by deposition of additional (crystalline) silicon. The Ge layer is protected with a 10 nm SiO_2 buffer layer and covered with a 70 nm Si layer that locates a null of the electric field at the mirror surface, reducing the damage threshold of the device. The use of the thin SiO_2 buffer layer was motivated by the observation that deposition of a Si layer directly on top of the Ge layer strongly reduced the absorption of the device, possibly due to formation of eutectic bonds at the Si-Ge interface.

The linear absorption characteristics of the SiGe-SBR is shown in Figure 5-5b. The

[2]such as Cr:Forsterite, Cr:YAG and Ti:sapphire.

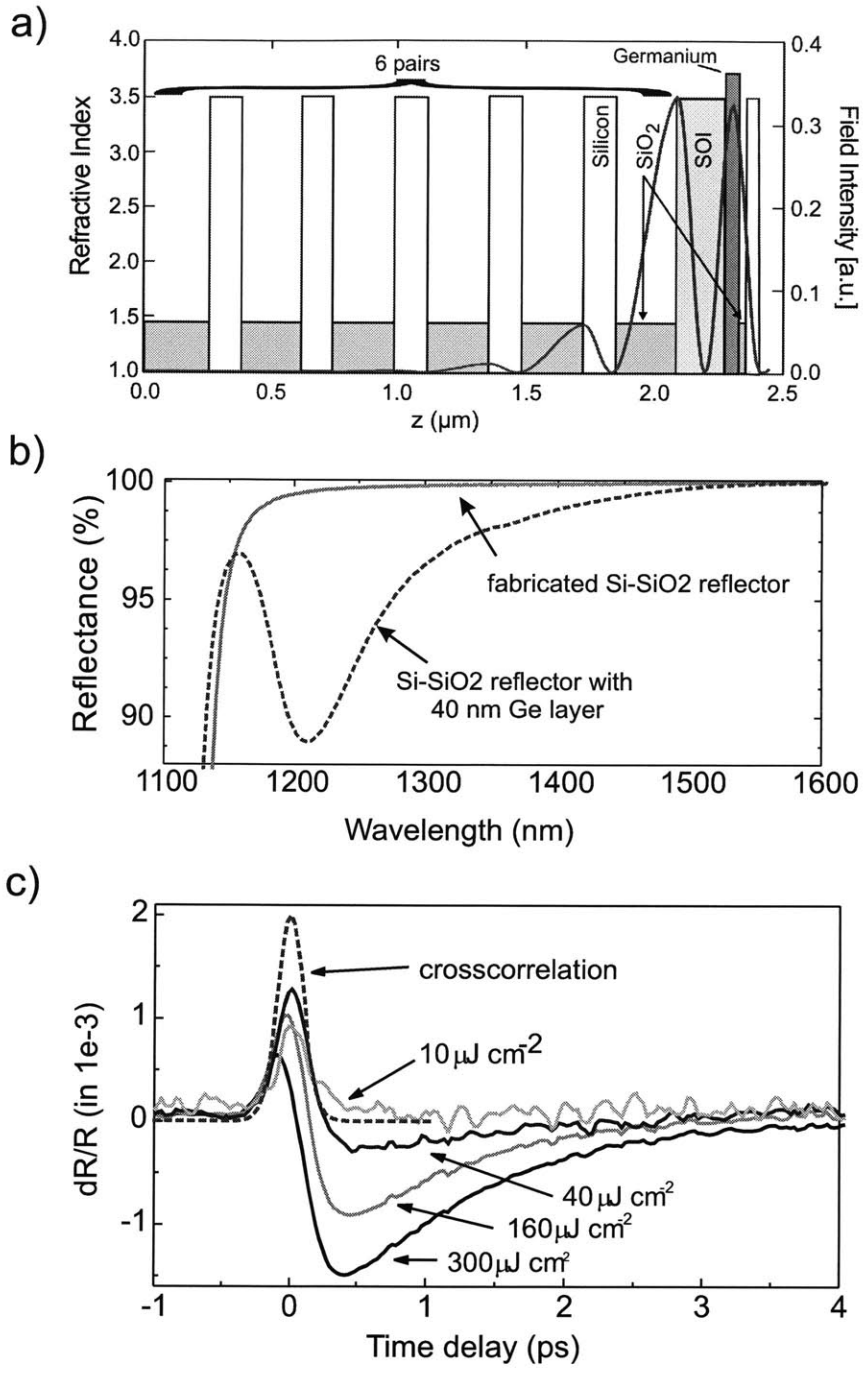

Figure 5-5: **a)** Refractive index profile and standing wave pattern of the SiGe-SBR. **b)** Measured reflectivity of the 6-pair Si-SiO_2 Bragg mirror with and without germanium layer. **c)** Pump-probe traces of the SiGe-SBR taken at various fluence values (solid) along with the cross-correlation of the pump probe laser source (dashed). Panel c) courtesy of Juliet Gopinath and Hanfei Shen.

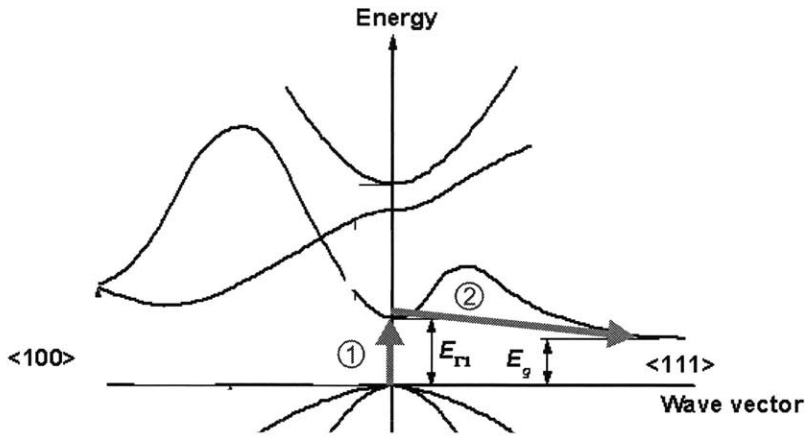

Figure 5-6: Bandstructure of germanium (from [2]).

absorption of the germanium sets in at 1580 nm. The absorption edge of the Ge film is shifted to shorter wavelengths due to compressive strain resulting from a 4% mismatch in lattice constants of silicon and germanium [160]. From the measured strain we calculate a shift of 38 nm. As a result, a total loss of 0.3%, and a nonsaturable loss of 0.17% are determined at 1540 nm, the center wavelength of the Erbium-Ytterbium:glass laser mode-locked with the SiGe-SBR (chapter 6) via comparison of the intracavity power obtained with the SiGe-SBR with different output couplers. In addition, a transmission electron micrograph revealed a small error in the SOI-layer thickness, placing the Ge-absorber layer slightly off the peak of the electric field. A larger modulation depth of the SBR can be expected from a precise positioning of the Ge layer at a field maximum, as well as by the use of a thicker layer. Figure 5-5b reveals a strong increase in absorption towards shorter wavelengths with a resonance at 1150 nm. SiGe-SBR with Si-SiO_2 reflectors shifted slightly towards shorter wavelengths and with an adjusted structure embedding the Ge absorber layer are promising candidates for use in Cr:Forsterite lasers.

The nonlinear response of the device was characterized by Juliet Gopinath and Hanfei Shen of Professor Ippen's group at MIT in a series of pump-probe measurements with 150 fs pulses centered at 1540 nm from an optical parametric oscillator (Fig. 5-5c). For low to medium fluence values (e.g. 40 $\mu J/cm^2$), we observe sub-picosecond recovery of the bleaching with up to 0.13% of modulation depth. The temporal resolution of our measure-

ment is limited by the pump- and probe pulse durations. This observation was confirmed, when the pump-probe measurement was repeated with 40 fs pulses [161]. Consequently, the SiGe-SBR acts as a fast saturable absorber in 1540 nm lasers with larger than 150 fs pulse durations, for example the Er-Yb:glass laser of Chapter 6. We attribute the fast relaxation process to intervalley scattering within the conduction band of germanium, which is an indirect semiconductor, and assume that absorption occurs at $k = 0$ [process (1) in Fig. 5-6] followed by fast scattering to the conduction band minimum at $k > 0$ [process (2) in Fig. 5-6]. In contrast, for high fluences (e.g., 300 μJ/cm^2), free carrier absorption (FCA) in the germanium layer due to generated carriers turns the SBR into an inverse saturable absorber. Two-photon absorption (TPA), which is much greater in germanium ($\beta_{Ge,1500nm}$ = 300 cm/GW) than in silicon[3], gallium arsenide[4] or indium phosphide[5] may also play a role. The observed behavior leads to dual functionality of the SiGe-SBR in a mode-locked laser: (i) the fast recovery enables ultrashort pulse generation, (ii) onset of inverse saturable absorption at high fluences acts as an inverse saturable absorber stabilizing lasers at high repetition rates against Q-switching instabilities (section 2.7). From pump probe measurements we estimate the saturation fluence to be about 30 μJ/cm^2. In conclusion, we have fabricated a silicon-germanium SBR with a Si-SiO_2 backmirror. The wide bandwidth of 700 nm, the sub-picosecond recovery time and the large amount of inverse saturable absorption make this SBR very attractive for applications in ultrafast optics in general. Furthermore, the compatibility of the Si-SiO_2-Ge materials system with silicon processing technology makes this absorber ideal for mode-locking integrated microchip and waveguide lasers.

5.2.2 Future work

The outstanding characteristics of the SiGe-SBR with respect to bandwidth and recovery time trigger high interest in a full exploration of the potential of SiGe-absorbers and in the fabrication of similar devices at other common laser wavelengths. At communications

[3] $\beta_{Silicon} \approx 1$ cm/GW [162, 163]
[4] $\beta_{GaAs} \approx 30$ cm/GW [164]
[5] $\beta_{InP} \approx 60$ cm/GW [165]

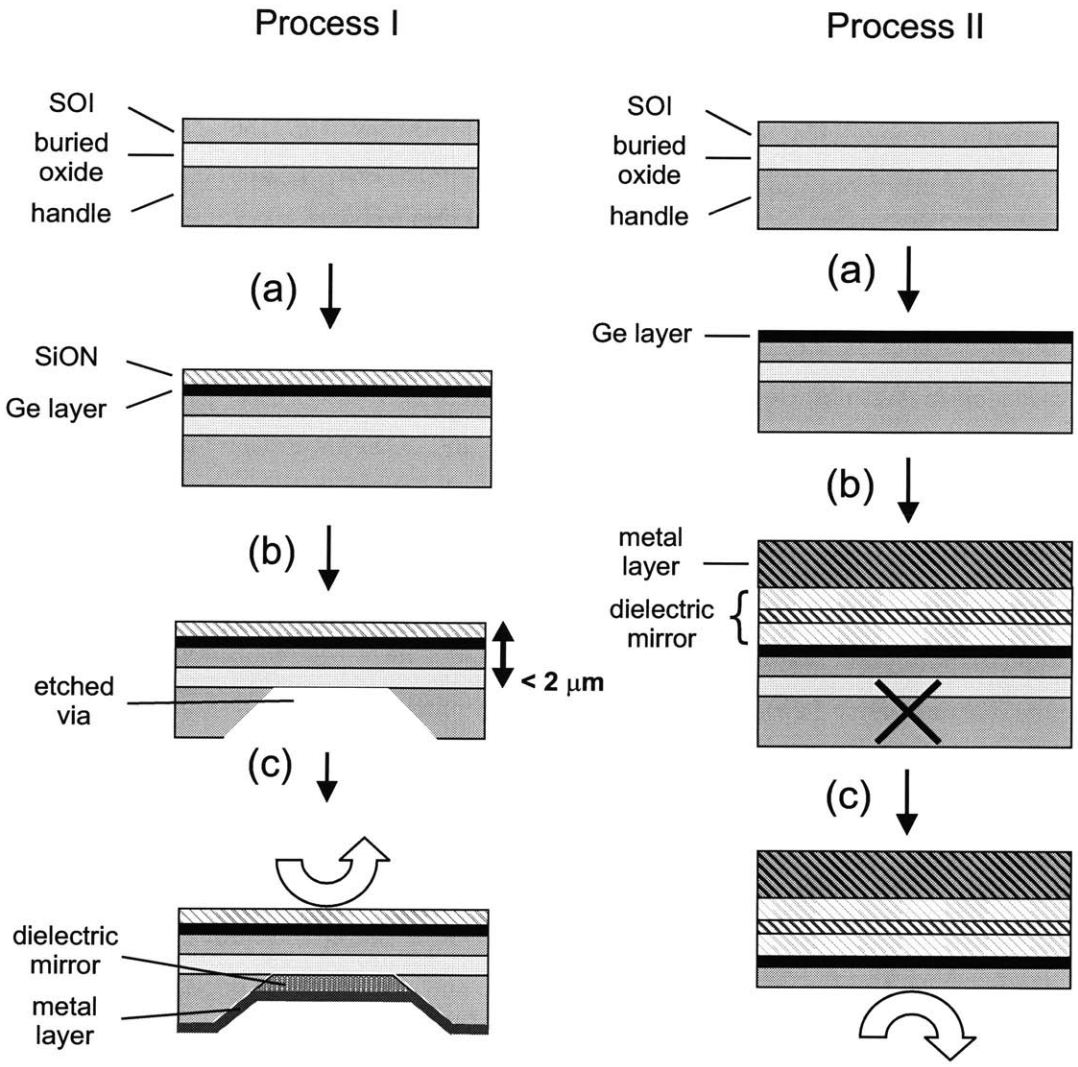

Figure 5-7: New fabrication processes facilitating the fabrication of SiGe-SBRs.

wavelengths absorbers with much larger modulation depth than the demonstrated 0.13% of our device are required to mode-lock fiber- and waveguide lasers. The fast recovery time, letting the SBR act as an artificial fast saturable absorber, may lead to interesting dynamics. Furthermore, a full characterization of the saturation behavior and a study of the recovery dynamics would be intriguing. Similar devices at shorter wavelengths will find applications in Cr:Forsterite and Ti:sapphire lasers at 1200 nm and 800 nm, used in optical metrology [154, 123] and for laser synchronization [155, 156]. These lasers would benefit greatly from the broad bandwidth of the SiGe-SBR, facilitating the operation of these highly complex systems. Since the absorption of germanium increases at shorter wavelengths, even higher saturable loss can be expected from a device with a structure similar to that of Fig. 5-5a, whose layer thicknesses are adjusted to the new center wavelength. With Si_xGe_{1-x} compound materials the bandgap of the absorber layer can be fine-tuned to allow for control of the absorption and of the saturation fluence. To meet the demand for a variety of absorber structures with germanium layers of different thickness and with a variety of reflectors, a simple and reliable fabrication process is desirable. The current process for fabrication of the Si-SiO_2 reflector (section 5.1.2), involving a wafer-bonding and substrate removal step, does not meet the reliability criterion, at least not in a university fabrication environment. In particular, wafer bonding proved to be a continuous challenge leading to occasional failure of the fabricated device. Therefore, two alternative fabrication processes are currently investigated (Fig. 5-7).

Process I is similar to the fabrication scheme presented for Si-SiO_2 reflectors in [144]: An SOI-wafer serves as the substrate for growth of the germanium absorber layer. Its thickness can be adjusted via thermal oxidation and etching or via deposition of additional silicon prior to Ge-deposition. First, the germanium absorber layer is deposited, followed by the growth of a protective SiON layer [step (a)]. This layer both acts as the top layer in the finished SiGe-SBR and protects the Ge-layer during subsequent etching. Then, vias are etched through the handle wafer via wet etching or deep reactive ion etching (D-RIE) [step (b)]. The buried oxide (BOX) of the SOI-wafer may serve as an etch stop layer. Alternatively, the BOX can be removed with hydro-fluoric acid (HF), which offers a 1:1000 etch selectivity at the Si:SiO_2 interface. Finally, a dielectric-metallic Bragg

reflector, *e.g.* similar to the one used in [166], is deposited in the via from the back of the wafer [step (c)]. The metal layer fulfills a triple functionality. Its acts as a heat spreader distributing energy deposited within the via opening, it contributes to a high and broadband reflectivity of the reflector, similar to [138], and it provides mechanical stability for the thin membrane. First fabrication runs revealed that mechanical stability of the membrane, exposed after fabrication step (b), and less than 2 μm thin, is a serious challenge to this process. Bowing of the membrane was observed, leading to a highly nonuniform reflection off the thin exposed layer.

To avoid degradation of the macroscopic surface quality, fabrication process II (Fig. 5-7) is designed to avoid the exposure of a thin membrane. First, the Ge absorber layer is deposited on an SOI-wafer [step (a)], followed by the dielectric-metallic reflector [step (b)]. The metal layer is reinforced via electroplated metal to yield a stability that allows it to serve as the new substrate [166]. Finally, the original substrate is removed, either entirely (as shown in Fig. 5-7) or in the area of vias. As a result, the SOI-layer and the Ge-layer form an absorber structure, on top of a dielectric-metallic Bragg mirror that is readily tailored to the specific laser wavelength. Research on both the properties of SiGe-SBRs and on simplified fabrication processes is in progress. Promising results are expected.

In summary, in this Chapter we have presented a CMOS-compatible process for the fabrication of highly reflecting Si-SiO_2 reflectors with 99.8% peak reflectance and an unprecedented bandwidth of 700 nm. A silicon-germanium saturable absorber was fabricated, based on these reflectors. Its wide optical bandwidth, ultrafast recovery dynamics and inverse saturable loss at high fluences point to interesting applications in femtosecond mode-locked lasers. The devices are fabricated in a materials system that is compatible with the gain medium anticipated for compact mode-locked lasers, paving the way to monolithic integration of both elements.

Chapter 6

Mode-locked bulk Er-Yb:glass laser

Erbium-doped fiber amplifiers (EDFAs) [167] have revolutionized optical communication systems. They constitute low-noise, broadband gain stages that allow for simultaneous amplification of signals across all channels, permitting the construction of long transmission spans without a single conversion of signals back to the electronic domain (section 1.1.2). The discovery of Er-doped fiber amplifiers has spurred research on Er-doped lasers for next generation communications systems (section 1.1), promising the emission of chirp-free pulse trains at highest repetition rates [39, 168, 40], of pulse trains with low timing jitter [36, 169, 61] and systems whose amplitude noise can be reduced via active feedback stabilization [105, 107]. Apart from optical communications, the emission in the eye-safe spectral region around 1.5 μm makes Er:glass lasers attractive for measurement and ranging applications. Finally, the low timing jitter, resulting from a long upper state lifetime, renders them interesting as sources for optical analog-to-digital conversion (section 1.3) and for the transmission of timing signals via optical fibers [36].

Since their first operation in the pulsed regime in 1965 [170], Er-doped glass lasers have been built in a variety of configurations. The Er:glass microchip laser, proposed in section 1.4.1 as a future laser source at high repetition rates, has first been demonstrated by Laporta *et al.* as a cw laser with a 200 μm long gain medium and a high slope efficiency of 22% [171]. Combined with a semiconductor saturable absorber, Q-switched operation of an Er:glass laser, emitting pulses as short as 1.2 ns with up to 100 kHz repetition

rate, could be demonstrated [172]. While the long upper state lifetime of Er-doped glass[1] and the short cavity round-trip time have prevented cw mode-locked operation of an Er-doped microchip laser to date (section 2.4), prior results obtained with cw and Q-switched Er:glass lasers indicate the feasibility of a mode-locked microchip laser made of the same gain medium, once active feedback stabilization is employed (Chapters 2-4). In contrast, mode-locked Er:glass lasers at high repetition rates of up to 50 GHz have already been demonstrated, but only in lasers built on discrete cavities that permit an adjustment of the mode size on the SBR in order to control the amount of inverse saturable loss for stabilization (section 2.7) [39, 168, 40]. Their integration in monolithic laser cavities, a prerequisite for wide commercial deployment, fully depends on the use of the active stabilization techniques of Chapters 2-4 and on silicon-germanium saturable absorbers compatible with the glass employed as the gain medium (Chapter 5).

To serve as multi-wavelength sources capable of providing light to all channels in the communications system (section 1.1.3) the spectrum of a mode-locked Er:glass laser needs to cover the entire C-band, requiring pulse durations shorter than 250 fs. Prior to our work, the shortest duration pulses were extracted from an Er:glass laser with 380 fs pulse duration and 6.8 nm full-width half-maximum (FWHM) spectral width [174], mode-locked via Kerr-lens mode-locking [92]. The compact high repetition rate lasers envisioned in this thesis, rely exclusively on the use of saturable Bragg reflectors for pulse formation. In such a system, the shortest pulse obtained in an Er:glass laser prior to our work showed an autocorrelation FWHM of 2.5 ps and a spectral width of 1.3 nm [175], more than an order of magnitude below the desired value. In this Chapter we demonstrate the bulk Erbium-Ytterbium:glass (Er-Yb:glass) laser with the shortest pulse duration (220 fs) and the broadest optical spectrum (11.2 nm FWHM) to date. Our laser spans the C-band of optical communications on a ± 10 dB level. Mode-locked only with a silicon-germanium saturable absorber it reveals the potential of mode-locked Er:glass lasers for WDM optical communication systems.

[1] $\tau_{Er} \approx 8$ ms [173].

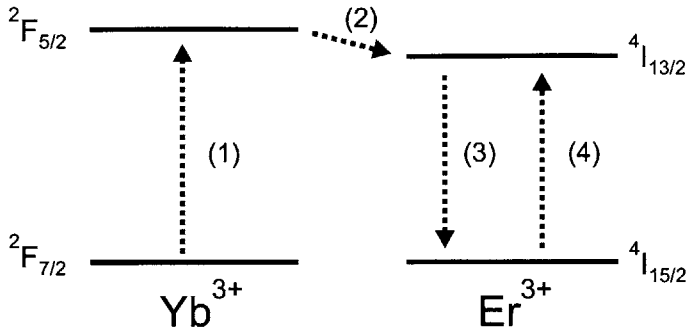

Figure 6-1: Significantly simplified energy-level diagram of the Er-Yb co-doped laser glass.

6.1 Characteristics of the gain medium Er-Yb:glass

Erbium-doped glass can be conveniently pumped with InGaAs semiconductor laser diodes at 980 nm, delivering up to 500 mW in their commercial versions and up to 1.8 W in the laboratory [176]. However, pump absorption in pure Er-doped glass rarely exceeds $\approx$ 50 dB/m due to cluster formation of Er-ions at higher doping concentrations. To enable short, bulk laser glasses, *e.g.*, to enable gain media of 200 μm length used in the microchip laser of [171], Erbium is co-doped with Ytterbium (Yb) of roughly twice the Erbium concentration. The Ytterbium acts as a sensitizer facilitating pump absorption, and reducing the absorption length to a few millimeters. The Er-Yb:glass used in the experiment of this Chapter was a phosphate glass (Kigre, Inc. type QX-Er) co-doped with 2.3×10^{20} Er-ions/cm^3 and 2.1×10^{21} Yb-ions/cm^3. Lower doping concentrations were tested as well, but did not yield the desired slope efficiency and pump absorption. When Ytterbium is engaged as a sensitizer, the absorption bandwidth shrinks to a few nanometers around 977 nm, requiring the pump diodes to be either temperature stabilized or stabilized with a fiber Bragg grating to match the peak absorption wavelength. The co-doped Er-Yb:glass constitutes a three-level system whose simplified level structure is depicted in Fig. 6-1. This diagram was created via incorporation of the simplifications and approximations for the pumping and lasing process of the Er-Yb:glass laser detailed in [173]. Under those assumptions the laser operates as follows: Pump light at 980 nm excites Yb-ions from the ground state Yb($^2F_{7/2}$) to the Yb($^2F_{5/2}$) state [process (1)]. A fast energy transfer from the upper Yb-level to the level Er($^4I_{13/2}$) populates the upper

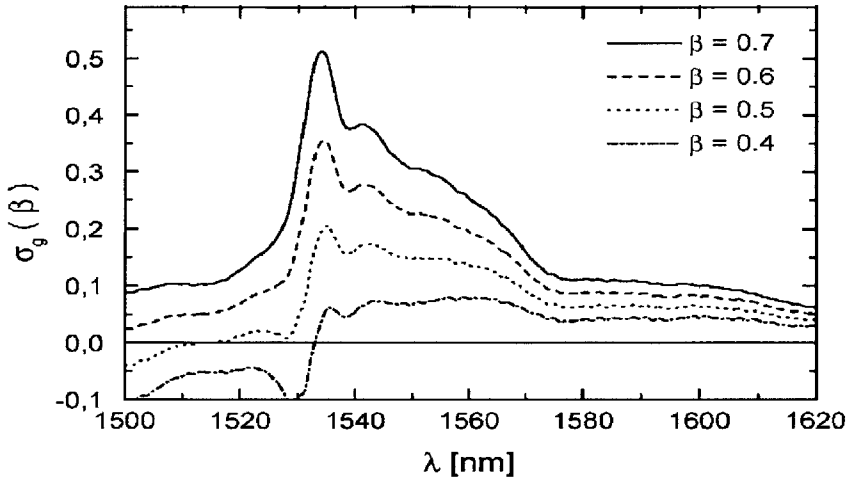

Figure 6-2: Effective gain cross section σ_g of phosphate glass QX-Er for different inversion levels β [3].

laser level [process (2)]. From here, spontaneous emission with the upper state lifetime $\tau_L \approx 8$ ms and stimulated emission occur [process (3)]. However, since the ground state of the Er-ions $Er(^4I_{15/2})$ is populated at room temperature, Er-doped glass acts as a three-level system and re-absorption [process (4)] can occur. Transparency of the gain medium is reached, when the emission exceeds the re-absorption.

The emission and absorption processes exhibit a different wavelength dependence [3]. As a result, the net gain spectrum varies with the interplay of emission and re-absorption in the laser [3, 173, 177]. Figure 6-2 shows the net gain cross section σ_g, representing the net gain spectrum of the Er-Yb:glass laser, as a function of inversion level $\beta = N_{2E}/N_E$, the ratio of Er-ions in the upper laser level N_{2E} to the total number or Er-ions N_E. For strong inversion, at $\beta \approx 0.7$, emission occurs predominantly at shorter wavelengths with a characteristic emission peak at 1534 nm. As the inversion decreases, a red shift in the emission becomes apparent, leading eventually to a relatively flat emission spectrum between 1530 nm and 1560 nm, the wavelength region corresponding to the C-band of optical communications. To generate short pulses from a mode-locked Er-Yb:glass laser, a flat and broadband gain spectrum is required, achievable only at low inversion. The

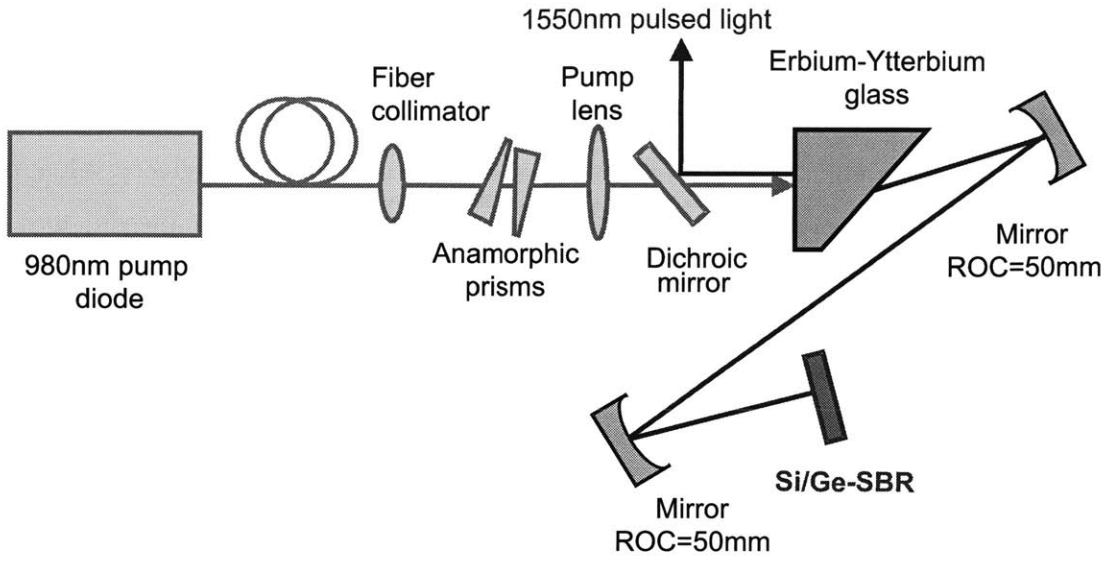

Figure 6-3: Schematic of the Er-Yb:glass laser cavity.

inversion of the gain medium is predominantly determined by the losses in the laser cavity [177]. We confirmed this finding of Taccheo *et. al.* recently by simulating the inversion characteristics of an Er-Yb:glass microchip laser [178] with the analytic model derived in [173]. Our simulation results indicate that the shape of the gain spectrum almost exclusively depends on the intracavity losses, whereas pump power and pump spot size do not critically affect the inversion level, as long as they are kept within reasonable proximity to the optimum. Following these theoretical results, careful optimization of the laser cavity and the use of our low-loss silicon-germanium saturable absorbers (section 5) have allowed us to build a low-loss Er-Yb:glass laser, whose wide optical bandwidth is attributed to the broad gain spectrum reached via low inversion.

6.2 Laser setup

A schematic of the mode-locked Er-Yb:glass laser is depicted in Fig. 6-3. The phosphate glass Kigre QX/Er co-doped with 2.3×10^{20} Er-ions/cm^3 and 2.1×10^{21} Yb-ions/cm^3 serves as the gain medium in the laser. It is flat-Brewster polished, placed at one end of the four-element laser cavity, and its flat side serves as an output coupler with 99.8%

reflectivity for the laser light and < 5% reflectivity at the pump wavelength. The laser is pumped with a 450 mW fiber-coupled laser diode, stabilized to 977 nm via temperature tuning (Bookham, type G07). While all pump light is absorbed for low pump power, at the operating point of the laser approximately 80% is absorbed, a reduced value to to bleaching of the absorption. The Gaussian waist of the laser mode inside the gain medium is calculated with the ABCD-matrix formalism [121] to be 30 × 45 μm, elliptic due to the Brewster interface. To match the size of the pump beam inside the gain medium with the ellipticity of the laser mode, and thus to ensure optimum overlap of pump mode and laser mode, the collimated pump light, a TEM_{00} mode, passes an anamorphic prism pair which creates the desired ellipticity of about 1:1.5. However, the anamorphic prism pair also introduces a slight astigmatism, separating the foci in the sagittal and tangential plane by about 0.5...1.0 mm. Further experiments, whose outcome is not included in the results section of this Chapter, have revealed that even better laser performance can be obtained when the ellipticity of the pump beam is generated with a pair of cylindrical lenses, eliminating the astigmatism. The pump light is focused with a 100 mm lens into the gain medium. A dichroic mirror between the focusing lens and the laser glass separates the laser output from the pump beam. The laser cavity itself is set up at 169 MHz repetition rate with two 50 mm mirrors focusing the laser mode in gain medium and on the saturable absorber.

6.3 Experimental results

With 360 mW of absorbed pump power an intracavity power of 8.7 W, corresponding to a pulse energy of 51 nJ, is obtained. To maximize power and reduce losses, *e.g.* via re-absorption in the gain medium, different path lengths in the Er-Yb:glass were tested by translating the flat-Brewster cut glass perpendicular to the optical axis. An optimum value was found at a path length of 2.0 mm, which will be the value of choice for future microchip lasers based on the same glass composition. Unlike Cr^{4+}:YAG laser crystals, well known for clustering of the dopant, the Er-Yb:glass was observed to be very homogeneous, such that the laser could be operated equally well across the entire sample.

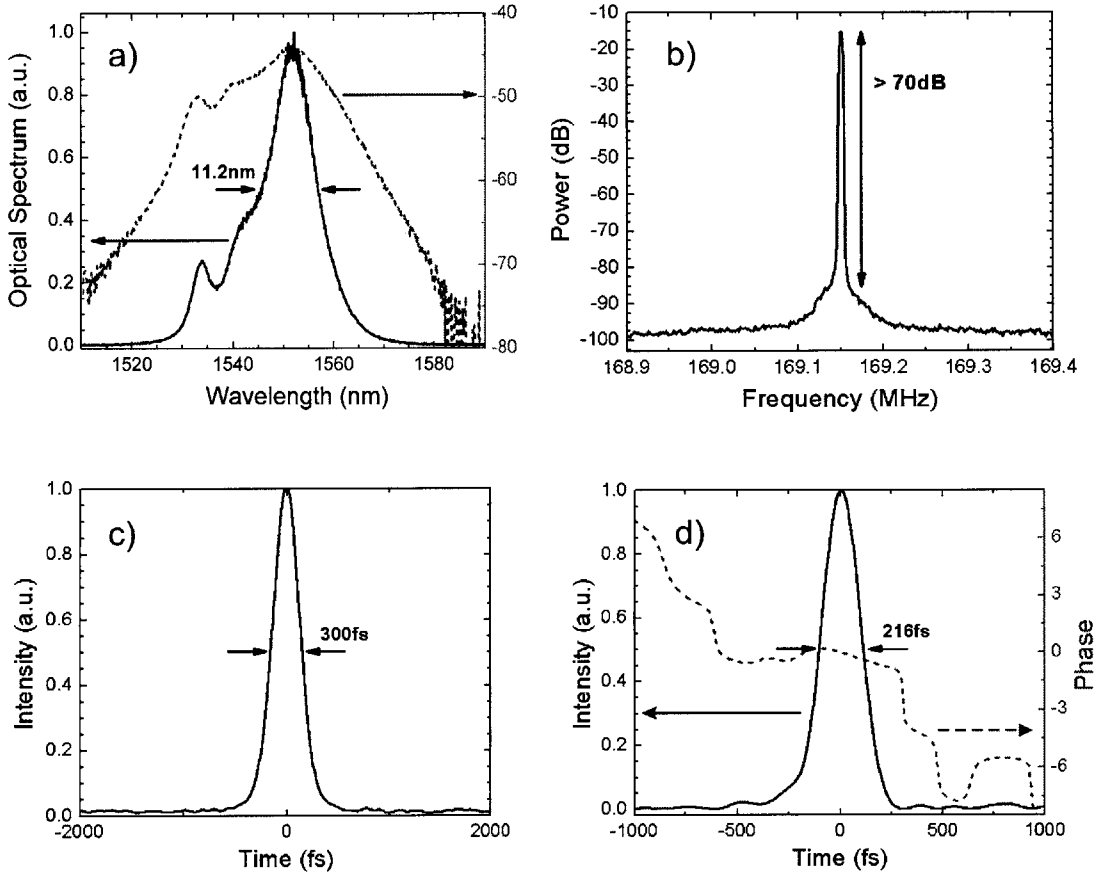

Figure 6-4: Characteristics of the Er-Yb:glass laser. **a)** Optical spectrum on linear and logarithmic scale. **b)** Microwave spectrum. **c)** Autocorrelation. **d)** Pulse intensity and phase retrieved with the Picaso algorithm.

Losses in the laser were reduced to a bare minimum by use of a low output coupling of 0.2% at the flat surface of the laser glass, via mirrors with $\approx 99.95\%$ reflectance and with the low-loss silicon-germanium saturable absorber exhibiting a nonsaturable loss of about 0.17% (Chapter 5). The minimization of intracavity losses results in a highly-saturated gain with low inversion, leading to a flat gain profile to support a broad optical spectrum. We obtain an optical spectrum centered at 1550 nm with a FWHM bandwidth of 11.2 nm. It covers the entire C-band of optical communications at approximately ± 10 dB level (Fig. 6-4a). Due to positive dispersion contributed by the Er-Yb:glass the pulses leaving the laser are chirped. After dechirping them extracavity with 1.0 m of single mode fiber (Corning SMF-28), an autocorrelation with 300 fs FWHM is measured with a commercial autocorrelator (APE model 'Pulsecheck'), leading to an inferred pulse duration of 212 fs (Fig. 6-4c). Phase retrieval with the Picaso algorithm [179] reveals a pulse width of 220 fs (Fig. 6-4d), which is 10% larger than the transform-limited value, obtained from the zero-phase Fourier transform of the power spectrum. The algorithm, matching pulse shape and phase to the measured autocorrelation and optical spectrum, indicates an almost flat phase across the pulse, indicating that the pulse was fully dechirped by the 1.0 m of single-mode fiber prior to autocorrelation measurement. To our knowledge, these are the shortest pulses generated from a bulk Er-Yb:glass laser to date, compared to 380 fs from a Kerr-lens mode-locked Er-Yb:glass laser [174] and a 2.5 ps pulse duration obtained solely from mode-locking of an Er-Yb:glass laser with an SBR [175]. To ascertain that the SiGe-SBR is solely responsible for mode-locking, a negative test with a sample similar to the SiGe-SBR was conducted: One of the Si-SiO_2 reflectors of Chapter 5 was completed with a silicon top layer whose optical thickness matched that of the structure terminating the SiGe-SBR. With the Si-SiO_2 high reflector twice the intracavity power, compared to the SiGe-SBR, could be achieved. Pulse formation was observed at none of the points in the stability diagram tested, neither self-starting nor induced by shaking of a cavity end-mirror. This observation lead us to the conclusion that the SiGe-SBR was the only mode-locking mechanism.

The laser operates at 169 MHz repetition rate with a clean RF spectrum and a noise floor more than 70 dB below the signal level (Fig. 6-4b). No Q-switching behavior was

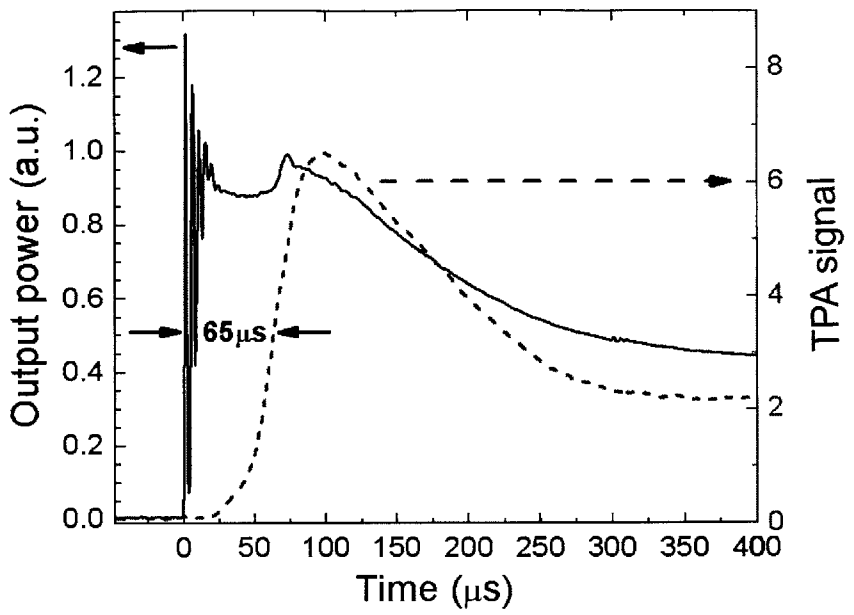

Figure 6-5: Characterization of the mode-locking buildup time, the time lag of the second harmonic intensity vs. output power after removal of an intracavity beam-block.

observed regardless of pump power level despite the long upper-state lifetime and the small emission cross section of the gain medium. We attribute the high stability against Q-switching to the onset of inverse saturable absorption in the SiGe-SBR at high fluence (Fig. 5-5c). A complete analysis of the mode-locking dynamics with the SiGe-SBRs is the object of future research. Possible questions to address are a complete characterization and modelling of the temporal dynamics of saturation, recovery and inverse saturable loss in the SiGe-SBR; a measurement of the saturation curve (similar to Fig. 2-1b) for pulses of different durations; and an analysis of the interplay between Er-Yb:glass laser and SiGe-SBR: Does the SiGe-SBR in fact act as a *fast* semiconductor saturable absorber? If so, what pulse shaping capability does it possess? Does the absence of a slow recovery component constitute obstacles to the starting behavior of the mode-locking process? At which fluence is the optimum balance between pulse shaping and stabilization against Q-switching instabilities reached? The new generation of SiGe-SBRs with larger modulation depth (section 5.2.2) and a simplified fabrication process will help answer these questions.

Finally, we measured the mode-locking buildup time with the new SBR. For this

purpose, the collimated output beam was tightly focussed with a 10 mm lens on a silicon photodetector, detecting the two-photon absorption (TPA) signal that is generated only in the presence of high peak intensities, *i.e.* when the laser is mode-locked. At the same time, a small fraction of the output power was detected with a fast InGaAs photodetector to measure a signal proportional to the intracavity power, independent of the mode-locking state. An optical chopper inside the laser cavity periodically blocked and unblocked the laser, allowing to record and average the two signals, representing output power and TPA signal. As shown in Fig. 6-5, the latter lags the output power by the mode-locking buildup time of about 65 μs, corresponding to 11,000 round-trips. This value is similar to values in lasers mode-locked with SBRs in the III-V semiconductor materials system [180][2], showing that the SiGe-SBR shows a starting characteristic of mode-locking similar to that observed with conventional saturable absorbers. Apart from the value of the mode-locking buildup time, Fig. 6-5 allows interesting insights in the dynamics of the laser. After the intracavity beam block is removed, the intracavity power undergoes roughly five relaxation oscillations, indicating that the laser is very stable, and power fluctuations are highly damped. This observation corresponds well with the low noise floor in the microwave spectrum of the laser, which does not reveal any, not even suppressed, relaxation oscillations. Once mode-locking sets in at $t \approx 65\mu$s, the output power slightly increases. This is due to the reduction of round-trip loss, now reduced by the saturable loss, which is bleached by the individual pulses. Finally, after $\approx$ 150 μs the intracavity power drops by a factor of two, due to gain saturation. The strong delay in the onset of gain saturation and relaxation is caused by the long upper state lifetime of the Er-Yb:glass gain medium.

In summary, we have mode-locked an Er-Yb:glass laser with a silicon-germanium saturable absorber. Minimization of intracavity losses lead to a flat gain spectrum supporting the shortest pulse generated in a bulk Er-Yb:glass laser to date, spanning the C-band of optical communications on a logarithmic scale. This experiment shows that Er-Yb:glass laser mode-locked with the new SiGe-SBRs are capable of serving as multi-wavelength

[2]In [180] a mode-locking buildup time of 200 μs was observed in a 100 MHz Ti:sapphire laser, corresponding to 20,000 round trips.

laser sources that provide all channels of the communications system with a clean and stable pulse train.

Chapter 7

Conclusion

In this thesis, we have presented solutions to a variety of challenges on the way to compact, integrated mode-locked microchip and waveguide lasers.

In the field of laser dynamics, we have introduced a control systems perspective to the stability of saturable absorber mode-locked lasers. The control systems method unifies the existing approaches to laser stabilization and makes the plethora of tools in control systems engineering available to problems of laser stabilization. In particular, it identifies feedback control with an intracavity loss modulator as a universal stabilization scheme, applicable without restrictions to solid-state lasers at high repetition rates. In laboratory experiments we have validated this concept and shown that a laser which is unstable without feedback control can reach a noise performance on par with a passively stabilized laser, once the feedback controller is engaged. Furthermore we have shown, that the addition of feedback stabilization does not negatively affect the pulse shaping dynamics, since controller and mode-locking dynamics occur on vastly different timescales.

To enable the monolithic integration of semiconductor nonlinearity and gain medium, we have addressed the materials challenge of manufacturing a CMOS-compatible saturable absorber in the silicon - silicon dioxide - germanium materials system. We have fabricated a wafer-scale Si-SiO_2 high reflector with 99.8% peak reflectance and an unprecedented bandwidth of 700 nm in the near infrared. It serves as the substrate of a saturable Bragg reflector which employs for the first time a germanium layer to provide saturable loss. Pump-probe measurements reveal ultrafast recovery of the saturation, indicating

the operation of the saturable Bragg reflector as a fast saturable absorber in the laser. In the regime of high fluence strong inverse saturable loss, providing stabilization against Q-switching instabilities, is observed. The compatibility of the materials used in our device with the laser gain medium of compact mode-locked lasers paves the way to monolithic integration of both elements.

Finally, we have built an Erbium-Ytterbium:glass laser mode-locked solely with the silicon-germanium saturable Bragg reflector. The laser generates the shortest pulse and broadest optical spectrum obtained from a bulk Er-Yb:glass laser to date. Spanning the C-band of optical communications on a ± 10 dB level, it demonstrates that mode-locked Er-Yb:glass lasers can serve as multi-wavelength laser sources in next-generation optical communications systems, providing all channels across the communications spectrum with a stable train of pulses.

In summary, this thesis has provided the essential components enabling the construction of actively stabilized, monolithically integrated and C-band spanning mode-locked Erbium-Ytterbium:glass high repetition rate lasers in the future.

Appendix A

Feedback control electronics

For the stabilization experiments of chapters 3 and 4 a number of feedback control circuits were designed. They were developed with use in future laser systems at repetition rates in the multi-GHz range in mind. Special attention was given to low noise, high gain, wide bandwidth and low group delay. The latter poses the most significant challenge to a system operating on only 90 deg phase margin (chapter 3): A 10 ns delay, the target value for development of the control circuit, already limits the effective bandwidth to only 25 MHz. To prevent additional phase lag from bandwidth limitations in the individual building blocks, a 3 dB bandwidth of over 100 MHz was targeted for all components of the circuit. Fig. A-1 shows the block diagram of the overall control circuit: A high gain, low noise transimpedance amplifier (TIA) converts the photodiode current into the control

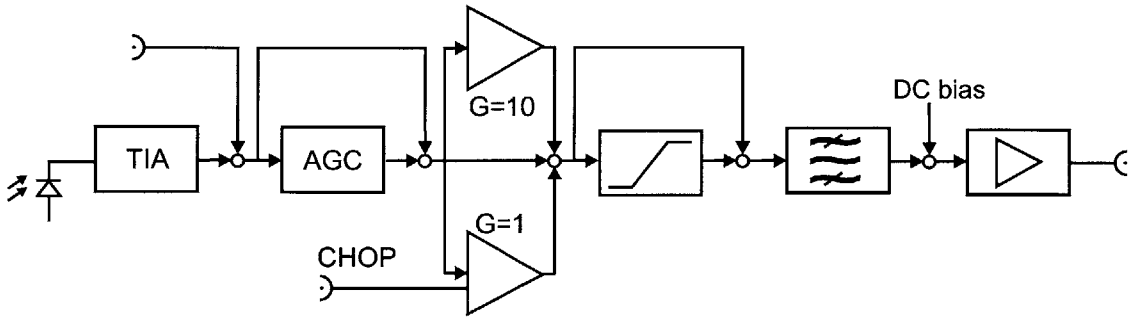

Figure A-1: Blockdiagram of the feedback control electronics. Abbreviations: TIA transimpedance amplifier, AGC automatic gain control, CHOP input of the electronic chopper.

Table A.1: Group delay of electronic components

component	group delay
Transimpedance amplifier (OPA657 + 4.7k)	3 ns
Automatic gain control (AD835)	1.5 ns
Amplifier (G=1) and chopper (OPA690)	2 ns
Amplifier (G=10) (OPA657)	2 ns
Limiter (AD8036, AD8037)	1.5 ns
Laser diode driver	3 ns

signal, which is then attenuated or amplified in the automatic gain control circuit (AGC), further amplified or chopped (CHOP) electronically, clipped in a limiter, filtered in a bandpass filter and finally prepared by a suitable output stage onto the intracavity loss modulator. Each of the components can be bypassed to eliminate the group delay of the respective component. For example, in most applications either the AGC or the limiter will be used, but not both. For test purposes it is helpful to drive the circuit with an electronic signal rather than optically, allowing for measurements with a network analyzer. The AGC allows to keep the system stable from threshold to its operating point, while the limiter protects the output stage if the controller is employed for the transition from unstable to stable operation, such that the circuit is active during Q-switched operation. Each building block, as well as the combined circuit, was built and then measured with a network analyzer to accurately determine the actual propagation delays and bandwidth limitations. While simulations and data sheets offer good first estimates, the interaction of printed circuit board (PCB) layout with the electronic components made this process indispensable for a reliable circuit design. Table A.1 lists the components discussed in this section and their measured group delay. It shows that a feedback controller with a total of 10 ns group delay can be built with standard components, though each stage of the circuit needs careful optimization.

A.1 Transimpedance amplifier

The circuit of the transimpedance amplifier (TIA) is sketched in Fig. A-2a. A fast 120 μm photodiode with 1 pF capacitance and 0.3 ns rise time (model OSI Fibercomm FCI-InGaAs-120) provides the current. FET-input OPAMPs (OPA655, OPA657) with large gain bandwidth products and low input capacitances were used in the TIA. The construction of a high gain, high bandwidth TIA is challenging when low noise is required in addition. The transimpedance resistor R_F sets the gain and, combined with the feedback capacitor C_F determines the bandwidth $f_{max} = 1/2\pi R_F C_F$. Resistors around 4.7 kΩ and capacitances of C_F=0.5 pF were chosen, resulting in a bandwidth of about 100 MHz with the OPA657 (Fig. A-2c). With the choice of R_F and C_F the noise gain of the TIA is determined as well: The capacitance of photodiode and OPAMP form a zero at the inverting node. Consequently, above $f_{noise} = 1/2\pi R_F(C_D + C_{comm} + C_{diff})$ the noise gain increases from the DC-value of unity by 20 dB / decade (Fig. A-2b). To reduce the overall noise once the bandwidth f_{max} is fixed, the sum of diode capacitance, common mode input and differential input capacitance must be reduced to a minimum. With the selected components this pole is located at about 10 MHz, as shown in the measured RF spectrum of the TIA output (Fig. A-2e). The most suitable feedback resistor was found in a series of measurements of the TIA transfer function with a network analyzer: Cw light from a tunable laser source at 1540 nm was modulated with the 10 GHz LiNb modulator, used for experiments in chapter 4. The modulator was driven with the signal generated in the network analyzer. First, the signal was recorded on a fast, 2 GHz photodetector with $<$ 0.2 ns rise time for calibration purposes (Eotech model ET-3000). This measurement served as the reference, allowing for propagation delays in the cables, the modulator and of the light to the photodetector. Then, the commercial 2 GHz photodetector was replaced by the combination of photodiode and TIA described above, and its transfer function was recorded. Figure A-2c and A-2d show the measured amplitude and phase characteristics for different feedback resistors. The gain of about 20 dB results from the difference in transimpedance values. The signal of the non-amplified 2 GHz detector was measured on a 50 Ω resistor, while the TIA employs a resistance two orders of magnitude above this

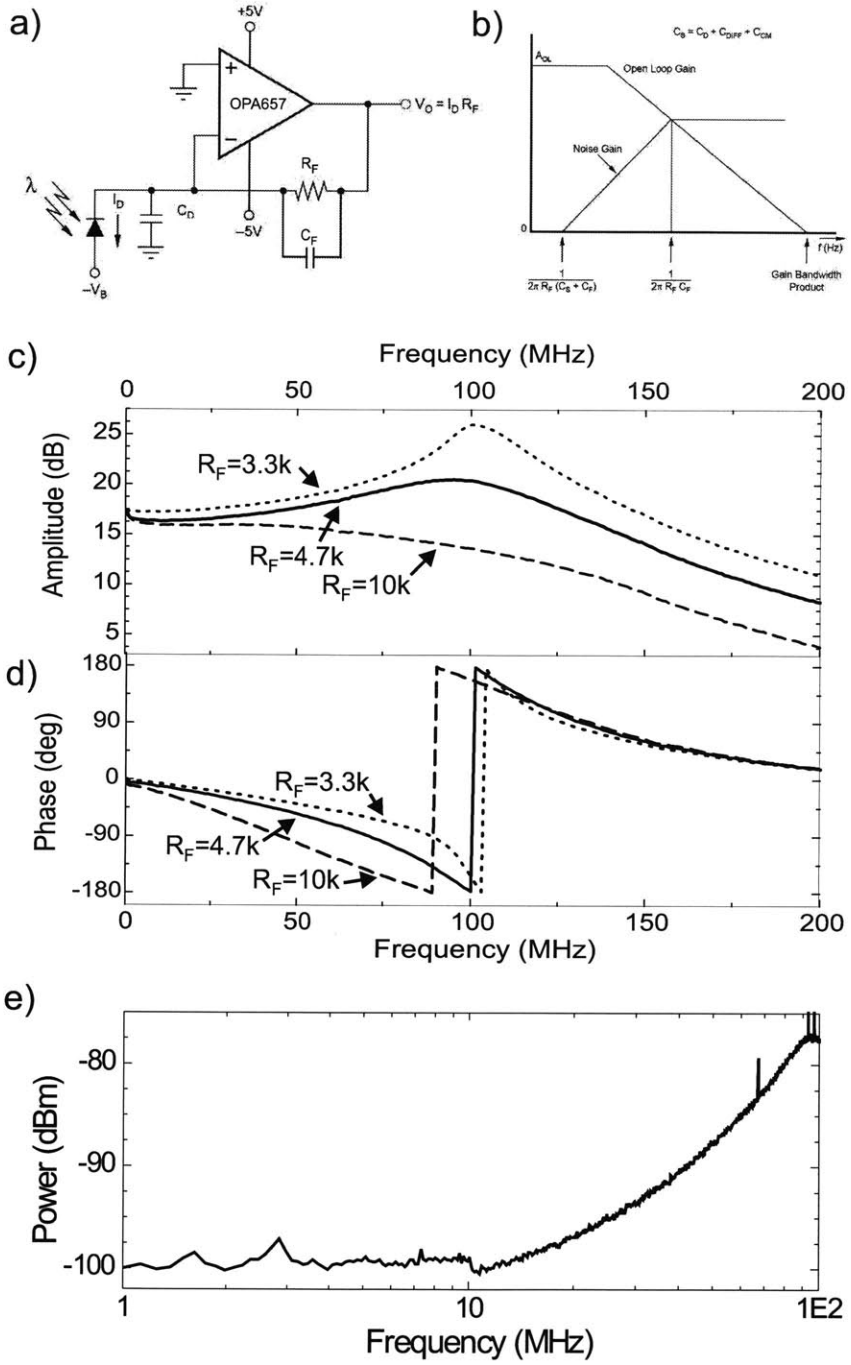

Figure A-2: **a)** Circuit diagram of the transimpedance amplifier (TIA). **b)** Noise and open loop gain of the circuit. **c)** and **d)** Measured transfer function of the TIA for different values of R_F: (c) amplitude and (d) phase. **e)** RF spectrum of the TIA without further amplification.

value, resulting in a gain difference of approximately 20 dB. This accurate measurement of the transfer function allowed to find the optimum value for R_F, once $C_D = 0.5$ pF was set. Resistors smaller than ≈ 3 kΩ lead to oscillations, while $R_F = 3.3$ kΩ still leads to strong peaking at the corne frequency of the TIA at about 100 MHz (Fig. A-2c). In contrast, a relatively flat TIA response was measured for $R_F = 4.7$ kΩ, the value selected for use in the circuit, while higher resistors severely compromise the bandwidth. Figure A-2d) shows the phase lag introduced by the TIA. For frequencies below 50 MHz the phase of the TIA with $R_F = 4.7$ kΩ is due to the total propagation delay of 3 ns in photodiode and TIA, while additional phase is accumulated for higher frequencies due to roll-off in the low-pass filter. Figure A-2e shows the noise of the TIA. It is flat up to $\approx$ 10 MHz and then increases by 20 dB / decade. Low-pass filters in the circuit, *e.g.* simple RC- or LC-filters, allow to reduce the noise gain between 10 MHz and 100 MHz. In summary, a transimpedance amplifier with 100 MHz bandwidth, 3 ns group delay and low noise gain has been built.

A.2 Automatic gain control

To allow for stabilization over the entire parameter range of the laser, mode-locked with a saturable absorber, an automatic gain control (AGC) was developed. It permits the control signal to provide constant negative feedback while the output power of the laser is ramped from threshold to its operating point, as discussed in section 3.1: The control signal applied to the intracavity loss modulator, stabilizing the laser via negative feedback, is proportional to the output power of the laser, similar to the feedback provided by gain saturation (matrix element A_{11} in Fig. 2-7a). As a result, the negative feedback of the active controller increases linearly as the laser is ramped up, while the destabilizing positive feedback of the saturable absorber (matrix element A_{22} in Fig. 2-7a) follows a highly nonlinear dependence of pump parameter r. An ideal feedback controller would allow the feedback gain to follow exactly the destabilizing positive feedback A_{22}. More simple approximations of this function were implemented as analog circuits, described in the following two sections. The AGC needs a wide bandwidth and low group delay to

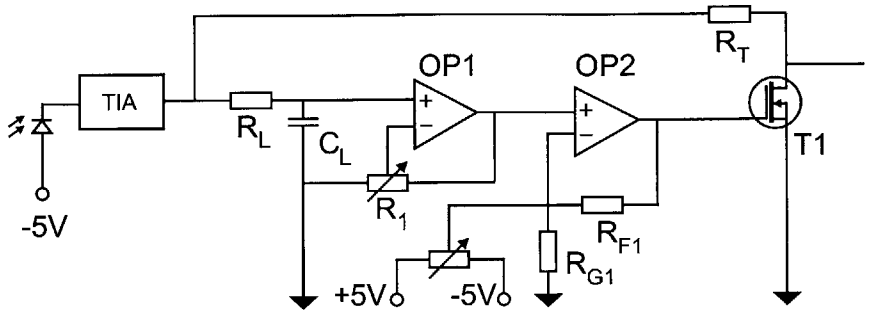

Figure A-3: Automatic gain control with field effect transistor (T1) as variable resistor.

permit broadband laser stabilization, and a large dynamic range over which the gain can be varied. The analog AGCs providing constant feedback consist of two major building blocks: (i) An attenuator in the signal path allows fast signals within the controller bandwidth to propagate undisturbed, while attenuating or amplifying the signal provided by the TIA. (ii) The gain of the AGC is determined in a slow bias circuit from the DC-level of the input signal, proportional to the laser output power.

A.2.1 Automatic gain control with field effect transistor

A simple AGC employed in the stabilization via AOM (chapter 3) is shown in Fig. A-3. The signal provided by the TIA is applied to a resistive voltage divider consisting of a fixed resistor R_T and the field effect transistor (FET) T_1 (model 2N2000) used in the linear region as a variable resistor [181]. By variation of the effective resistance of T_1 the signal level between drain and source of the FET can be varied by about 1.5 orders of magnitude, allowing for attenuation of the input signal as the output power of the laser is increased. The gate voltage of T_1 is determined by the remaining components of the circuit in Fig. A-3. The signal of the TIA is filtered in the RC low-pass consisting of R_L=3.3 kΩ and C_L=2.2 μF, with a corner frequency of 22 Hz. The DC-level of the input signal, which is very gradually ramped up as the laser is turned on, can pass this filter, while fast signal components, such as Q-switch oscillations and pulses at the laser repetition rate, are filtered out. This DC-level is then amplified in the slow amplifier OP1 (*e.g.* an OPA1177) with variable gain and combined with an offset voltage in OP2 (also an

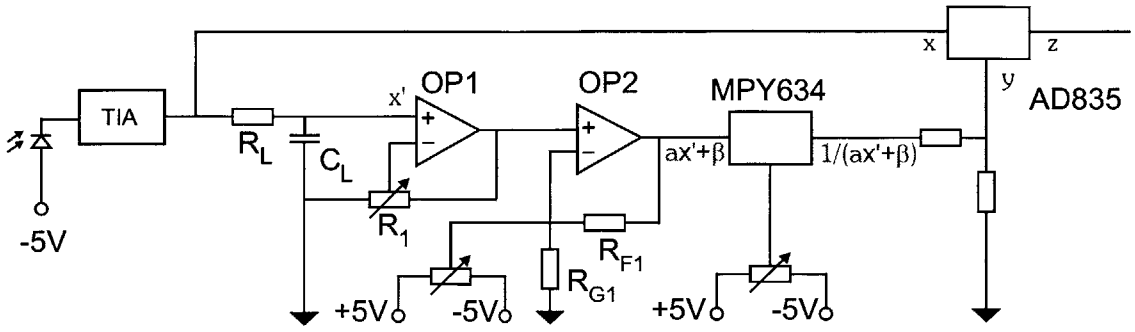

Figure A-4: Automatic gain control with four quadrant multiplier (AD835) as variable attenuator

OPA1177). The two amplifiers allow to set the slope and offset of the control signal applied to the variable resistor T_1. At different bias levels of the variable resistor T_1 a group delay of about 5 ns was measured in the signal path. This value was tolerable in the experiment with the AOM, where a propagation delay of 200 ns between transducer and the laser mode (section 3.1) limited the control bandwidth. However, control circuits applicable to future generations of microchip and waveguide lasers require sub-10 ns overall group delay (section A). In the following section an improved, fast AGC is discussed.

A.2.2 Automatic gain control with four quadrant multiplier

To avoid the bandwidth limitations mentioned above, the resistive divider R_T, T_1 in the circuit of Fig. A-3 was replaced by a 250 MHz four quadrant multiplier (AD835), used as a variable attenuator in the signal path (Fig. A-4). Its output follows the function $z = x \cdot y$, permitting to control the signal path $x \rightarrow z$ with the signal applied to y. Measurements with a network analyzer determined the small signal propagation delay between x and z to be about 1.5 ns, a factor-of-three improvement over the previous circuit. To keep z constant when x, the output of the TIA, rises upon ramp-up of the laser, this control input is set to $y = const/(\alpha x' + \beta)$ with the analog multiplier MPY634 (Fig. A-4): Again, the DC-level x' of the signal provided by the TIA is obtained via the RC filter R_L, C_L. Slope and offset are set with the resistor settings on OP1 and OP2, resulting in a signal $\alpha x' + \beta$ applied to the MPY634. The analog multiplier MPY634

is wired to invert its input, delivering an output signal $10V/(\alpha x + \beta)$. Its amplitude is divided in a 1:10 resistive divider and applied to set the gain of the fast four quadrant multiplier AD835. The latter assumes an output value of $z = x/(\alpha x' + \beta) \approx$. For the offset β is chosen as small as possible, just large enough to prevent the inverter MPY634 from saturating for the smallest input levels x'. Then, the circuit implements a provides a constant output level α for fast signal components.

A.3 Amplifier G=10 and G=1 with electronic chopping

To further amplify the signal of the TIA (Fig. A-1), an amplifier with G=10 based on an OPA657 with R_G=47 Ω and R_F=470 Ω is used. Alternatively, the control signal can be electronic chopped, by periodically opening and closing the control loop. This way, the transients between unstable and stabilized state of the laser (section 4.2) can be studied. A unity-gain amplifier based on an OPA690 offers enable (disable) functionality within 25 ns (200 ns), sufficiently fast for the study of the transitions.

A.4 Limiting amplifier

When the drive electronics in the output stage of the circuit controls sensitive devices that have to be protected against spikes, *e.g.* those resulting from a Q-switch cycle that accidentally passes through the circuit before the controller stabilizes the laser, a voltage limiter was added to the circuit. The AD8036 / AD8037 used at unity gain or gain G=2 proved ideal for this task. Equipped with a limiter at the voltage feedback input stage, they achieve 3 mV clamp accuracy with nanosecond overdrive recovery time, offer $>$ 200 MHz bandwidth and a group delay below 2 ns, as verified in measurements with a network analyzer. Since the clamp function applies to the input stage, the gain of the is stage was chosen as small as possible to preserve the clamp accuracy — if for example a gain of 5 were chosen, the clamp accuracy would drop to 15 mV. For the same reason, the limiter was placed as close to the output stage as possible, to prevent further amplification

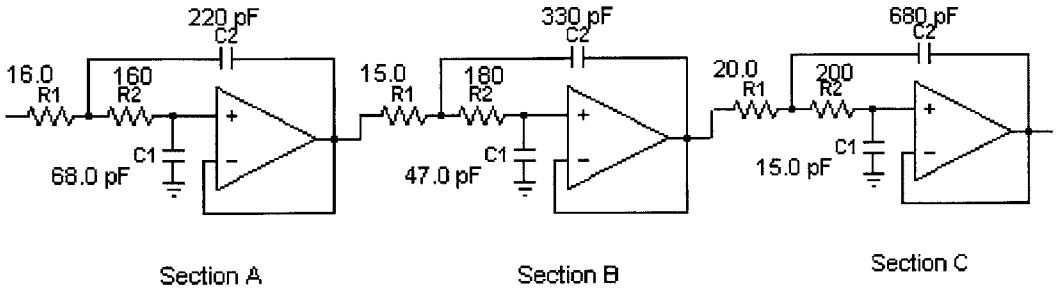

Figure A-5: Active low-pass filter (6^{th} order Butterworth with 25 MHz bandwidth)

of the signal after clamping. For high power laser diodes controlled in carrier injection experiments clamping is not critical, but low power diodes, *e.g.* 70 mW diodes at 780 nm, were successfully protected with the limiter.

A.5 Higher order low-pass filter

To prevent the feedback control electronics from interacting with the pulse formation on a round-trip timescale, signals at and above the laser repetition rate were suppressed with an active filter. To obtain a maximum effective control bandwidth, determined by filter roll-off and 90 deg phase point, a Butterworth filter of 6^{th} order was designed with the FilterPro^{TM} tool from Texas Instruments [127]. As discussed in section 4.1 the requirements on the filter were especially high in the lasers with repetition rates of 30 MHz ... 100 MHz used in the experiments of chapters 3 and 4 since filter roll-off and repetition rate differed by less than a factor of three. To meet this requirement, the filter shown in Fig. A-5 was implemented. However, the low impedance values required in the high frequency range posed a significant challenge: The output resistances of the OPAMPs used (mainly OPA655 and OPA657) came close to the smaller values used in the Sallen-key architecture of Fig. A-5. While filter could be implemented by careful adjustments of the resistor values, passive higher order low-pass filter of the PLP series from Minicircuits offer better performance at significantly less effort. They will be used in future experiments.

A.6 Laser diode driver

One possibility to control the intracavity losses in a mode-locked microchip laser might be with an optical loss modulator based on free carrier absorption, similar to the one discussed in [116], but with the modulating light source located apart from the saturable absorber device. One way to accomplish this, might be to use a short wavelength laser diode (*e.g.* an 800 nm laser diode) that optically injects free carriers in the absorber, and thus adds loss to the laser cavity as the current of this diode is increased. One of the challenges to this modulation scheme is the construction of fast laser diode driver capable of controlling a high current (*e.g.* 1 A) with the bandwidth calculated in section 2.6.

We accomplish this task with the following circuit. A fast, yet high current OPAMP (TI OPA2674) is operated as a current source in the configuration of Figure A-6a. The ground resistor R_G converts the OPAMP to a transresistance amplifier, converting input voltages to output currents. The diode to be controlled is added between the output of the OPAMP and R_G. With the OPA2674 we were able to source up to 400mA, when R_G = 1 Ωm and R_F = 240 Ωm. The corresponding transfer function is shown in Fig. A-6c and reveals a 3dB bandwidth of about 100 MHz and a propagation delay on the order of 3 ns. These values remained almost constant even when the output current swing was increased to 50mA peak-peak. To increase the possible drive current, four OPAMPs were connected in parallel, as shown in the diagram of Fig. A-6b. Now, an additional resistor $R_1 ... R_4$ is added to ensure stability and an equal current load in each of the OPAMPs. The laser diode to be controlled is added in series to R_G. This bears the disadvantage that an offset input voltage equalling the band gap of the diode must be added to the drive voltage and that the conversion from input voltage to output current in no longer linear, but follows the I-V-characteristic of the diode. However, for stabilization purposes, the laser diode is biased with a modest bias current, such that a sufficient slope exists. It can also be increased with a larger value of R_G. With four OPAMPs we measured the transfer function of Fig. A-6d, again with over 100 MHz small signal bandwidth and a maximum drive current of 1400 mA. These measurements show that the need for broadband loss control, identified in section 2.6 can be met with a simple drive circuit.

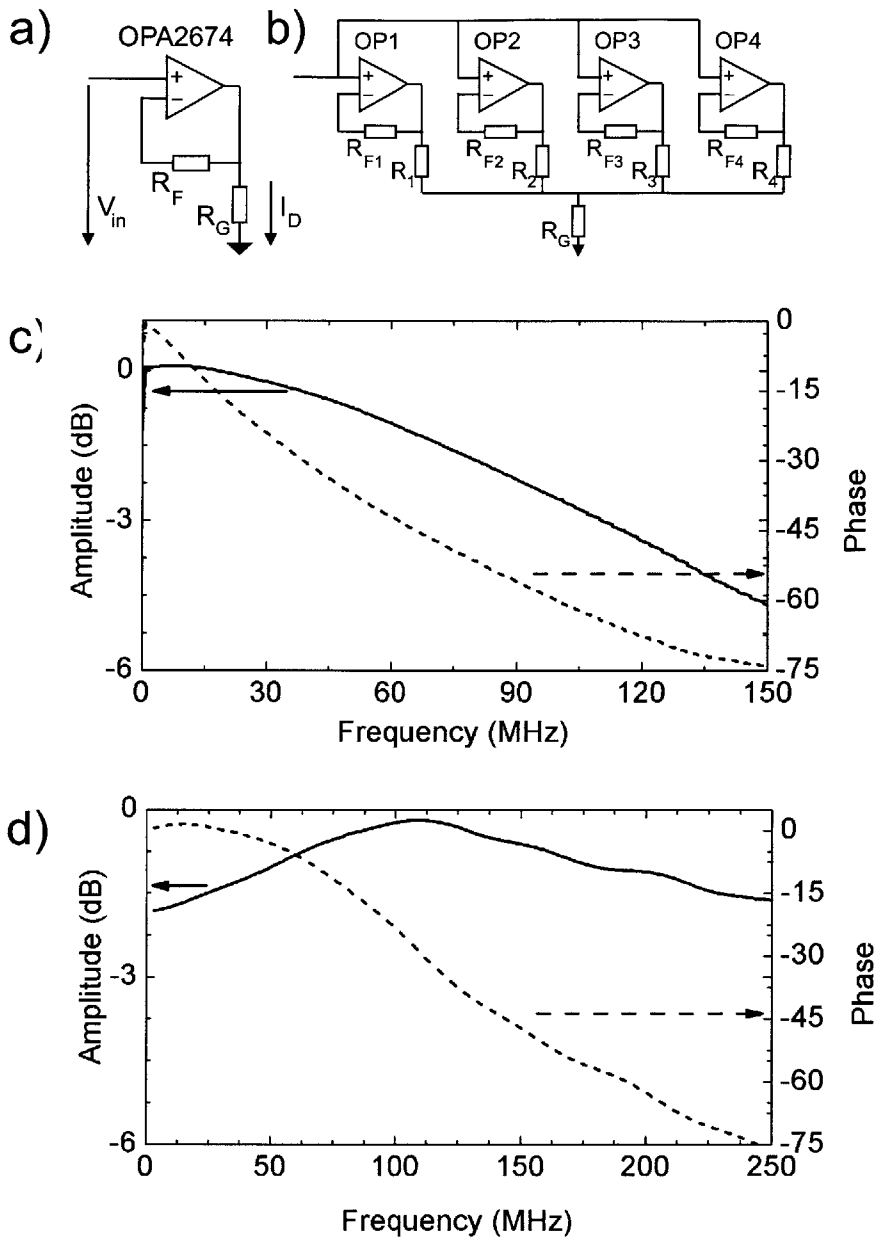

Figure A-6: **a)** Schematics of single OPAMP current source. **b)** Schematics of quad OPAMP current source. **c)** Measured transfer function of single OPAMP current source. **d)** Measured transfer function quad OPAMP current source. Data courtesy of Hyunil Byun.

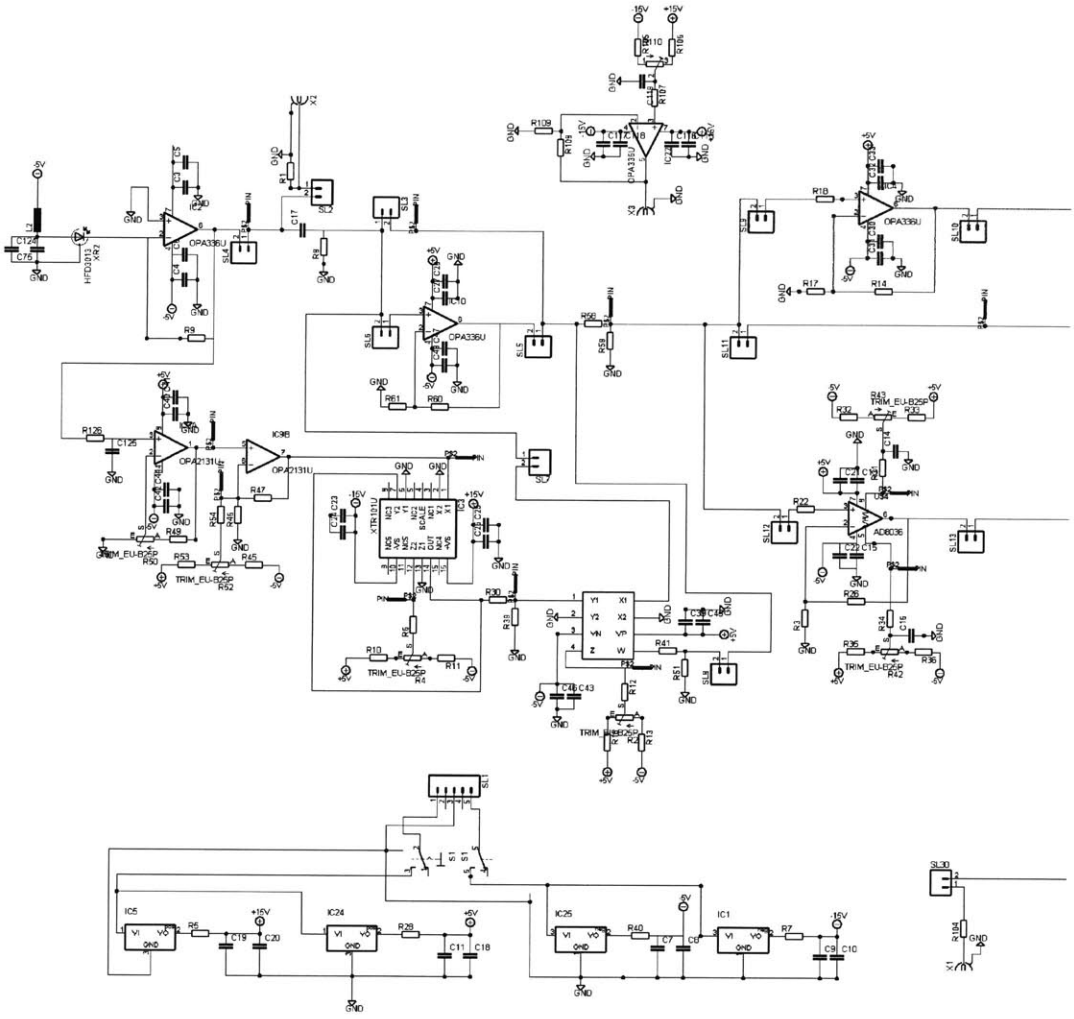

Figure A-7: Complete feedback control circuit: TIA, AGC, limiter.

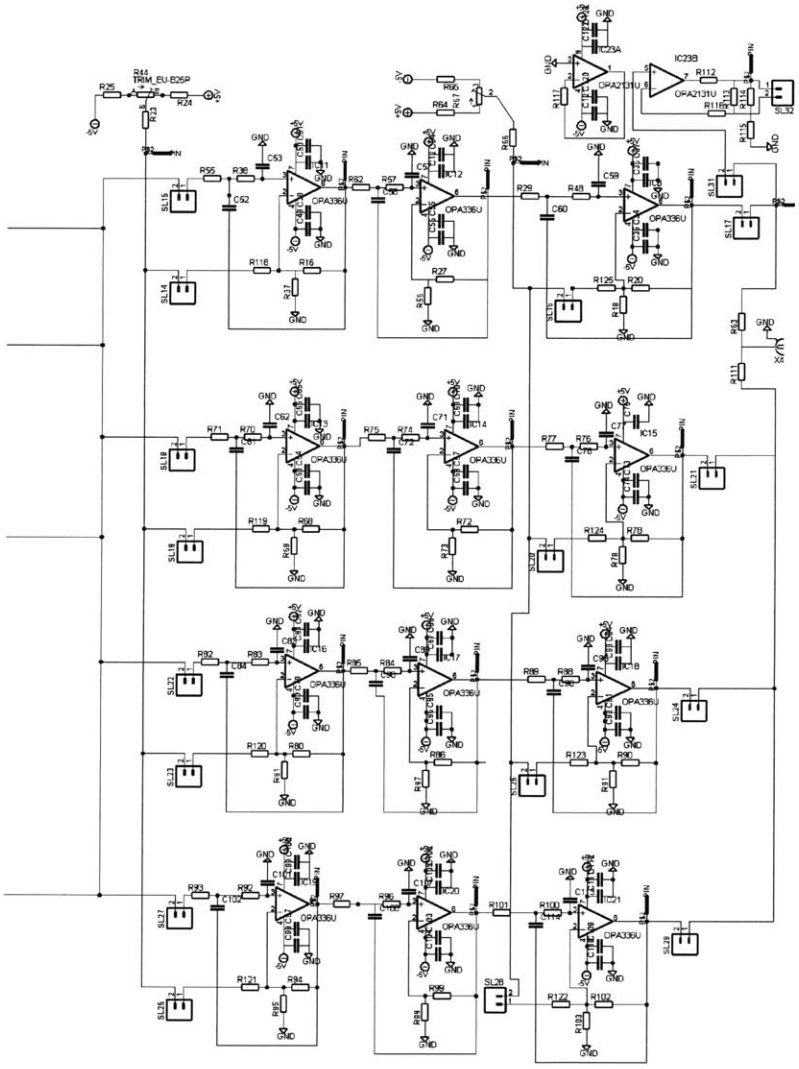

Figure A-8: Complete feedback control circuit: filter bank and DC-bias.

Bibliography

[1] F. X. Kaertner. Gigahertz high-resolution optical sampling technology (ghost). *Proposal to DARPA/ MTO*, 2004.

[2] Ioffe Physico-Technical Institute. Electronic archive new semiconductor materials. characteristics and properties, 2005.

[3] J.F. Philipps, T. Topfer, H. Ebendorff-Heidepriem, D. Ehrt, and R. Sauerbrey. Spectroscopic and lasing properties of er¡sup¿3+¡/sup¿:yb¡sup¿3+¡/sup¿-doped fluoride phosphate glasses. *Applied Physics B: Lasers and Optics*, 72(4):399–405, 2001.

[4] D. Payne. A new architecture for optical networking. In *CIPS annual meeting, May-19, 2005.*

[5] D. Welch. Design and implementation of lsi-pics. In *CIPS annual meeting, May-19, 2005.*

[6] A. Willner. Future highly efficient optical networks. In *CLEO 2005*, CTuX3.

[7] F. A. Kish and et. al. 100 gb/s (10 x 10 gb/s) dwdm photonic integrated circuit transmitters and receivers. In *CLEO 2005*, CMGG3.

[8] F. J. Leonberger. Trends in optical components and modules. In *APOC Executive Forum, 2002*, 2002.

[9] D.C. Kilper, R. Bach, D.J. Blumenthal, D. Einstein, T. Landolsi, L. Ostar, M. Preiss, and A.E. Willner. Optical performance monitoring. *Lightwave Technology, Journal of*, 22(1):294–304, 2004.

[10] A.E. Willner, S.M.R.M. Nezam, Zhongqi Pan, and Qian Yu. Performance degradations and monitoring in optical networks. *Proceedings of the SPIE - The International Society for Optical Engineering APOC 2003: Asia-Pacific Optical and Wireless Communications. Network Architectures, Management, and Applications, 4-6 Nov. 2003*, 5282:261–74, 2004.

[11] R.A. Soref. Silicon-based optoelectronics. *Proc. IEEE*, 81(12), 1993.

[12] A.V. Krishnamoorthy and D.A.B. Miller. Scaling optoelectronic-vlsi circuits into the 21st century: a technology roadmap. *IEEE J. of Selected Topics in Quantum Electronics*, 2:55–76, 1996.

[13] B. Jalali, S. Yegnanarayanan, T. Yoon, T. Yoshimoto, I. Rendina, and F. Coppinger. Advances in silicon-on-insulator optoelectronics. *IEEE J. of Selected Topics in Quantum Electronics*, 4(6):938–947, 1998.

[14] L.C. Kimerling. Silicon microphotonics. *Applied Surface Science*, 159-160:8–13, 2000.

[15] M. Salib, L. Liao, R. Jones, M. Morse, A. Liu, D. Samara-Rubio, D. Alduino, and M. Paniccia. Silicon photonics. *Intel Technology Journal*, (2), 2004.

[16] S. M. Sze. *Physics of Semiconductor Devices*. John Wiley and Sons, 1981.

[17] H.A. Lopez and P.M. Fauchet. Room-temperature electroluminescence from erbium-doped porous silicon. *Applied Physics Letters*, 75(25):3989–91, 1999.

[18] M. Lipson and L.C. Kimerling. Strong er/sup 3+/-photon interaction. *Optical Materials French-Israeli Workshop on Optical Properties of Inorganic Materials, 5-8 Dec. 1999*, 16(1-2):47–52, 2001.

[19] Ansheng Liu, Haisheng Rong, M. Paniccia, O. Cohen, and D. Hak. Net optical gain in a low loss silicon-on-insulator waveguide by stimulated raman scattering. *Optics Express*, 12(18), 2004.

[20] H. Rong, A. Liu, R. Jones, O. Cohen, D. Hak, R. Nicolaescu, A. Fang, and M. Paniccia. An all-silicon raman laser. *Nature*, 433(7023):292–4, 2004.

[21] Naisheng Rong, R. Jones, Ansheng Liu, O. Cohen, D. Hak, A. Fang, and M. Paniccia. A continuous-wave raman silicon laser. *Nature*, 433(7027):725–8, 2005.

[22] O. Boyraz and B. Jalali. Demonstration of directly modulated silicon raman laser. *Optics Express*, 13(3), 2005.

[23] E. A. De Souza, M.C. Nuss, W.H. Knox, and D.A.B. Miller. Wavelength-division multiplexing with femtosecond pulses. *Opt. Lett.*, 20(10):1166–1168, 1995.

[24] L. Boivin, M. Wegmuller, M.C. Nuss, W.H. Knox, Y. Sun, A.K. Srivastava, J.W. Sulhoff, and C. Wolf. Transmission over 360 km of 110 channels at 2.35 gb/s from a spectrum-sliced modelocked laser. In *Optical Fiber Communication Conference, 1999, and the International Conference on Integrated Optics and Optical Fiber Communication. OFC/IOOC '99. Technical Digest*, volume 3, pages 218–220 vol.3, 1999.

[25] J.S. Lee, Y.C. Chung, and D.J. DiGiovanni. Spectrum-sliced fiber amplifier light source for multichannel wdm applications. *Photonics Technology Letters, IEEE*, 5(12):1458–1461, 1993.

[26] O. Boyraz, J. Kim, M.N. Islam, E. Coppinger, and B. Jalali. 10 gb/s multiple wavelength, coherent short pulse source based on spectral carving of supercontinuum generated in fibers. *Lightwave Technology, Journal of*, 18(12):2167–2175, 2000.

[27] Y.J. Chai, C.G. Leburn, A.A. Lagatsky, C.T.A. Brown, R.V. Penty, I.H. White, and W. Sibbett. 1.36-tb/s spectral slicing source based on a cr/sup 4+/-yag femtosecond laser. *Lightwave Technology, Journal of*, 23(3):1319–1324, 2005.

[28] J.S. Lee, Y.C. Chung, T.H. Wood, J.P. Meester, C.H. Joyner, C.A. Burrus, J. Stone, H.M. Presby, and D.J. DiGiovanni. Spectrum-sliced fiber amplifier light source with a polarization-insensitive electroabsorption modulator. *Photonics Technology Letters, IEEE*, 6(8):1035–1038, 1994.

[29] J.J. Veselka and S.K. Korotky. A multiwavelength source having precise channel spacing for wdm systems. *Photonics Technology Letters, IEEE*, 10(7):958–960, 1998.

[30] K. Mori and K. Sato. Supercontinuum lightwave generation employing a mode-locked laser diode with injection locking for a highly coherent multicarrier source. *IEEE Photonics Technology Letters*, 17(2):480–482, 2005.

[31] L. Boivin, M.C. Nuss, W.H. Knox, and J.B. Stark. 206-channel chirped-pulse wavelength-division multiplexed transmitter. *Electronics Letters*, 33(10):827–829, 1997.

[32] J.B. Stark, M.C. Nuss, W.H. Knox, S.T. Cundiff, L. Boivin, and U. Koren. Chirped wavelength-division-multiplexed local access network using a shared source. In *Lasers and Electro-Optics, 1997. CLEO '97., Summaries of Papers Presented at the Conference on*, volume 11, pages 281–282, 1997.

[33] L. Boivin, M. Wegmueller, M.C. Nuss, and W.H. Knox. 110 channels times 2.35 gb/s from a single femtosecond laser. *Photonics Technology Letters, IEEE*, 11(4):466–468, 1999.

[34] B.C. Collings, M.L. Mitchell, L. Boivin, and W.H. Knox. A 1021 channel wdm system. *Photonics Technology Letters, IEEE*, 12(7):906–908, 2000.

[35] S.T. Cundiff, B.C. Collings, L. Boivin, M.C. Nuss, K. Bergman, W.H. Knox, and Jr. Evangelides, S.G. Propagation of highly chirped pulses in fiber-optic communications systems. *Lightwave Technology, Journal of*, 17(5):811–816, 1999.

[36] J. B. Schlager, B. E. Callicoatt, R. P. Mirin, N. A. Sanford, D. J. Jones, and J. Ye. Passively mode-locked glass waveguide laser with 14-fs timing jitter. *Optics Letters*, 28(23):2411–2413, 2003.

[37] A. Winter, F. O. Ilday, O. Muecke, R. Ell, H. Schlarb, P. Schmueser, and F. X. Kaertner. Towards high-performance optical master oscillators for energy recovery linacs. *submitted to Nuclear Instruments and Methods*, 2005.

[38] L. Krainer, R. Paschotta, S. Lecomte, M. Moser, K. J. Weingarten, and U. Keller. Compact nd:yvo4 lasers with pulse repetition rates up to 160 ghz. *IEEE J. of Quantum Electronics*, 38(10):1331–1338, 2002.

[39] L. Krainer, R. Paschotta, G. J. Spuehler, I. Klimov, K. J. Weingarten, and U. Keller. Tunable picosecond pulse-generating laser with repetition rate exceeding 10 ghz. *Electronics Letters*, 38:225–226, 2002.

[40] S. C. Zeller, F. Krausz, G.J. Spuehler, R. Paschotta, M. Golling, D. G. Ebling, K. J. Weingarten, and U. Keller. Passively modelocked 50 ghz er:yb:glass laser. *Electronics Letters*, 40(14):875–876, 2004.

[41] Ch. Erny, G.J. Spuhler, L. Krainer, R. Paschotta, K.J. Weingarten, and U. Keller. Simple repetition rate tunable picosecond pulse-generating 10 ghz laser. *Electronics Letters*, 40(14):877–8, 2004.

[42] Xun Li, Gui-Rong Zhou, Ning-Ning Feng, and Weiping Huang. A novel planar waveguide wavelength demultiplexer design for integrated optical triplexer transceiver. *IEEE Photonics Technology Letters*, 17(6):1214–16, 2005.

[43] Kemiao Jia, Wenhui Wang, Yanzhe Tang, Yirong Yang, Jianyi Yang, Xiaoqing Jiang, Yaming Wu, Minghua Wang, and Yuelin Wang. Silicon-on-insulator-based optical demultiplexer employing turning-mirror-integrated arrayed-waveguide grating. *IEEE Photonics Technology Letters*, 17(2):378–80, 2005.

[44] V. Van, B.E. Little, S.T. Chu, and J.V. Hryniewicz. Micro-ring resonator filters. In *2004 IEEE LEOS Annual Meeting Conference Proceedings, 7-11 Nov. 2004*, volume Vol.2 of *2004 IEEE LEOS Annual Meeting Conference Proceedings (IEEE Cat. No.04CH37581)*, pages 571–2, Rio Grande, Puerto Rico, 2004. IEEE.

[45] T. Barwicz, M.A. Popovic, P.T. Rakich, M.R. Watts, H.A. Haus, E.P. Ippen, and H.I. Smith. Microring-resonator-based add-drop filters in sin: fabrication and analysis. *Optics Express*, 12(7), 2004.

[46] Spectral grids for wdm application 1: Dwdm frequency grid. *ITU-T recommendation G.694.1*, May 2002.

[47] A. Liu, R. Jones, L. Liao, D. Samara-Rubio, D. Rubin, O. Cohen, R. Nocolaescu, and M. Paniccia. A high-speed silicon optical modulator based on a metal-oxide-semiconductor capacitor. *Nature*, 427:615–618, 2004.

[48] F. Gan and F. X. Kaertner. High-speed silicon electrooptic modulator design. *IEEE Photonics Technology Letters*, 17(5):1007–1009, 2005.

[49] V. R. Almeida, C. A. Barrios, R.R. Panepucci, and M. Lipson. All-optical control of light on a silicon chip. *Nature*, 431:1081–1084, 2004.

[50] J. Leibrich, C. Wree, and W. Rosenkranz. Cf-rz-dpsk for suppression of xpm on dispersion-managed long-haul optical wdm transmission on standard single-mode fiber. *Photonics Technology Letters, IEEE*, 14(2):155–157, 2002.

[51] M. Nakazawa, H. Kubota, K. Suzuki, E. Yamada, and A. Sahara. Ultrahigh-speed long-distance tdm and wdm soliton transmission technologies. *Selected Topics in Quantum Electronics, IEEE Journal of*, 6(2):363–396, 2000.

[52] F. J. Grawert, B. Kommandur, and S. Weinstein. Business plan for microlaser inc. *M.I.T. 50k business plan competition*, 2004.

[53] S.A. Hamilton, B.S. Robinson, T.E. Murphy, S.J. Savage, and E.P. Ippen. 100 gb/s optical time-division multiplexed networks. *Lightwave Technology, Journal of*, 20(12):2086–2100, 2002.

[54] M. Nakazawa, T. Yamamoto, and K.R. Tamura. 1.28 tbit/s-70 km otdm transmission using third- and fourth-order simultaneous dispersion compensation with a phase modulator. *Electronics Letters*, 36(24):2027–2029, 2000.

[55] M. Nakazawa. Tb/s otdm technology. In *Optical Communication, 2001. ECOC '01. 27th European Conference on*, volume 5, pages 184–187 vol.2, 2001.

[56] P.W. Juodawlkis, J.C. Twichell, G.E. Betts, J.J. Hargreaves, R.D. Younger, J.L. Wasserman, F.J. O'Donnell, K.G. Ray, and R.C. Williamson. Optically sampled analog-to-digital converters. *Microwave Theory and Techniques, IEEE Transactions on*, 49(10):1840–1853, 2001.

[57] M. Y. Frankel, J. U. Kang, and R. D. Esman. High-performance photonic analogue-to-digital converter. *Electronics Letters*, 33(25):2096–2097, 1997.

[58] A.S. Bhushan, F. Coppinger, S. Yegnanarayanan, and B. Jalali. Nondispersive wavelength-division sampling. *Opt. Lett.*, 24(11):738–740, 1999.

[59] F. Coppinger, A.S. Bhushan, and B. Jalali. Photonic time stretch and its application to analog-to-digital conversion. *Microwave Theory and Techniques, IEEE Transactions on*, 47(7):1309–1314, 1999.

[60] M.E. Grein, H.A. Haus, Y. Chen, and E.P. Ippen. Quantum-limited timing jitter in actively modelocked lasers. *IEEE Journal of Quantum Electronics*, 40(10):1458–70, 2004.

[61] A. Schlatter, B. Rudin, S.C. Zeller, R. Paschotta, G.J. Spuhler, L. Krainer, N. Haverkamp, H.R. Telle, and U. Keller. Nearly quantum-noise-limited timing jitter from miniature er:yb:glass lasers. *Optics Letters*, 30(12):1536–8, 2005.

[62] B. Resan, L. Archundia, and Jr. Delfyett, P.J. Frog measured high-power 185-fs pulses generated by down-chirping of the dispersion-managed breathing-mode semiconductor mode-locked laser. *IEEE Photonics Technology Letters*, 17(7):1384–6, 2005.

[63] M. Mielke, G.A. Alphonse, and P.J. Delfyett. 60 channel wdm transmitter using multiwavelength modelocked. *Electronics Letters*, 38(8):368–70, 2002.

[64] J. J. Zayhowski and A. Mooradian. Single-frequency microchip nd lasers. *Optics Letters*, 14:24–26, 1989.

[65] T. R. Schibli, U. Morgner, and F. X. Kaertner. Control of q-switched mode locking by active feedback. *Optics Letters*, 26:148 – 150, 2001.

[66] S. Tsuda, W. H. Knox, S. T. Cundiff, W. Y. Jan, and J. E. Cunningham. Mode-locking ultrafast solid-state lasers with saturable bragg reflectors. *IEEE J. sel. Topics in Quantum Electronics*, 2:454–464, 1996.

[67] G. Steinmeyer, D.H. Sutter, L. Gallman, N. Matuschek, and U. Keller. Frontiers in ultrashort pulse generation: Pushing the limits in linear and nonlinear optics. *Science*, 286:1507–1511, 1999.

[68] J. J. Zayhowski and P. L. Kelley. Optimization of q-switched lasers. *IEEE J. Quantum Electronics*, 27:2220–2225, 1991.

[69] J. J. Zayhowski. Q-switched operation of microchip laser. *Optics Letters*, 16:575–577, 1991.

[70] F. X. Kaertner, L. R. Brovelli, D. Kopf, M. Kamp, I. Calasso, and U. Keller. Control of solid-state laser dynamics by semiconductor devices. *Optical Engineering*, 34:2024–2036, 1995.

[71] T. R. Schibli, T. Kremp, U. Morgner, F. X. Krtner, R. Butendeich, J. Schwarz, H. Schweizer, and F. Scholz. Continuous-wave operation and q-switched mode locking of cr4+:yag-microchip lasers. *Optics Letters*, 26(12):148–150, 2001.

[72] E. R. Thoen, E. M. Koontz, D. J. Jones, D. Barbier, F. X. Krtner, E. P. Ippen, and L. A. KolodziejskiT. Erbium-ytterbium waveguide laser mode-locked with a semiconductor saturable absorber mirror. *Photonics Technology Lett.*, 12:149 – 151, 2000.

[73] F. J. Grawert, F. O. Ilday, D. Kielpinski, J. T. Gopinath, G. S. Petrich, L. A. Kolodiejski, E.P. Ippen, and F. X. Kaertner. Automatic feedback control of an er-doped fiber laser with an intracavity loss modulator. *Opt. Lett.*, 30(9):1066–68, 2005.

[74] H. A. Haus. Parameter ranges for cw passive modelocking. *IEEE J. Quantum Electronics*, QE-12:169–176, 1976.

[75] S. Namiki, E. P. Ippen, H. A. Haus, and C. X. Yu. Energy rate equations for mode-locked lasers. *J. Opt. Soc. Am. B*, 14(8):2099–2111, 1997.

[76] C. Hoenninger, R. Paschotta, F. Morier-Genoud, M. Moser, and U. Keller. Q-switching stability limits of continuous-wave passive mode locking. *J. of the Optical Society of America B*, 46(1):46 – 56, 1999.

[77] D. J. Harter, Y. B. Band, and E. P. Ippen. Theory of mode-locked lasers containing a reverse saturable absorber. *IEEE J. of Quantum Electronics*, 21(8):1219–1228, 1985.

[78] T. R. Schibli, E. R. Thoen, F. X. Kaertner, and E. P. Ippen. Suppression of modelocked q-switching and break-up into multiple pulses by inverse saturable absorption. *Applied Physics B*, 70:41 – 49, 2000.

[79] E. R. Thoen, E. M. Koontz, M. Joschko, P. Langlois, T. R. Schibli, F. X. Kaertner, E. P. Ippen, and L. A. Kolodziejski. Two-photon absorption in semiconductor saturable absorber mirrors. *Applied Physics Lett.*, 74:3927 – 3929, 1999.

[80] P. Langlois, M. Joschko, E. R. Thoen, E. M. Koontz, F. X. Krtner, E. P. Ippen, and L. A. Kolodziejski. High fluence ultrafast dynamics of semiconductor saturable absorber mirrros. *Applied Physics Letters*, 75:3841 – 3483, 1999.

[81] E. R. Thoen, M. E. Grein, E. M. Koontz, E. P. Ippen, H. A. Haus, and L. A. Kolodziejski. Stabilization of an active harmonically mode-locked fiber laser using two-photon absorption. *Optics Letters*, 25:948 – 951, 2000.

[82] P. Cerny, G. Valentine, D. Burns, and K. McEwan. Passive stabilization of a passively mode-locked laser by nonlinear absorption in indium phosphide. *Opt. Lett.*, 29(12):1387–9, 2004.

[83] R. Grange, M. Haiml, R. Paschotta, G. J. Spuehler, L. Krainer, M. Golling, O. Ostinelli, and U. Keller. New regime of inverse saturable absorption for self-stabilizing passively mode-locked lasers. *Appl. Phys. B*, 80(2):151–158, 2004.

[84] A. Agnesi, A. Guandalini, A. Tomaselli, E. Sani, A. Toncelli, and M. Tonelli. Diode-pumped passively mode-locked and passively stabilized nd/sup 3+/:bay/sub 2/f/sub 8/ laser. *Optics Letters*, 29(14):1638–40, 2004.

[85] N. Joly and S. Bielawski. Suppression of q-switch instabilities by feedback control in passively modelocked lasers. *Opt. Lett.*, 26(10):692–4, 2001.

[86] N. Joly and S. Bielawski. Self-starting of feedback control in lasers with a tendency to q-switch. *Optics Communications*, 220:171–177, 2003.

[87] S. Tsuda, W. H. Knox, E. A. de Souza, W. Y. Jan, and J. E. Cunningham. Low-loss intracavity alas/algaas saturable bragg reflector for femtosecond mode locking in solid-state lasers. *Optics Letters*, 20:1406–1408, 1995.

[88] D. Lorenser, H.J. Unold, D.J.H.C. Maas, A. Aschwanden, R. Grange, R. Paschotta, D. Ebling, E. Gini, and U. Keller. Towards wafer-scale integration of high repetition rate passively mode-locked surface-emitting semiconductor lasers. *Applied Physics B (Lasers and Optics)*, B79(8):927–32, 2004.

[89] A. Schlatter, S. C. Zeller, R. Grange, R. Paschotta, and U. Keller. Pulse-energy dynamics of passively mode-locked solid-state lasers above the q-switching threshold. *J. Opt. Soc. Am. B*, 21(8):1469–78, 2004.

[90] H. A. Haus. Theory of modelocking with a fast saturable absorber. *Journal of Applied Physics*, 46:3049–3058, 1975.

[91] H. A. Haus. Theory of mode locking with a slow saturable absorber. *IEEE Journ. of Quantum Electron.*, QE 11:736–46, 1975.

[92] D. E. Spence, P. N. Kean, and W. Sibbett. 60-fsec pulse generation from a self-mode-locked ti:sapphire laser. *Optics Lett.*, 16:42–44, 1991.

[93] M. Hofer, M.E. Fermann, F. Haberl, M.H. Ober, and A.J. Schmidt. Mode locking with cross-phase and self-phase modulation. *Optics Letters*, 16(7):502–4, 1991.

[94] J. T. Gopinath, E.R. Thoen, E. M. Koontz, M. E. Grein, L. A. Kolodiejski, E. P. Ippen, and J. P. Donnelly. Recovery dynamics in proton-bombarded semiconductor saturable absorber mirrors. *Appl. Phys. Lett.*, 78:3409–3411, 2001.

[95] S. Gupta, J. F. Whitaker, and G.A. Mourou. Ultrafast carrier dynamics in iii-v semiconductors grown by molecular-beam epitaxy at very low substrate temperatures. *IEEE J. of Quantum Electronics*, 28(10):2464–2472, 1992.

[96] E. L. Delpon, J. L. Oudar, N. Bouche, R. Raj, A. Shen, N. Stelmakh, and J. M. Lourtioz. Ultrafast excitonic saturable absorption in ion-implanted ingaas-inalas multiple quantum wells. *Appl. Phys. Lett.*, 72(7):759–761, 1998.

[97] Normal S. Nise. *Control Systems Engineering.* Addison-Wesley, 2nd edition, 1995.

[98] Otto Foellinger. *Regelungstechnik.* Huethig Verlag, Heidelberg, 8th edition, 1994.

[99] F. X. Kaertner, I. D. Jung, and U. Keller. Soliton mode-locking with saturable absorbers. *IEEE J. of Selected Topics in Quantum Electronics*, 2(3):540–556, 1996.

[100] F. X. Kaertner, J. Aus der Au, and U. Keller. Mode-locking with slow and fast saturable absorbers - what's the difference? *IEEE J. of Sel. Topics in Quantum Electronics*, 4(2):159, 1998.

[101] F.X. Kaertner and U. Keller. Stabilization of solitonlike pulses with a slow saturable absorber. *Optics Letters*, 20(1):16–18, 1995.

[102] L. R. Brovelli, I. D. Jung, D. Kopf, M. Kamp, M. Moser, F. X. Krtner, and U. Keller. Self-starting soliton modelocked ti:sapphire laser using a thin semiconductor saturable absorber. *Electronics Lett.*, 31:287–289, 1995.

[103] V. Liverini, S. Schon, R. Grange, M. Haiml, S.C. Zeller, and U. Keller. Gainnas sesams passively mode-locking 1.3- mu m solid-state lasers. *IEE Proceedings-Optoelectronics*, 151(5):437–41, 2004.

[104] M. Haiml, R. Grange, and U. Keller. Optical characterization of semiconductor saturable absorbers. *Applied Physics B (Lasers and Optics)*, B79(3):331–9, 2004.

[105] S. Taccheo, P. Laporto, O. Svelto, and G. De Geronimo. Intensity noise reduction in a single-frequency ytterbium-codoped erbium laser. *Optics Letters*, 21(21):1747–9, 1996.

[106] S. Taccheo, G. Sorbello, P. Laporta, and C. Svelto. Suppression of intensity noise in a diode-pumped tm-ho:yag laser. *Optics Letters*, 25(22):1642–4, 2000.

[107] S. Taccheo, P. Laporta, O. Svelto, and G. De Geronimo. Theoretical and experimental analysis of intensity noise in a codoped erbium-ytterbium glass laser. *Applied Physics B (Lasers and Optics)*, B66(1):19–26, 1998.

[108] C. Svelto, S. Taccheo, M. Marano, G. Sorbello, and P. Laporta. Optoelectronic feedback loop for relaxation oscillation intensity noise suppression in tm-ho:yag laser. *Electron. Lett.*, 36(19):1623–4, 2000.

[109] S. Longhi, M. Marano, P. Laporta, O. Svelto, R. Corsini, and F. Fontana. Amplitude noise suppression in high-repetition-rate pulse train generation from a frequency-modulated er-yb laser. *Applied Physics B (Lasers and Optics)*, B69(5-6):487–90, 1999.

[110] T. R. Schibli, K. E. Robinson, U. Morgner, F. X. Kaertner, S. Mohr, and D. Kopf . Control of q-switching instabilities in passively mode-locked lasers. In M. E. Fermann Marshall and L. R., editors, *Advanced Solid-State Lasers*, volume 68, pages 498–504, Quebec, Canada, 2002. Optical Society of America,.

[111] S. Bielawski, M. Bouazaoui, D. Derozier, and P. Glorieux. Stabilization and characterization of unstable steady states in a laser. *Phys. Rev. A*, 47(4):3276–3280, 1993.

[112] D. Barbier, M. Rattay, F. Saint Andre, G. Clauss, M. Trouillon, A. Kevorkian, J.-M. P. Delavaux, and E. Murphy. Amplifying four-wavelength combiner based on erbium/ytterbium-doped waveguide amplifiers and integrated splitters. *IEEE Photonics Tehnology Letters*, 9(3):315–7, 1997.

[113] J. T. Gopinath. *Studies of third-order nonlinearities in materials and devices for ultrafast lasers.* PhD thesis, Massachusetts Institute of Technology, 2005.

[114] N.H. Bonadeo, W.H. Knox, J.M. Roth, and K. Bergman. Passive harmonic mode-locked soliton fiber laser stabilized by an optically pumped saturable bragg reflector. *Optics Letters*, 25(19):1421–3, 2000.

[115] J.M. Roth, N.H. Bonadeo, K. Bergman, and W.H. Knox. Polarisation-maintaining, harmonically modelocked soliton fibre laser with repetition rate stabilisation using optical pumping of saturable bragg reflector. *Electronics Letters*, 38(1):16–17, 2002.

[116] M.D. Guina, A.-M. Vainionpaa, L. Orsila, A. Harkonen, J. Lyytikainen, L.A. Gomes, and O.G. Okhotnikov. Saturable absorber intensity modulator. *IEEE Journal of Quantum Electronics*, 39(9):1143–9, 2003.

[117] A.R. Chraplyvy. Limitations on lightwave communications imposed by optical-fiber nonlinearities. *Lightwave Technology, Journal of*, 8(10):1548–1557, 1990.

[118] B. E. Bouma and J. G. Fujimoto. Compact kerr-lens-mode-locked resonators. *Optics Lett.*, 21:Jan. 15, 1996.

[119] A. Penzkofer, M. Wittmann, E. Sigert, and S. MacNamara. Kerr lens effects in a folded-cavity four-mirror linear resonator. *Optical and Quantum Electronics*, 28:423–42, 1996.

[120] V. Magni, G. Cerullo, and S. DeSilvestri. Abcd matrix analysis of propagation of gaussian beams through kerr media. *Optics Communications*, 96:348–355, 1993.

[121] H. A. Haus. *Waves and Fields in Optoelectronics.* Prentice–Hall, Englewood Cliffs, New Jersey, 1984.

[122] H. Kogelnik and T. Li. Laser beams and resonators. *Applied Optics*, 5:1550–1567, 1966.

[123] O. D. Muecke, Ell R., A. Winter, Kim J., J. R. Birge, L. Matos, and F. X. Kaertner. Self-referenced 200 mhz octave-spanning ti:sapphire laser with 50 attosecond carrier-envelope phase jitter. *Optics Express*, 13(13):5163–5169, 2005.

[124] P. Kubina, P. Adel, F. Adler, G. Grosche, T.W. Hansch, R. Holzwarth, A. Leitenstorfer, B. Lipphardt, and H. Schnatz. Long term comparison of two fiber based frequency comb systems. *Optics Express*, 13(3), 2005.

[125] K. Tamura, E. P. Ippen, H. A. Haus, and L. E. Nelson. 77-fs pulse generation from a stretched-pulse modelocked all-fiber ring laser. *Optics Letters*, 18:1080–1082, 1993.

[126] F. O. Ilday, J. Chen, and F. X. Kaertner. Generation of sub-100-fs pulses at up to 200 mhz repetition rate from a passively mode-locked yb-doped fiber laser. *Optics Express*, 13(7):2716–2721, 2005.

[127] J. Bishop. Filterpro (tm) low-pass design tool. *Analog applications journal, Texas Instruments Inc.*, 2002.

[128] www.minicircuits.com. Datasheet of the plp low-pass filter series.

[129] K. Vahala. Optical microcavities. *Nature*, 424:839–846, 2003.

[130] E. M. Purcell. Spontaneous emission probabilities at radio frequencies. *Phys. Rev.*, 69:681, 1946.

[131] P. J. Reece, M. Gal, H. H. Tan, and C. Jagadish. Optical properties of erbium-implanted porous silicon microcavities. *Appl. Phys. Lett.*, 85(16):3363–5, 2004.

[132] A. Polman, B. Min, J. Kalkman, T. J. Kippenberg, and K. J. Vahala. Ultralow-threshold erbium-implanted toroidal microlaser on silicon. *Appl. Phys. Lett.*, 84(7):1037–9, 2004.

[133] M. K. Emsley, O. Dosunmu, and M. S. Unlu. High-speed resonant-cavity-enhanced silicon photodetectors on reflecting silicon-on-insulator substrates. *IEEE Photonics Technology Letters*, 14(4):519–521, 2002.

[134] O. I. Dosunmu, D. D. Cannon, M. K. Emsley, B. Ghyselen, J. Liu, L. C. Kimerling, and M. S. Unlu. Resonant cavity enhanced ge photodetectors for 1550 nm operation on reflecting si substrates. *IEEE J. of Selected Topics in Quantum Electronics*, 10(4):694–701, 2004.

[135] Y. Fink, J. N. Winn, S. Fan, C. Chen, J. Michel, J. D. Joannopoulos, and E. L. Thomas. A dieletric omnidirectional reflector. *Science*, 282:1679–1682, 1998.

[136] A. Bruyant, G. Lerondel, P. J. Reece, and M. Gal. All-silicon omnidirectional mirrors based on one-dimensional photonic crystals. *Appl. Phys. Lett.*, 82(19):3227–3229, 2003.

[137] S.N. Tandon, J.T. Gopinath, H.M. Shen, G.S. Petrich, L.A. Kolodziejski, F.X. Kartner, and E.P. Ippen. Large-area broadband saturable bragg reflectors by use of oxidized alas. *Optics Letters*, 29(21):2551–3, 2004.

[138] R. Fluck, I. D. Jung, G. Zhang, F. X. Krtner, and U. Keller. Broadband saturable absorber for 10 fs pulse generation. *Optics Lett.*, 21(10):743–745, 1996.

[139] Zhigang Zhang, K. Torizuka, T. Itatani, K. Kobayashi, T. Sugaya, T. Nakagawa, and H. Takahashi. Broadband semiconductor saturable-absorber mirror for a self-starting mode-locked cr:forsterite laser. *Optics Letters*, 23(18):1465–7, 1998.

[140] Zhigang Zhang, T. Nakagawa, K. Torizuka, T. Sugaya, and K. Kobayashi. Self-starting mode-locked cr/sup 4+/:yag laser with a low-loss broadband semiconductor saturable-absorber mirror. *Optics Letters*, 24(23):1768–70, 1999.

[141] Y. Ishikawa, N. Shibata, and S. Fukatsu. Epitaxy-ready si/sio2 bragg reflectors by multiple separation-by-implanted-oxygen. *Appl. Phys. Lett.*, 69(25):3881–3, 1996.

[142] M. Bruel. Silicon on insulator material technology. *Electron. Lett.*, 31(14):1201–2, 1995.

[143] K. Wada, T. Chen, J. Michel, L. C. Kimerling, H. Aga, K. Mitani, T. Abe, and M. Suezawa. Photonic bandgap formation by wafer bonding and delamination. *MRS proc. vol. 535, p. 121*, 1999.

[144] C. B. Li, H. X. Li, R. W. Mao, Y. H. Zuo, W. H. Shi, L. Zhao, L. P. Luo, B. W. Cheng, J. Z. Yu, and Q. M. Wang. Fabrication of low-cost and high-reflectivity bottom mirrors for si-based micro-cavity devices. *Electron. Lett.*, 40(17):1079–1080, 2004.

[145] D.I. Babic, J. Piprek, K. Streubel, R.P. Mirin, N.M. Margalit, D.E. Mars, J.E. Bowers, and E.L. Hu. Design and analysis of double-fused 1.55- mu m vertical-cavity lasers. *IEEE Journal of Quantum Electronics*, 33(8):1369–83, 1997.

[146] M. Ortsiefer, R. Shau, G. Bohm, F. Kohler, and M.-C. Amann. Room-temperature operation of index-guided 1.55 mu m inp-based vertical-cavity surface-emitting laser. *Electronics Letters*, 36(5):437–9, 2000.

[147] H.-W. Song, W.S. Han, J.-H. Kim, O.-K. Kwon, Y.-G. Ju, J.-H. Lee, S.-H. KoPark, and S.-G. Kang. 1.55 mu m bottom-emitting inalgaas vcsels with al/sub 2/o/sub 3//a-si thin-film pairs as top mirror. *Electronics Letters*, 40(14):868–9, 2004.

[148] S. Akiyama. *High index contrast platform for silicon photonics.* PhD thesis, Massachusetts Institute of Technology, 2004.

[149] Myung-Chul Jun, Yong-Sang Kim, Min-Koo Han, Jin-Won Kim, and Ki-Bum Kim. Polycrystalline silicon oxidation method improving surface roughness at the oxide/polycrystalline silicon interface. *Appl. Phys. Lett.*, 66(17):2206–8, 1995.

[150] C. Mazure, I. Cayrefourcq, B. Ghyselen, F. Letertre, and C. Maleville. Moving from today's soi to advanced substrate engineering. *Solid State Technology*, 46(7):111–115, 2003.

[151] F. J. Grawert, J. T. Gopinath, F. O. Ilday, H. Shen, E. P. Ippen, F. X. Kaertner, S. Akiyama, J. Liu, K. Wada, and L. C. Kimerling. 220 fs er-yb:glass laser mode-locked by a broadband low-loss si/ge saturable absorber. *Opt. Lett.*, 30(3):329–331, 2005.

[152] A. C. Adams. Dielectric and polysilicon film deposition. *in S. M. Sze, Ed., VLSI Technology, McGraw Hill, New York 1983*, 1983.

[153] H. A. Haus. Theory of mode locking with a fast saturable absorber. *Journ. of Appl. Phys.*, 64:3049–58, 1975.

[154] L. Matos, D. Kleppner, O. Kuzucu, T.R. Schibli, J. Kim, E.P. Ippen, and F.X. Kaertner. Direct frequency comb generation from an octave-spanning, prismless ti:sapphire laser. *Optics Letters*, 29(14):1683–5, 2004.

[155] T. R. Schibli, J. Kim, O. Kuzucu, J. T. Gopinath, S. N. Tandon, G. S. Petrich, L. A. Kolodziejski, J. G. Fujimoto, E. P. Ippen, and F. X. Kaertner. Attosecond active synchronization of passively mode-locked lasers using balanced cross-correlation. *Opt. Lett.*, 28:947–949, 2003.

[156] T. R. Schibli, O. Kuzucu, J.-W. Kim, E. P. Ippen, J. G. Fujimoto, F. X. Kaertner, V. Scheuer, and G. Angelow. Toward single-cycle laser systems. *IEEE J. of Selectred Topics in Quantum Electronics*, 9(4):990–1001, 2003.

[157] R. Szipoecs, K. Ferencz, Ch. Spielmann, and F. Krausz. Chirped multilayer coatings for broadband dispersion control in femtosecond lasers. *Optics Lett.*, 19:201–203, 1994.

[158] F. X. Kaertner, N. Matuschek, T. Schibli, U. Keller, H. A. Haus, C. Heine, R. Morf, V. Scheuer, M. Tilsch, and T. Tschudi. Design and fabrication of double-chirped mirrors. *Optics Lett.*, 22(13):831–833, 1997.

[159] N. Matuschek, F. X. Kaertner, and U. Keller. Analytic design of double-chirped mirrors with custom tailored dispersion characteristics. *IEEE J. of Quantum Electronics*, 5:129 – 137, 1999.

[160] Y. Ishikawa, K. Wada, D.D. Cannon, Jifeng Liu, Hsin-Chiao Luan, and L.C. Kimerling. Strain-induced band gap shrinkage in ge grown on si substrate. *Applied Physics Letters*, 82(13):2044–6, 2003.

[161] J. T. Gopinath. Ultrafst pump probe measurements on silicon-germanium saturable absorbers, personal communication, 2005.

[162] Jr. Boggess, T.F., K.M. Bohnert, K. Mansour, S.C. Moss, I.W. Boyd, and A.L. Smirl. Simultaneous measurement of the two-photon coefficient and free-carrier cross section above the bandgap of crystalline silicon. *IEEE Journal of Quantum Electronics*, QE-22(2):360–8, 1986.

[163] H.K. Tsang, C.S. Wong, T.K. Liang, I.E. Day, S.W. Roberts, A. Harpin, J. Drake, and M. Asghari. Optical dispersion, two-photon absorption and self-phase modulation in silicon waveguides at 1.5 mu m wavelength. *Applied Physics Letters*, 80(3):416–18, 2002.

[164] T.F. Boggess, A.L. Smirl, S.C. Moss, I.W.Boyd, and E.W. van Stryland. Optical limiting in gaas. *IEEE J. of Quantum Electronics*, QE-21(5):488–494, 1985.

[165] H.K. Tsang, R.V. Penty, I.H. White, R.S. Grant, W. Sibbett, J.B.D. Soole, H.P. LeBlanc, N.C. Andreadakis, R. Bhat, and M.A. Koza. Two-photon absorption and self-phase modulation in ingaasp/inp multi-quantum-well waveguides. *Journal of Applied Physics*, 70(7):3992–4, 1991.

[166] M. Ortsiefer, R. Shau, G. Bohm, F. Kohler, and M.-C. Amann. Low-threshold index-guided 1.5 mu m long-wavelength vertical-cavity surface-emitting laser with high efficiency. *Applied Physics Letters*, 76(16):2179–81, 2000.

[167] E. Desurvire. *Erbium-Doped Fiber Amplifiers.* John Wiley & Sons, New York, 1994.

[168] S. C. Zeller, L. Krainer, G. J. Spuehler, K. J. Weingarten, R. Paschotta, and U. Keller. Passively mode-locked 40-ghz er:yb:glass laser. *Appl. Phys. B*, 76:787–788, 2003.

[169] G. J. Spuehler, M. Dymott, I. Klimov, G. Luntz, L. Baraldi, I. Kilburn, P. Crosby, S. Thomas, O. Zehnder, C. Y. Teisset, M. Brownell, K. J. Weingarten, R. Dangel, B. J. Offrein, G. L. Bona, O. Buccafusca, Y. Kaneko, L. Krainer, R. Paschotta, and U. Keller. 40 ghz pulse generating source with less than 350 fs timing jitter. *Electronics Letters*, 38:1031–1032, 2002.

[170] E. Snitzer and R. Woodcock. Yb3+-er3+ glass laser. *Applied Physics Letters*, 6:45–46, 1965.

[171] P. Laporta, S. Taccheo, S. Longhi, O. Svelto, and G. Sacchi. Diode-pumped microchip er-yb:glass laser. *Optics Letters*, 18(15):1232–4, 1993.

[172] R. Fluck, R. Haring, R. Paschotta, E. Gini, H. Melchior, and U. Keller. Eyesafe pulsed microchip laser using semiconductor saturable absorber mirrors. *Applied Physics Letters*, 72(25):3273–5, 1998.

[173] P. Laporta, S. Longhi, S. Taccheo, and O. Svelto. Analysis and modelling of the erbium-ytterbium glass laser. *Optics Communications*, 100:311–321, 1993.

[174] G. Wasik, F.W. Helbing, F. Koenig, A. Sizmann, and G. Leuchs. Bulk er:yb:glass soliton femtosecond laser. In *CLEO proceedimgs, CMA4*, 2001.

[175] G.J. Spuehler, L. Gallman, R. Fluck, G. Zhang, L.R. Brovelli, C. Harder, P. Laporta, and U. Keller. Passively modelocked diode-pumped erbium-ytterbium glass laser using a semiconductor saturable absorber mirror. *Electronics Letters*, 35(7):567–569, 1999.

[176] B. Schmidt, N. Lichtenstein, B. Sverdlov, N. Matuschek, S. Mohrdiek, T. Pliska, J. Muller, S. Pawlik, S. Arlt, H.-U. Pfeiffer, A. Fily, and C. Harder. Further development of high power pump laser diodes. volume 5248 of *Proceedings of SPIE - The International Society for Optical Engineering*, pages 42–54, 2003.

[177] S. Taccheo, P. Laporta, and C. Svelto. Widely tunable single-frequency erbium-ytterbium phosphate glass laser. *Applied Physics Letters*, 68(19):2621–2623, 1996.

[178] H. Byun. Numerical modeling of the erbium-ytterbium glass micro-laser with repect to gain bandwidth and output power. *term paper*, 2005.

[179] J. W. Nicholson, J. Jasapara, and W. Rudolph. Full-field characterization of femtosecond pulses by spectrum and cross-correlation measurements. *Opt. Lett.*, 24(23):1774–1776, 1999.

[180] I. D. Jung, F. X. Kaertner, N. Matuschek, D. H. Sutter, F. Morier-Genoud, Z. Shi, V. Scheuer, M. Tilsch, T. Tschudi, and U. Keller. Semiconductor saturable absorber mirrors supporting sub-10 fs pulses. *Applied Physics B: Special Issue on Ultrashort Pulse Generation*, 65:137–150, 1997.

[181] P. Horowitz and W. Hill. *The art of electronics.* Cambridge University Press, 2nd edition, 1980.